Polarimetry on the Advanced Cold Molecule Electron Electric Dipole Moment Experiment

Master Thesis
by
Vitaly Andreev

December 2016

Technische Universität München
Department of Physics

This work was supported by the full year scholarship of the German Academic Exchange Service (DAAD) and was part of the Visiting Fellow Program during the year 2015-16 at the Graduate School of Arts and Sciences at Harvard University in the research group of Prof. G. Gabrielse as a member of the ACME Collaboration.

ACME

DAAD Deutscher Akademischer Austauschdienst
German Academic Exchange Service

Contents

List of Figures

List of Tables

Acknowledgements

First of all, I would like to express my deep gratitude to Prof. Jerry Gabrielse for inviting me to join his group and for giving me the opportunity to work on the fascinating ACME experiment with an interesting and motivating project. I am very thankful for all the fruitful discussions, helpful comments, lots of advice and his thoughtful edits on the manuscript about the polarimeter. I learned a lot from Jerry and his great intuition for physics. I am also very grateful to the whole Gabrielse Research group for the very supportive and kind working climate, especially to Cris, Daniel, Elise, Mason, Geev, Melissa, Tharon, Cole and Ron.

I am very grateful to Prof. Peter Fierlinger for initially waking my interest in precision experiments during my Bachelor studies when I worked on the neutron EDM experiment, and for refereeing this thesis as part of the fulfillment of the Master's Degree at the Technical University of Munich. I thank the German Academic Exchange Service (DAAD) for providing me the scholarship for the Visiting Fellow program at Harvard and thereby giving me the opportunity to come to the U.S. Furthermore, I thank the German Academic Scholarship Foundation (Studienstiftung) for supporting my physics studies.

I would like to express my deep gratitude to the whole ACME Collaboration. I thank the Professors Jerry Gabrielse, John Doyle and Dave DeMille who lead the collaboration for stimulating and helpful discussions during the collaboration meetings. I thank John very much for inviting me to various social events and making me feel welcome in his group. I am very grateful to Dave for giving me an exciting tour of his labs when I visited Yale University, and always answering my questions with care and astonishingly clear explanations. I thank all of the ACME members, especially those who I worked most closely with – Adam, Brendon, Cris, Daniel, Elizabeth, Nick and Zack, for many stimulating and helpful discussions, for being open to questions at anytime and a delightful working environment. This thesis would also not have been possible without the first-generation ACME team who worked on understanding the thermally-induced birefringence and the design of the improved field plates, especially Nick, Paul, Ben and Brendon. I thank Elizabeth for helping me with the fiber laser which I used for first polarimetry tests and for giving me the opportunity to learn about the fascinating molecule source. I thank Adam, Ben, Brendon, Cris, Elizabeth, Paul and Zack for useful comments on the manuscript about the polarimeter. To sum up, it was a pleasure to work in such a great collaboration!

I would especially like to express my gratitude to Cris, who was my great 'lab brother'

during the whole period of my time on ACME. He was always ready to teach me about the ACME experiment and help me in case I had a question about my project. I am very grateful for his outstanding support, remarks, lots of advice and careful discussions about the polarimetry.

Furthermore, I am very thankful to Daniel who was also my 'lab brother', for always creating such a pleasant and joyful atmosphere, many discussions about and beyond physics, for always being so kind and open, and for the wonderful time of making music together.

I am also very grateful to all my other friends for the great hours together, inside or outside the university. I especially thank the Harvard Catholic Club and other St. Paul parish members, the Christian community of graduate students at Harvard, my friends from the Christian journal at MIT, and the Harvard Ballroom Dancing team. I thank the Harvard Memorial Church for the beautiful morning prayers providing me a great start of the day. I am very grateful to Fr. George, Fr. Mark, Fr. Kelly, and the whole St. Paul parish community who illuminated my time in the U.S. with deep joy and spiritual meaning. I am also very grateful to Elizabeth for the wonderful Easter celebration.

I am deeply grateful to Barbara, for her love and support which always accompanied and motivated me during my time in the U.S., even being most of the time on different continents with her. I am very indebted to my mother whose permanent support made my physics studies possible and who encouraged me throughout my entire life.

In my opinion, our thanksgivings, with or without recognizing it consciously, are always rooted in God, for He is the Love which dwells in us. At the same time being personally and subjective, in my view, God is the objective Logos. As I have come to think[1], science provides us with a taste of this Logos who is the fundamental reason of everything and the source of the beauty of nature and our understanding of the visible universe. I am deeply grateful to God for giving me the talents to participate in the joy and the adventure of physics.

'The diversity of the phenomena of nature is so great, and the treasures hidden in the heavens so rich, precisely in order that the human mind shall never be lacking in fresh nourishment.' [2]
JOHANNES KEPLER

'Both religion and science require a belief in God. For believers, God is in the beginning, and for physicists He is at the end of all considerations. To the former He is the foundation, to the latter, the crown of the edifice of every generalized world view.' [3]
MAX PLANCK

---

[1] MIT et Spiritus, `http://mitetspiritus.org`, Issue 1, Spring 2016, 'The Trinity of Physics, Christianity, and Life'. I am glad to learn from comments and criticism, and to discuss about these topics.

[2] J. Kepler, *Mysterium Cosmographicum*, Tübingen, 1596 (publisher: M. Caspar, Filser Augsburg, 1923)

[3] M. Planck, *Scientific Autobiography and Other Papers*, New York Philosophical Library, 1968

1 Introduction

Imagine holding an apple in your hands – this is how small our visible universe was around 13.8 billion years ago. This tiny piece of today's space-time contained an enormous amount of energy. The progress of our fundamental understanding of nature is rooted in investigating these early moments in the evolution of our universe. One approach is to reproduce this high temperature state in collider experiments, where high energy particles are directly produced. The current energy limit[1] of around 14 TeV is set by the Large Hadron Collider. High precision experiments provide us with insights into the fundamentals of nature on similar or even higher energy scales where virtual particles give rise to contributions of precisely measured quantities.

Understanding nature over many orders of magnitude, physicists can explore the first moments of the temporal evolution of our universe and predict to an astonishing precision the outcomes of experiments with the smallest units of matter [35]. We have a thorough understanding of the early phases of the universe, but there are still many unknowns and puzzles, for example dark matter, the cosmological constant, or the origin of matter in our universe. Most theories which could resolve some of these questions predict permanent electric dipole moments (EDMs) of particles. A precision-measurement of the electron EDM is particularly important to exclude or constrain various supersymmetry models. Furthermore, a non-zero value of an electron EDM violates the time reversal symmetry and could give us hints to explain the matter-antimatter asymmetry of our universe.

The current limit for the existence of the electron EDM was set by the Advanced Cold Molecule Electron EDM (ACME) Collaboration in 2013, performing a spin-precession measurement in thorium-232 monoxide (ThO) molecules. The value of the electron EDM is measured to be smaller than $9.3 \cdot 10^{-29}\,e\,\mathrm{cm}$ (90% confidence level) [8], thereby constraining various prominent particle physics theories [72]. The second-generation ACME experiment aims for even higher precision. The leading systematic uncertainties in the first-generation electron EDM measurement were due to imperfect polarizations of the laser beams needed to prepare and readout the EDM-sensitive state of the molecules. This thesis presents an improved polarimeter allowing for precise characterization of polarization imperfections. Furthermore, various polarimetry measurements on ACME are performed. In particular, a detailed investigation of thermally-induced birefringence in the

---

[1] In particle physics and cosmology, the Boltzmann constant is usually set to one, so that energy and temperature units are equivalent. An energy of $1\,\mathrm{eV}$ corresponds to a temperature of around 10^4 K.

indium-tin-oxide coated glass field plates is reported. These field plates, used to produce a static electric field in the ACME experiment and therefore being crucial for the whole measurement scheme, are dominantly responsible for the systematic error mechanism in the ACME's first generation. Polarimetry results shown in this thesis demonstrate that the newly designed second-generation field plates greatly suppress this effect.

The structure of this thesis is as follows: An overview of the ACME experiment in Chapter 2 summarizes the motivation for the search of an electron EDM, the measurement principle and the experimental setup, and gives an illustration of how imperfect polarization leads to systematic errors. The following Chapter 3 reports in detail on the self-calibrating polarimeter designed for ACME. This includes a brief review of the Stokes parameters needed to describe the polarization of light, the basics of a rotating waveplate polarimeter, its laboratory realization together with the intensity normalization scheme, the novel calibration technique, and an analysis of uncertainties. The polarimetry measurements on ACME are presented in Chapter 4. A particular focus is the thermally-induced birefringence in the electric field plates. Furthermore, mechanical stress-induced birefringence is investigated and tests of various optical elements are shown. Finally, a brief conclusion found in Chapter 5 sums up the content of this thesis.

2 The Advanced Cold Molecule Electron EDM (ACME) Experiment

This chapter briefly describes the Advanced Cold Molecule Electron Electric Dipole Moment (ACME) Experiment. More details can be found in theses by ACME graduates ([88, 43, 48, 40, 94]) and publications by the ACME collaboration (e.g. [9, 66, 8]). Since this thesis focuses on polarimetry, only a compact overview is given here. The first section summarizes the motivation for the search of an electron EDM and its link to the progress of fundamental physics. After introducing the measurement principle and the advantages of using ThO for an electron EDM experiment in Sec. 2.2, the ACME setup is presented in Sec. 2.3. The last Sec. 2.4 indicates how imperfect polarizations of laser beams affect the electron EDM measurement.

2.1 Motivation for the Search of an Electron EDM

Let us first illustrate how the electron EDM is related to the discrete symmetries. In the classical picture, an electric dipole moment $\vec{d}_{\mathrm{cl}}$ characterizes the spatial asymmetry in the charge distribution:

$$\vec{d}_{\mathrm{cl}} = \int \rho(\vec{r}) \cdot \vec{r}\ \mathrm{d}^3\vec{r}, \tag{2.1}$$

where $\rho(\vec{r})$ is the spatially dependent electric charge density. In molecular physics the unit Debye is often used to quantify its magnitude: $1\,\mathrm{D} \simeq 3.3 \cdot 10^{-30}\,\mathrm{C} \cdot \mathrm{m} \simeq 0.4\,e\,a_0$, where a_0 is the Bohr radius and e the electron charge. In particle physics, units of $e \cdot \mathrm{cm}$ are common instead. To compare this unit to atomic scales, consider the water molecule which has an electric dipole moment of around $3\,\mathrm{D} \simeq 1.6 \cdot 10^{-9}\,e \cdot \mathrm{cm}$ [39].

What distinguishes the electron EDM from the classical EDM is that it has to be either aligned or anti-aligned with the spin [73]. If this would not be the case, another quantum number could be added to describe the electron. Then, due to the Pauli principle, twice as many electrons could occupy the orbitals – the atomic spectra and chemical laws would be completely different. Since we know that our set of quantum numbers for the electron is sufficient to describe the atomic shell structure, we conclude that there cannot be any other quantum number which is not a combination of the known ones. The Wigner-Eckhard theorem [78] states that in this case the combined vector, in our case the electric dipole moment, must be proportional to the known vector quantity, in our case the spin.

The electron EDM is fundamentally different from the classical EDM which becomes clear if we consider the discrete symmetries of time reversal (described by the time-reversal operator $\hat{T}$) and parity inversion (described by the operator $\hat{P}$ which reverses the space coordinates). For a classical EDM, the space inversion operator $\hat{P}$ changes the sign of the EDM since it is proportional to $\vec{r}$:

$$\vec{d}_{\mathrm{cl}} \propto \vec{r} \quad \rightarrow \quad \hat{P}\vec{d}_{\mathrm{cl}} = -\vec{d}_{\mathrm{cl}}, \qquad \hat{T}\vec{d}_{\mathrm{cl}} = \vec{d}_{\mathrm{cl}}. \tag{2.2}$$

As discussed in the previous paragraph, the electron EDM is proportional to its spin and hence behaves oppositely under P- and T-transformations:

$$\vec{d}_{\mathrm{e}} \propto \vec{S} \quad \rightarrow \quad \hat{P}\vec{d}_{\mathrm{e}} = \vec{d}_{\mathrm{e}}, \qquad \hat{T}\vec{d}_{\mathrm{e}} = -\vec{d}_{\mathrm{e}}. \tag{2.3}$$

Since the electric field $\vec{\mathcal{E}}$ breaks the parity-reversal symmetry, $\hat{P}\vec{\mathcal{E}} = -\vec{\mathcal{E}}$, and is invariant in time, $\hat{T}\vec{\mathcal{E}} = \vec{\mathcal{E}}$, the corresponding electron EDM interaction term in the Hamiltonian,

$$\hat{H}_{\mathrm{eEDM}} = \vec{d}_{\mathrm{e}} \cdot \vec{\mathcal{E}}, \tag{2.4}$$

is odd under the P-symmetry and the T-symmetry:

$$\hat{P}(\hat{H}_{\mathrm{eEDM}}) = -\vec{d}_{\mathrm{e}} \cdot \vec{\mathcal{E}}, \qquad \hat{T}(\hat{H}_{\mathrm{eEDM}}) = -\vec{d}_{\mathrm{e}} \cdot \vec{\mathcal{E}}. \tag{2.5}$$

This demonstrates that the electron EDM breaks the time reversal and parity symmetries. For local quantum field theories, which are a successful framework for the Standard Model of particle physics and most of its extensions, the combined CPT symmetry, where C stands for the charge conjugation operator, is conserved [60].[1] Assuming the CPT-theorem, the electron EDM also violates the combined CP symmetry.

Symmetries have always been important in understanding the fundamentals of nature. Until the 1950s, a common paradigm in physics was that ‘nature is perfect’ such that the C-, P-, and T-symmetries are separately conserved. This is a natural assumption based on all the ‘perfect’ conservation laws we find in classical physics. We would never think that Newton’s law should be slightly different if we reverse the space. If we move to the left, $\vec{F} = m\,\vec{a}$ is true exactly the same way compared to if we move to the right. A breakthrough for fundamental physics happened in 1956 when Lee and Yang proposed to test the P symmetry [58]. In the same year, the astonishing experiment by Wu saw the violation of this fundamental symmetry in the weak interaction [99]. In 1964, Cronin and Fitch reported the violation of the combined CP-symmetry [18].

---

[1] There are theories which propose a violation of the CPT-symmetry [22]. Therefore, it is important to perform experimental CPT-tests, for example with antimatter experiments such as [27]. We remark that there is a controversy on whether CPT implies Lorentz invariance and vice versa [38, 16].

Today, CP-violation is well established in theory but still insufficient to explain one of the greatest puzzles of contemporary physics – the matter-antimatter asymmetry of the universe. Our universe arose from a hot dense state where matter and antimatter[2] are believed to be in equilibrium. Particles and antiparticles are created and annihilated as long as the temperature of the universe is sufficiently high to exceed the rest energy of the particle. As the universe expands, it cools down and the interactions fall out of equilibrium. This so-called 'freeze-out' of particles occurs when the expansion rate H is approximately equal to the rate of particle interactions Γ [62].

The question of how much matter survives the early phases of the universe is quantified by the baryon-to-photon density ratio n_b/n_γ. A simple estimate based on the standard cosmological model yields, see App. A.1:

$$n_b/n_\gamma \sim 10^{-18}. \tag{2.6}$$

However, the observational value is far off the prediction [67]:

$$n_b/n_\gamma = (6.09 \pm 0.06) \cdot 10^{-10}. \tag{2.7}$$

This value can be obtained from several independent observations which are all remarkably consistent with each other [67, 62]. The striking discrepancy between Eqs. 2.6 and 2.7 of around nine orders of magnitude points to the lack of understanding of the origin of baryons, even without mentioning the apparent absence of anti-baryons [23].

In addition to the above discrepancy, we find almost no anti-baryons in our universe which is referred to as the matter-antimatter asymmetry. According to Sakharov [77], three conditions are necessary to produce an excess of matter over antimatter: violation of baryon number, violation of C- *and* CP-symmetries, and a thermal non-equilibrium. Interestingly, all Sakharov conditions are satisfied in the Standard Model. First, though not directly observed yet, the baryon number is broken via anomalies present in quantum field theories[3] [70]. Second, as discussed above, the C- and CP-symmetries are found to be violated and a corresponding mechanism is implemented in the Standard Model. Third, the thermal non-equilibrium is a known phenomenon in the development of our universe [62]. Though a slight asymmetry between baryons and anti-baryons can be produced within the Standard Model, a detailed quantitative analysis shows that the specific value disagrees with the observed baryon-to-photon ratio by many orders of magnitude [15]. Therefore, undiscovered sources of Sakharov conditions must exist, which can only be explained by physics beyond the Standard Model.

---

[2] What is antimatter? The charge-conjugation operator $\hat{C}$ converts a particle state $|\Psi\rangle$ into antiparticle state $|\overline{\Psi}\rangle$. The operator $\hat{C}$ changes sign of all additive quantum numbers (e.g. electric charge, baryon number) but leaves the space-time related properties unchanged (e.g. mass, energy, momentum, spin).

[3] The triangle anomaly leads to the sphaleron process which violates the baryon number. This non-perturbative effect was first realized by 't Hooft in 1976 [91].

CP-violations beyond the Standard Model can manifest in permanent EDMs [72]. Since the electron EDM violates the C-, T- and CP-symmetries (assuming CPT-theorem), it is a prominent candidate for new sources for the fulfillment of the Sakharov conditions. Also other permanent EDMs, for instance of the neutron or the proton, are important for the research on this topic. Whereas the neutron and proton EDMs also probe the strong interaction, the electron EDM provides an outstanding probe of CP-violation in leptons.

In addition to the matter-antimatter puzzle of the universe, many other hints point to physics beyond the Standard Model. For example, gravity is not consistently included into current quantum field theories, we do not know what dark matter is, we do not understand the source of the cosmological constant, and the Standard Model of particle physics suffers from the so-called hierarchy problem [67]. Extensions to the Standard Model provide possible solutions to some of these problems. Most of the prominent models, like various modifications of Supersymmetry, predict a value for the electron EDM. The origin of the electron EDM can be interpreted as the asymmetrical charge distribution in the cloud of virtual particles surrounding the electron. In the n-loop process, Ramsey et al. showed that the electron EDM would be related to the mass scale m_x of the new particle as [30]:

$$|d_e| \simeq \frac{\hbar e}{c}\frac{m_e}{m_\mathrm{x}^2}\left(\frac{\alpha}{4\pi}\right)^n \sin\phi_{CP}, \tag{2.8}$$

where e is the electron charge and α the coupling strength between the electron with mass m_e and the new particle. The phase ϕ_{CP} is naturally expected to be maximally CP-violating [72]. For $n = 1$ and $\sin\phi_{CP} \simeq 1$, we obtain a value of:

$$|d_e| \simeq 10^{-27}\, e\cdot\mathrm{cm}\quad \left(\frac{10\ \mathrm{TeV}}{m_\mathrm{x}c^2}\right)^2 \tag{2.9}$$

Therefore, the electron EDM measurement is a very strong probe of new physics. The electron acts as an ‘antenna’ for virtual massive particles arising in CP-violating interactions. The current electron EDM limit is set by the first-generation ACME measurement:

$$|d_e| < 9.3\cdot 10^{-29}\, e\cdot\mathrm{cm}\quad (90\%\ \text{confidence level})\ [8]. \tag{2.10}$$

Most simple supersymmetric models predict an electron EDM of $d_e \sim 10^{-26}\, e\cdot\mathrm{cm}$. Therefore, the result of Eq. 2.10 constrains the parameter space of various modifications of supersymmetry, pushing them to the unnatural fine tuning. Note that the Standard Model also predicts a non-zero value for the electron EDM, $d_e \lesssim 10^{-38}\, e\cdot\mathrm{cm}$, which is unrealistic to verify by the experiment, though. This is due to the fact that the CP-violation in the Standard Model is manifested in the quark sector and contributes to the leptonic electron EDM only on the fourth loop order.

2.2 Measurement Principle and Advantages of Thorium Monoxide

When measuring the electron EDM, we wish to determine an interaction whose energy contribution is:

$$\hat{H}_{\mathrm{eEDM}} = \vec{d}_{\mathrm{e}} \cdot \vec{\mathcal{E}} = |\vec{d}_{\mathrm{e}}|\, \hat{\sigma} \cdot \vec{\mathcal{E}}, \tag{2.11}$$

where $\hat{\sigma}$ is the Pauli matrix corresponding to the direction of the spin, $\vec{\mathcal{E}}$ the electric field, and $\vec{d_e}$ the electron electric dipole moment. In order to measure this Hamiltonian term, we need a system where electrons have a known spin state which can be addressed and manipulated, and where electrons are subject to an electric field. As we shall see, we can find such a system in an atom or a molecule. For now, let us assume that the electron state can be controlled and we perform a spin precession measurement.

When the electron is placed in an electric and magnetic field, the Hamiltonian reads:

$$\hat{H} = \vec{\mu} \cdot \vec{B} + \vec{d_e} \cdot \vec{\mathcal{E}} = m\,(\,\mu B \pm d_e \mathcal{E}_{\mathrm{eff}}\,)\,, \tag{2.12}$$

where we assume that the magnetic and electric fields are aligned with a particular spin orientation $m = \pm 1$. The electron is subject to the effective electric field $\mathcal{E}_{\mathrm{eff}}$ (the term 'effective' is justified later). Furthermore, we allow for a reversal of the electric field. First, we prepare a superposition of spin states so that the initial state reads:

$$|\psi(0)\rangle = \frac{1}{\sqrt{2}}(|\uparrow\rangle + |\downarrow\rangle). \tag{2.13}$$

Then we let the electron interact with the electric and magnetic fields. According to the Schrödinger picture, during a time t the state accumulates a phase:

$$|\psi(t)\rangle = \exp(-\mathrm{i}\hat{H}t/\hbar)\,|\psi(0)\rangle. \tag{2.14}$$

After a precession time $t = \tau$, the state is given by:

$$|\psi(\tau)\rangle = \frac{1}{\sqrt{2}}(\mathrm{e}^{-\mathrm{i}\phi}|\uparrow\rangle + \mathrm{e}^{\mathrm{i}\phi}|\downarrow\rangle), \tag{2.15}$$

with the corresponding phase

$$\phi = \frac{\tau}{\hbar}(\mu B \pm d_e \mathcal{E}_{\mathrm{eff}}). \tag{2.16}$$

If we determine the phases $\phi_\pm$ with the opposite directions of the electric field, the value for the electron EDM can be extracted as:

$$d_e = \frac{\hbar(\phi_+ - \phi_-)}{2\,\tau\,\mathcal{E}_{\mathrm{eff}}}. \tag{2.17}$$

The phase ϕ can be measured by a projection onto a pair of orthogonal analyzer states $|\psi_{A,X}\rangle$ and $|\psi_{A,Y}\rangle$ given by:

$$|\psi_{A,X}\rangle = \frac{1}{\sqrt{2}}(|\downarrow\rangle - |\uparrow\rangle), \qquad |\psi_{A,Y}\rangle = \frac{1}{\sqrt{2}}(|\downarrow\rangle + |\uparrow\rangle)\,. \tag{2.18}$$

The projection from N prepared electrons leads to the signals S_X and S_Y :

$$S_X = N|\langle\psi_{A,X}|\psi(\tau)\rangle|^2 = N\cos^2(\phi), \qquad S_Y = N|\langle\psi_{A,Y}|\psi(\tau)\rangle|^2 = N\sin^2(\phi). \tag{2.19}$$

Determining the asymmetry $\mathcal{A}$ between these signals has the great advantage of being immune to possible fluctuations in the number of analyzed electrons in the system (in the ACME experiment N fluctuates by around 20%):

$$\mathcal{A} = \frac{S_X - S_Y}{S_X + S_Y} = \cos(2\phi). \tag{2.20}$$

If the orthogonal states $|\psi_{A,X}\rangle$ and $|\psi_{A,Y}\rangle$ are rotated by a degree ψ with respect to x in the xy-plane, the upper equation is modified by $\phi \to \phi - \psi$. A variety of imperfections (e.g imperfections in the state preparation or readout, decay back to the prepared state, velocity dispersion), introduce a reduced contrast $\mathcal{C} < 1$ in the asymmetry measurement:

$$\mathcal{A} = \frac{S_X - S_Y}{S_X + S_Y} = \mathcal{C}\cos[2(\phi - \psi)]. \tag{2.21}$$

On ACME the contrast value is typically $\mathcal{C} \simeq 0.94$. The contrast can be measured by dithering the small angle ψ when $\phi \approx (2n+1)\pi/4$ for integer n (condition for largest sensitivity on measuring small changes of ϕ):

$$\mathcal{C} = -\frac{1}{2}\frac{\partial\mathcal{A}}{\partial\psi}. \tag{2.22}$$

For a shot-noise limited measurement, the uncertainty in the phase measurement scales as $1/\sqrt{N}$ (see [94] for a detailed discussion). Comparing with Eq. 2.17, the sensitivity for the electron EDM is approximately given by

$$\delta d_e \simeq \frac{\hbar}{2\,\mathcal{C}\,\tau\,\mathcal{E}_{\text{eff}}\sqrt{\dot{N}T}}, \tag{2.23}$$

where we introduced the flux $\dot{N}$ and the total measurement time T.

As obvious from Eq. 2.23, it is important to maximize the effective electric field $\mathcal{E}_{\text{eff}}$. It turns out that the strongest electric fields an electron can experience are found in a molecule. Naively, one would expect that due to the Schiff's theorem [81] the net electric field on the electron bound in a neutral system vanishes. Indeed, if Eq. 2.11 was exactly true, the electron would not experience any electric field at all. However, Eq. 2.11 is only a non-relativistic approximation and the proper relativistic Hamiltonian reads:

$$\hat{H}_{\text{eEDM, rel.}} = \vec{d}_{\text{e}} \cdot \vec{\mathcal{E}} + \frac{\gamma}{1+\gamma} \vec{\beta} \cdot \vec{d}_e \, \vec{\beta} \cdot \vec{\mathcal{E}}, \tag{2.24}$$

where γ is the Lorentz factor and $\vec{\beta} = \vec{v}/c$ the dimensionless electron velocity. One can write the average value for this Hamiltonian in the familiar non-relativistic form of Eq. 2.11:

$$\langle \hat{H}_{\text{eEDM, rel.}} \rangle = m \, \langle |\vec{d}_{\text{e}}| \rangle \, \mathcal{E}_{\text{eff}}, \tag{2.25}$$

with $\mathcal{E}_{\text{eff}}$ being the effective electric field on the electron with spin alignment $m = \pm 1$. The fact that $\mathcal{E}_{\text{eff}}$ does not vanish was first realized by Sandars in 1965 [79]. The second term in Eq. 2.24 gives rise to the Lorentz contraction which makes Schiff's theorem invalid. In an atom or a molecule $\mathcal{E}_{\text{eff}}$ scales as:

$$\mathcal{E}_{\text{eff}} \propto \begin{cases} PZ^3\alpha^2 & \text{for} \quad Z \ll 140, \\ PZ^4\alpha^2 & \text{for} \quad Z \lesssim 140, \end{cases} \tag{2.26}$$

where Z is the atomic number, α the fine structure constant, and P the degree of polarization. The fact that $\mathcal{E}_{\text{eff}} \propto \alpha^2$ indicates that to a first-order Schiff's theorem is true, whereas a non-zero $\mathcal{E}_{\text{eff}}$ is a second-order effect. However, because of the Z dependence the effective electric field can easily become substantial for nuclei with large atomic numbers.

For atoms, only a small polarization fraction P can be achieved. Even to achieve $P \sim 10^{-3}$, very high applied electric fields on the order of $\mathcal{E}_{\text{app}} \sim 10^5$ kV/cm are required. On the contrary, molecules can be nearly fully polarized, $P \sim 1$, with modest electric fields of $\mathcal{E}_{\text{app}} < 10^2$ V/cm. Therefore, molecules provide a larger effective electric field with much smaller applied electric field. A larger $\mathcal{E}_{\text{eff}}$ value results in a higher electron EDM sensitivity whereas a smaller $\mathcal{E}_{\text{app}}$ reduces the sources of systematic errors. The limiting systematic errors in atomic EDM measurements, like the tellurium (Tl) experiment [75], are typically caused by large applied electric fields leading to geometric phases, motional magnetic fields and leakage currents.

An overview of the three most recent electron EDM experiments is given in Table 2.1. For a long time, from 1990 to 2011, the most precise limit on the electron EDM was achieved by the Tl experiment. Experiments with atoms have the advantage of a high flux $\dot{N}$. The flux attained with molecular beam sources is typically several orders of magnitude lower. However, EDM experiments with molecules are competitive to those with atoms because of the larger $\mathcal{E}_{\text{eff}}$ and a smaller $\mathcal{E}_{\text{app}}$ which suppresses several systematic errors. This was first demonstrated by the ytterbium fluoride (YbF) experiment in 2011. In the ACME experiment, the applied electric fields are even smaller and the effective electric field is more than five times larger than in YbF [33, 84]. Furthermore, the sophisticated cryogenic buffer gas beam source allows for a higher molecule flux [49].

System Group Year [ref]	$\mathcal{E}_{\mathrm{app}}$ [kV/cm]	P	$\mathcal{E}_{\mathrm{eff}}$ [GV/cm]	$\dot{N}$ [s^{-1}]	τ [ms]	T [h]	Result [$10^{-28}\,e\,\mathrm{cm}$]		
							$\boldsymbol{\lvert d_e \rvert}$	$\delta d_e^{\mathrm{stat}}$	$\delta d_e^{\mathrm{sys}}$
Tl Berkley 2002 [75]	123	10^{-3}	0.07	$8.5 \cdot 10^{8}$	2.4	60	$<$ **16**	5.5	5
YbF Imperial 2011 [46]	10	0.75	14.5	$1.2 \cdot 10^{4}$	0.65	280	$<$ **10.5**	5.7	1.5
ThO ACME 2013 [8]	0.03	1.00	78	$5 \cdot 10^{5}$	1.1	200	$<$ **0.93**	0.41	0.27

Table 2.1: Overview of the three most recent leading electron EDM experiments. The table shows the parameters relevant for the measurement sensitivity according to Eq. 2.23, as well as the final results of the experiments ($|d_e|$ at 90% confidence level, the statistical uncertainty $\delta d_e^{\mathrm{stat}}$ and the systematic uncertainty $\delta d_e^{\mathrm{sys}}$).

For all three listed experiments, the precession time τ is on the order of a millisecond. Typically, the precession time is limited by the lifetime of the used state. For the ACME experiment, the lifetime of the EDM-sensitive H-state in ThO is 1.8 ms [95]. Even if the states lived much longer, a larger precession time could cause possible systematic effects, for instance due to the velocity dispersion leading to different interaction times. Because of the residual magnetic field the variation in the interaction time results in a broader phase distribution. Therefore, a much larger precession time is not necessarily a better choice.

A further requirement for an electron EDM measurement is a suitable electronic state. For ThO, the $H\,{}^3\Delta_1$ state of rotational level $J = 1$ turns out to be a perfect candidate. In this state, the two valence electrons are in the σ and δ orbitals. The σ electron is closer to the nucleus and is therefore responsible for the high effective electric field. The presence of the δ electron results in a small magnetic moment of $\mu_1 = g_1 \mu_B$, where μ_B is the Bohr magneton and $g_1 = 0.00440(5)$ the small g-factor [71, 96]. This makes the EDM measurement largely immune to magnetic field noise.

Another important property of the $H\,{}^3\Delta_1$ state is the Ω-doublet structure which is illustrated in Fig. 2.1. Without the applied electric field, the molecules are in one of the defined parity states $|\pm\rangle$. This configuration is symmetric or antisymmetric under $\hat{P}$-transformation, $\hat{P}|\pm\rangle = \pm|\pm\rangle$:

$$|\pm\rangle = \frac{1}{\sqrt{2}}\left(\left|\begin{smallmatrix}\mathrm{O}\\ \uparrow\\ \mathrm{Th}\end{smallmatrix}\right\rangle \pm \left|\begin{smallmatrix}\mathrm{Th}\\ \downarrow\\ \mathrm{O}\end{smallmatrix}\right\rangle\right) \equiv \frac{1}{\sqrt{2}}\Big(|\tilde{\mathcal{N}} = -1\rangle \pm |\tilde{\mathcal{N}} = +1\rangle\Big)\,, \tag{2.27}$$

where $\tilde{\mathcal{N}}$ denotes the direction of the internuclear axis. The opposite parity states are

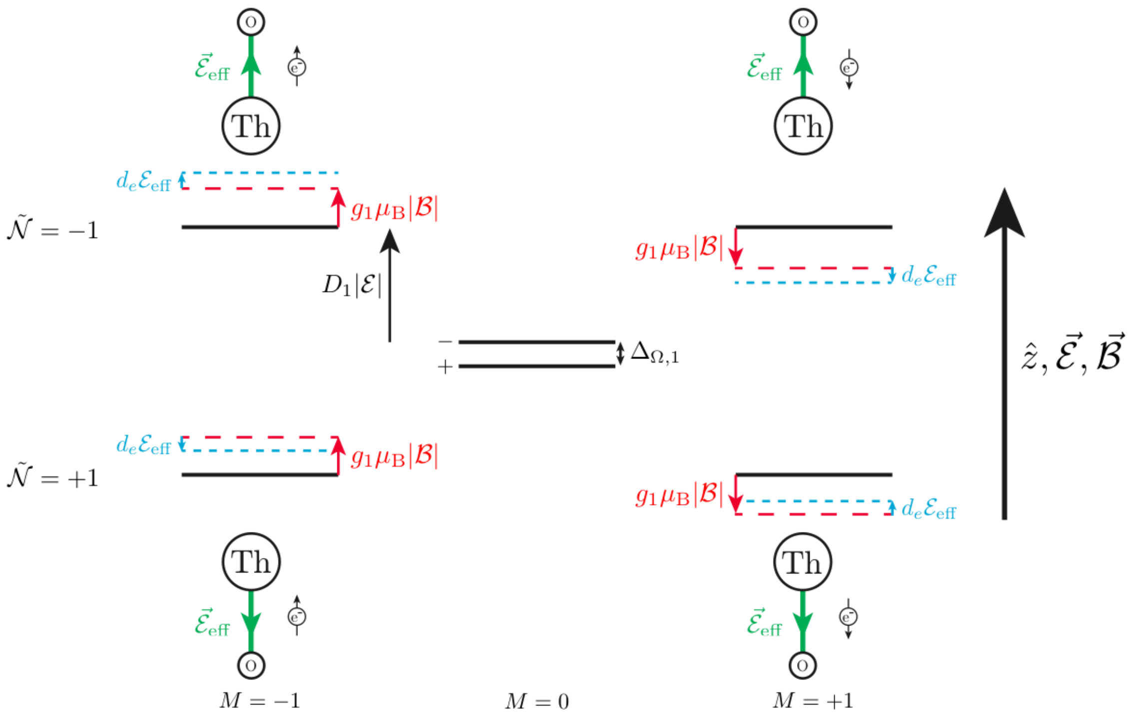

FIGURE 2.1: The energy level structure of the $H\,^3\Delta_1$ state in ThO illustrating the advantages for the electron EDM measurement, figure from [9]. The $|M = \pm 1\rangle$ states are subject to the linear Stark shift proportional to $D_1|\mathcal{E}|$ where $D_1 \simeq 2\pi \times 1\,\mathrm{MHz/(V/cm)}$ is the molecular electric dipole moment and $\mathcal{E}$ the applied electric field. The contribution of the Zeeman shift $g_1\mu_B|B|$ is shown in red. A non-zero electron EDM results in a shift proportional to $d_e\mathcal{E}_{\mathrm{eff}}$ depicted in blue. The electric and magnetic fields are aligned with the laboratory $\hat{z}$ axis which determines the orientation of the effective electric field $\vec{\mathcal{E}}_{\mathrm{eff}}$ as well as the orientation of the spin of the σ electron.

separated by $\Delta_{\Omega,1} \simeq 2\pi \times 360\,\mathrm{kHz}$ due to the Coriolis force [14].[4] An applied electric field polarizes the molecules and thus breaks the space-reversal symmetry. The molecules are now in the $|\tilde{\mathcal{N}} = \pm 1\rangle$ states of mixed parity:

$|\tilde{\mathcal{N}} = -1\rangle \equiv |$ 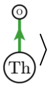 $\rangle = \frac{1}{\sqrt{2}}\left(|+\rangle + |-\rangle\right)\,, \qquad |\tilde{\mathcal{N}} = +1\rangle \equiv |$ 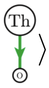 $\rangle = \frac{1}{\sqrt{2}}\left(|+\rangle - |-\rangle\right)\,.$ (2.28)

Note that for $M = 0$ the linear Stark shift does not occur and the molecules still are in the opposite parity states $|\pm\rangle$ from the case of zero applied electric field. The electric dipole moment of the H state is $D_1 \simeq 2\pi \times 1\,\mathrm{MHz/(V/cm)}$. Therefore, the condition for a nearly perfect polarization, $D_1|\mathcal{E}| \gg \Delta_{\Omega,1}$, can be achieved with applied electric fields on the order of $\sim 10\,\mathrm{V/cm}$. Another advantage of the Ω-doublet is the possibility of reversing the effective electric field without altering the laboratory electric field by addressing different $\mathcal{N}$ states. This is of great importance for studying various systematic errors.

---

[4] The Ω-doublet splitting of the C state in ThO is much larger, $\Delta_{\Omega,C,1} \sim 50\,\mathrm{MHz}$, and can easily be spectroscopically resolved. Optical pumping of the $H \to C$ transition thus allows to switch the parity of the prepared H state.

2.3 The ACME Experimental Setup

The basic ACME setup is shown in Fig. 2.2. For the sake of simplicity, the molecular beam source is not shown. This sophisticated hydrodynamically enhanced cryogenic buffer gas beam source is crucial for the ACME experiment [49]. Here we just quote the result: fifty times per second a 2 ms long pulse of ThO molecules with a velocity of $\sim 200\,\mathrm{m/s}$ and a rotational temperature of $\sim 4\,\mathrm{K}$ enters the interaction region. Thereafter, the molecules are polarized by the transparent glass electric field plates coated with a conductive layer of indium-tin-oxide (ITO). Then the desired molecule state is prepared, see Sec. 2.3.1. After the spins precess for ~ 1 ms in parallel electric and magnetic fields, the accumulated phase is measured by the readout laser beam. The molecules are pumped into a higher excited state (C state in the first generation and I state in the second) and the photons from the spontaneous decay are detected by photomultiplier tubes (PMTs).

In addition to what is depicted in Fig. 2.2, the ACME apparatus has magnetic field coils and five layers of magnetic shielding. Several coils wrapped around the vacuum chamber provide a constant magnetic field $\mathcal{B}_z$ parallel to the electric field, as well as constant

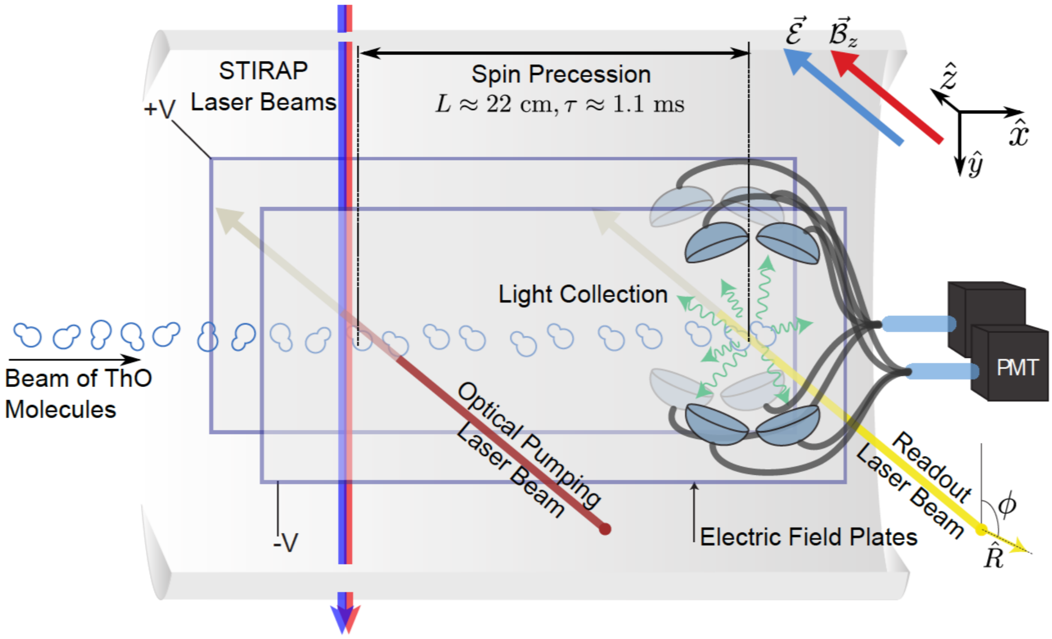

FIGURE 2.2: The basic ACME experimental setup, figure from [66] by C. Panda. The molecular beam source (not shown for the sake of simplicity) provides a beam of ThO molecules which are polarized with electric field plates as soon as they enter the interaction region. The desired EDM-sensitive state is prepared via the second-generation Stimulated Raman Adiabatic Passage (STIRAP) technique or via optical pumping (first-generation technique), see Sec. 2.3.1. Afterwards, the state precesses for ~ 1 ms in parallel electric and magnetic fields. The accumulated phase is measured by pumping into a higher excited state with the readout laser beam (which switches between orthogonal linear polarizations) and detecting the fluorescence photons with photomultiplier tubes (PMTs). Note that magnetic coils and shields are not shown in this figure.

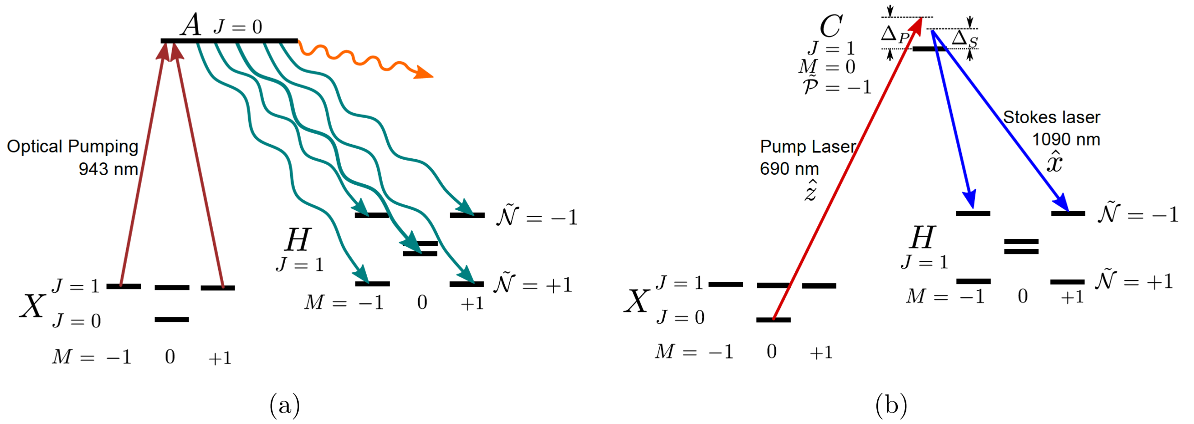

(a) (b)

FIGURE 2.3: Comparison of state preparation schemes for the first and second generations of the ACME experiment, figure from [66] by C. Panda. (a) In the first generation the molecules are pumped into the A state. The spontaneous decay to the H state results in an incoherent superposition of the H state sub-levels. A coherent superposition needs to be prepared by additional pumping to the C state (not shown here). (b) In the second generation, two laser beams are applied simultaneously. Carefully chosen parameters of these pump and the Stokes lasers allow for a Stimulated Raman Adiabatic Passage (STIRAP) from the lowest rotational X state level to a coherent superposition of the H state sub-levels.

magnetic fields in the other two directions and all five linearly independent first-order magnetic field gradients. The latter are used to study or exclude systematic errors. The magnetic field is permanently monitored by a set of four magnetometers[5]. As mentioned previously, the used H state of ThO has the great advantage of a small magnetic moment allowing to be largely insensitive to magnetic field imperfections.

2.3.1 First- and Second-generation State Preparation

The state preparation schemes differ for the first and second generations of the experiment and are compared in Fig. 2.3. In the first generation method, the molecules are optically pumped from the ground X state to the A state. This results in a spontaneous decay to the desired H state manifold. However, the superposition of H sub-levels is incoherent and therefore useless for the spin precession measurement until a coherent superposition of opposite spin states according to Eq. 2.13 is prepared. An additional state preparation laser (not shown in the figure) is responsible for optical pumping into the C state, thereby leaving the 'dark' coherent superposition of $M = \pm 1$ sub-levels of the H state. The first generation scheme is subject to many state losses. Only around 6% of molecules can finally be used for the EDM measurement.

The technique for the second generation demonstrates a transfer of $(75 \pm 5)\%$ of initial molecules into the desired state, a factor of 12 ± 1 increase in the usable number of molecules compared to the first generation [66]. In this so-called Stimulated Raman Adi-

---

[5] Bartington Instruments, Mag-03 Three-Axis Fluxgate Magnetometers

abatic Passage (STIRAP) two laser beams are applied simultaneously. Rotational cooling (also present in the first generation) is achieved by several lasers before the molecules enter the interaction region and enhances the population in the lowest rotational level of the X state. From this state the population is coherently transferred into a superposition of opposite spin states in the H state manifold. The prepared state is purified with an additional refinement laser beam (not shown in the figure), similar to the optical pumping in the first generation.

2.3.2 Phase Measurement and Switches

The interaction Hamiltonian responsible for a phase accumulation during the spin precession reads similar to Eq. 2.12:

$$\hat{H}(M, \tilde{\mathcal{N}}, \tilde{\mathcal{E}}, \tilde{\mathcal{B}}) = M(\tilde{\mathcal{B}} g_1 \mu_B \mathcal{B}_z + \tilde{\mathcal{B}}\tilde{\mathcal{N}} \eta \mu_B \mathcal{E} \mathcal{B}_z + \tilde{\mathcal{N}}\tilde{\mathcal{E}} d_e \mathcal{E}_{\mathrm{eff}}). \tag{2.29}$$

$M = \pm 1$ denotes the spin state of the electrons. $\tilde{\mathcal{N}} = \pm 1$ is the internuclear axis orientation corresponding to the upper or lower H state manifold in Fig. 2.1. $\tilde{\mathcal{B}} = \pm 1$ denotes the direction of the magnetic field in the z-direction with a magnitude $\mathcal{B}_z$. $\tilde{\mathcal{E}} = \pm 1$ is the direction of the electric field in the z-direction set by the voltage on the field plates. The first term in Eq. 2.29 accounts for the Zeeman shift with the small magnetic moment mentioned in the previous section. The second term is related to the electric field dependent magnetic moment difference between the upper ($\tilde{\mathcal{N}} = -1$) and lower ($\tilde{\mathcal{N}} = +1$) sub-levels of the H state, caused by Stark mixing with other ThO states. The parameter η is measured to be $\eta = 0.79(1)\,\mathrm{nm/V}$ [71]. The last term in Eq. 2.29 corresponds to a shift caused by the electron EDM we wish to determine.

For a precession time τ, the accumulated phase reads analogously to Eq. 2.16:

$$\phi = \frac{\tau}{\hbar}(\tilde{\mathcal{B}} g_1 \mu_B \mathcal{B}_z + \tilde{\mathcal{B}}\tilde{\mathcal{N}} \eta \mu_B \mathcal{E} \mathcal{B}_z + \tilde{\mathcal{N}}\tilde{\mathcal{E}} d_e \mathcal{E}_{\mathrm{eff}}). \tag{2.30}$$

As can be seen from Eq. 2.21, for a most sensitive measurement the accumulated phase ϕ needs to be $\phi \approx (2n+1)\pi/4 + \psi$ for integer n, where ψ is determined by the rotation of the two orthogonal linear polarizations of the readout laser[6]. This condition can be fulfilled by setting a corresponding magnetic field amplitude $\mathcal{B}_z$ as well as the polarization rotation angle ψ.

The accumulated phase is measured by the asymmetry between orthogonal state projections as described in the previous section. On ACME, this is realized with orthogonal linear polarization switching of the readout laser beam. To be as insensitive as possible to molecule number fluctuations, the polarization switching needs to be fast. However, the

---

[6] Note that in other theses or publications by ACME the linear rotation angle is typically called θ rather than ψ. In this thesis we choose ψ to be consistent with the definition of a linear rotation angle in Chapter 3, see Eq. 3.9 and Fig. 3.1.

upper limit is determined by the fluorescence state lifetime of around $0.5\,\mu$s because the spontaneous decay needs to be detectable. Ideally, one wants to measure the line shape of the emitted photon numbers. In the first generation the polarization was alternated every $5\,\mu$s, for the second generation the rate is doubled.

The polarization switching frequency constrains the horizontal width of the laser beam. The molecules need to experience both polarizations as they propagate through the laser light. With a switching frequency of 100-200 kHz and a velocity of 200 m/s we obtain a horizontal beam width on the order of $w_x \sim 1 - 2$ mm. The vertical width w_y needs to be much larger because of the angular spread of the molecular beam, $w_y \sim 30$ mm.

From Eq. 2.30 it becomes obvious that in order to measure the contribution of the electron EDM, we need to isolate the $\tilde{\mathcal{N}}\tilde{\mathcal{E}}$ correlated phase. Not only for this purpose, but also to study various systematic errors, several 'switches' are used in the ACME experiment. Aside from the polarization switching, the fastest switch is between the two configurations of the H state, $\tilde{\mathcal{N}} = \pm 1$. With an acousto-optic modulator (AOM), the laser frequency is alternated twice per second to address these different sub-levels of the H state manifold. The direction of the applied electric field $\tilde{\mathcal{E}} = \pm 1$ is switched every two seconds. The linear polarization rotation angle of the readout laser beam is dithered every 10 s by $\Delta\psi = 0.05$ rad to measure the contrast $\mathcal{C}$ from Eq. 2.21. The precession time τ is determined by varying the direction of the magnetic field $\tilde{\mathcal{B}} = \pm 1$ every 20 s. Those four switches, $\tilde{\mathcal{N}}$, $\tilde{\mathcal{E}}$, $\tilde{\psi}$, and $\tilde{\mathcal{B}}$, form a 'block' of data of all $2^4 = 16$ configurations of these experimental parameters which takes in total around 40 seconds [8].

On longer times scales, the following parameters are varied to study or to exclude systematic errors: the parity of the excited state $\mathcal{P}_{\text{read}}$, the simultaneous change of the power supply polarity and interchange of leads connecting the electric field plates to their voltage supply, a rotation of the state readout orthogonal polarizations by $\psi \to \psi + \pi/2$, the global polarization rotation of both state preparation and readout lasers by 90°, the magnitude of the magnetic field $\mathcal{B}_z$ (1, 19, or 38 mG) and the magnitude of the applied electric field $\mathcal{E}$ needed to polarize the molecules (varied between 36 and 141 V/cm) [8].

2.3.3 Second-generation Upgrades

In addition to the STIRAP state preparation scheme which results in a 12 times higher signal gain, the second generation of the ACME experiment features the following upgrades: optimized beamline geometry ($\sim 8\times$ gain), improved fluorescence collection ($\sim 2.5\times$ gain) and an increased efficiency of photomultiplier tubes due to a different detection wavelength ($\sim 2.5\times$ gain). From these improvements, an overall signal gain factor of $300 - 600$ in the spin precession measurement is anticipated [3]. Furthermore, a novel thermochemical molecular beam source which allows to produce an around ten times higher molecule flux is currently under development [3].

Regarding systematic error handling, the second generation ACME setup mainly has the following novel features: the refinement beam which aims to suppress STIRAP polarization fluctuations, the careful control of beam pointing, the modified apparatus for magnetometry, the monitoring and feed back system of laser light polarization, and the improved electric field plates [3]. This thesis presents a contribution to the latter two points. The polarimeter described in Chapter 3 allows to precisely measure the laser light polarization. In Chapter 4 various polarimetry measurements are discussed. A particular focus is the investigation of thermally-induced birefringence (Sec. 4.2). Anticipated improvements of optical and thermal properties of the new field plates are characterized by measurements of thermally-induced polarization changes. The proposed ellipticity feed back mechanism [65] accounts for waveplate imperfections which need to be investigated as demonstrated in Sec. 4.3.1. Furthermore, the knowledge of the absolute light polarization which reaches the molecules and may be affected by mechanical stress-induced birefringence, see Sec. 4.1, can be valuable. In addition, the polarization purity in the sideport of the Glan-Laser polarizer is tested in Sec. 4.3.4 which is important for the polarization switching scheme.

2.4 Systematic Errors due to Imperfect Polarizations

The dominant systematic errors in the first generation ACME setup are due to imperfect polarizations of the laser beams preparing and reading out the state of the ThO molecules. The mechanisms by which polarization imperfections produce an EDM-like phase are one of the most intricated ones. This thesis focuses on the characterization of polarization imperfections rather than the mechanism by which these imperfections cause a systematic effect. Therefore, it is only briefly mentioned how imperfect laser polarizations may contribute to spurious phases in the EDM measurement. We refer to [9] for more details.

Consider first an idealized measurement scheme with constant polarization offsets only, a small linear polarization rotation by $\psi_i \to \psi_i + \lambda d\psi_i$ and a small ellipticity change by $\chi_i \to \chi_i + \lambda d\chi_i$, where λ quantifies the small polarization imperfections. Note how a linear rotation angle ψ and an ellipticity angle χ are related to the relative Stokes parameters in the next chapter, see Eq. 3.9 and Fig. 3.1. Taking these offsets into account, the phase ϕ from Eq. 2.30 differs from the measured phase Φ as following [9]:

$$\Phi = \phi + \lambda(d\psi_{\mathrm{prep}} - \frac{1}{2}(d\psi_X + d\psi_Y)) - \lambda^2 \tilde{\mathcal{P}}_{\mathrm{prep}} \tilde{\mathcal{P}}_{\mathrm{read}} d\chi_{\mathrm{prep}}(d\chi_X - d\chi_Y) + \mathcal{O}(\lambda^3). \quad (2.31)$$

Note that a rotation of all polarization angles by the same amount leaves the measured phase unchanged, as should be true from symmetry arguments. A deviation in the relative linear polarization angle between the state preparation and readout beams adds an offset to the measured phase. However, if uncorrelated with other parameters or switches, this

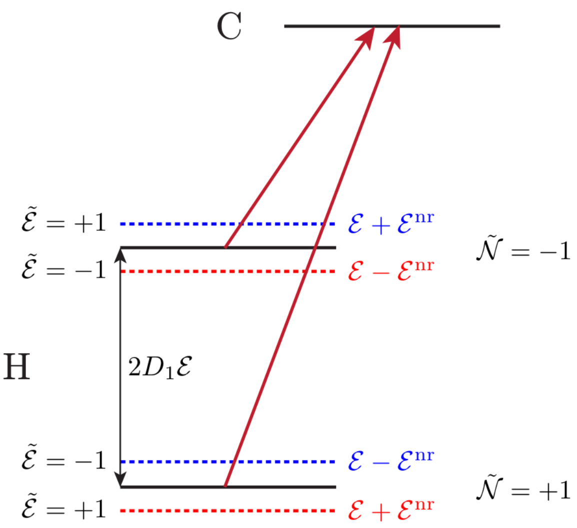

FIGURE 2.4: Illustration of how a non-reversing electric field $\mathcal{E}^{\mathrm{nr}}$ leads to a correlated laser frequency detuning $\Delta^{\mathcal{N}\mathcal{E}}$, figure from [9]. The energy levels $\tilde{\mathcal{N}} = \pm 1$ are shifted oppositely with a non-reversing electric field component $\mathcal{E}^{\mathrm{nr}}$ when switching the direction of the electric field $\tilde{\mathcal{E}} = \pm 1$.

offset is eliminated through measuring the $\tilde{\mathcal{N}}\tilde{\mathcal{E}}$ correlated phase. The contribution of an imperfect ellipticity enters the phase measurement only if it is different in the orthogonal readout laser beams. Furthermore, it can be distinguished from other contributions through the parity of the excited state for read out, $\tilde{\mathcal{P}}_{\mathrm{read}}$. To sum up, the terms in Eq. 2.31 are uncorrelated with the $\tilde{\mathcal{N}}\tilde{\mathcal{E}}$ switch used to extract the EDM phase. However, Eq. 2.31 provides a useful framework to analyze other polarization imperfections [9].

Polarization imperfections can contribute to a false EDM measurement through Stark interference between the electric dipole (E1) and magnetic dipole (M1) transition amplitudes. The analysis of this mechanism follows a calculation which is found in [9]. It is estimated, that in the first generation with an ellipticity corresponding to the relative Stokes parameter $S/I \sim 5\%$, this mechanism contributes to a systematic error on the order of $\omega^{\mathcal{N}\mathcal{E}} = \phi/\tau \sim 0.1$ mrad/s which corresponds to a false EDM on a scale of $10^{-30} - 10^{-31}\, e \cdot \mathrm{cm}$. With the demonstrated ellipticity imperfection of one to two orders of magnitude lower than in the first generation (see Fig. 4.10), this effect should be even smaller and can be neglected. However, it is important to confirm this conclusion through the polarization switches of the global polarization rotation and the rotation of the readout laser beam. These switches can be used to suppress the systematic error due to Stark interference between E1 and M1 transition amplitudes.

The leading systematic error in ACME's first generation was due to the mechanism of AC Stark shift phases. As above we refer to [9] for a detailed calculation and discussion. On ACME, the AC Stark shift phases produce an EDM-like phase by coupling to the correlated laser detuning $\Delta^{\mathcal{N}\mathcal{E}}$, combined with circular polarization gradients due to thermally-induced birefringence in the electric field plates. As illustrated in Fig. 2.4, the

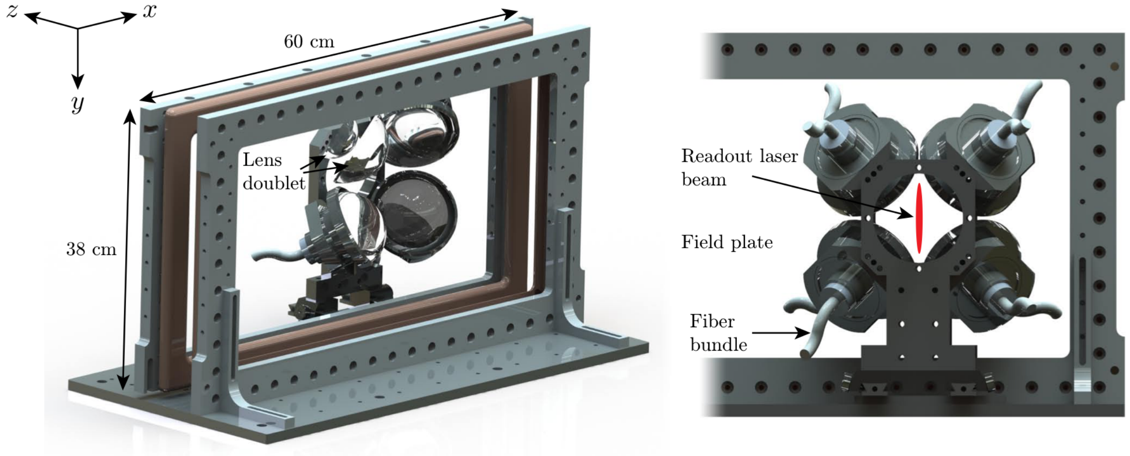

FIGURE 2.5: Field plates used to produce the static electric field, depicted together with the fluorescence collection optics, figure from [9]. Only one of two sets of four lens doublets is shown. Note that in the second generation the fiber bundles are replaced by light pipes. The right view shows the elongated beam shape of the readout laser. This high intense laser beam propagating through windows and field plates is responsible for thermally-induced birefringence causing the leading systematic error mechanism in ACME's first-generation measurement. The thermally-induced birefringence in the field plates is a particular focus of Sec. 4.2.

correlated laser detuning $\Delta^{\mathcal{N}\mathcal{E}}$ is caused by the non-reversing component of the electric field $\mathcal{E}^{\rm nr} \sim 5\,{\rm mV/cm}$. The circular polarization gradient is caused by thermally-induced birefringence in the electric field plates which is discussed in detail in Sec. 4.2. Fig. 2.5 shows the electric field plates together with the fluorescence optics. As the high-power elongated laser beam (illustrated on the right view in Fig. 2.5) passes through the field plates, some heat is deposited in the glass as well as in the coating.[7] This heat leads to mechanical stress and at the end causes a spatially dependent birefringence. Since the intensity varies along the beam, an ellipticity gradient is imprinted. This ellipticity gradient maps onto the molecule state we prepare and read out in a way that an EDM-like phase is produced.

It was demonstrated that the systematic due to AC Stark shift phases can be suppressed by aligning the laser beam polarization with the birefringence axis, by a chopper wheel reducing the time-averaged laser power, and by the shaping of the laser beam profile [9, 8]. Nevertheless, an uncertainty corresponding to a false EDM on the order of $10^{-29}\,e\cdot{\rm cm}$ remains. This thesis demonstrates that in the second generation ACME setup, the ellipticity gradient is one to two orders of magnitude lower than in the first generation. Assuming that the mechanism of detuning-correlated AC Stark shift phases scales approximately linearly with the magnitude of the circular polarization gradient [9], we conclude that in the second generation this systematic error is anticipated to produce a false electron EDM of less than $\sim 10^{-30} - 10^{-31}\,e\cdot{\rm cm}$.

---

[7] The intense laser beam also passes through the vacuum windows. In the first generation the windows were made of BK-7 glass which can substantially contribute to thermal effects. The second-generation fused silica windows produce no significant thermally-induced birefringence, see Fig. 4.10.

3 Self-calibrating Polarimeter to measure Stokes Parameters

The leading systematic errors in the first-generation ACME experiment are due to imperfect polarizations of the laser beams used to manipulate the states in the molecules [9, 8]. In particular, circular polarization gradients resulting from the thermally-induced birefringence of the electric field plates affect the spin precession measurement and contribute substantially to a systematic error mechanism. The second-generation field plates are designed to suppress this effect and require a test of their polarization properties. The goal of this work is to construct a polarimeter with an improved performance that allows to carefully characterize the polarization state of the ACME experiment lasers, in particular the ellipticity present in the laser beam. Though to some extent the systematic error due to thermally-induced birefringence can be minimized [9, 8], a precise characterization of light polarization in the future generations of ACME is needed to identify or exclude other possible sources of systematic errors related to the imperfect polarization in the electron electric dipole moment measurement. Therefore, a major part of this thesis is dedicated to the development of a polarimeter matching the requirements by ACME, one of which is the use at intensities of up to a hundred $\mathrm{mW/mm^2}$ whereas commercial polarimeters are specified for intensities lower by one or two orders of magnitude [44, 92, 80]. Furthermore, the improved design presented here is immune to intensity fluctuations and features a novel calibration technique. The carefully analyzed uncertainties demonstrate an order-of-magnitude increase in precision compared to previous laboratory realizations or commercial polarimeters.

This chapter reports on this polarimeter for the precise determination of the relative Stokes parameters that characterize the polarization state of laser light. The structure is as follows: After a brief introduction into polarimetry in the first section and an overview of Stokes parameters in Sec. 3.2, the working principle of the rotating waveplate polarimeter is presented in Sec. 3.3. The laboratory realization and the compensation of intensity noise in the measured laser beam, which is crucial for the measurement precision, are summarized in Sec 3.4. Sec. 3.5 describes an optimized in-situ calibration technique without the need to remove or realign optical elements which minimizes the calibration uncertainties. Finally, the last section, Sec. 3.6, shows the study of uncertainties which ensures the high accuracy of the absolute polarization measurement.

3.1 Introduction into Polarimetry

Light polarimetry is important in many fields of physics [85]. In atomic physics, polarization of light reveals information about interactions between excited states and the atomic state structure [61]. Among many applications in astronomy [45], the polarization of light that has traveled through interstellar dust provides information about the background magnetic field that aligns the dust [2, 37]. Light polarization also probes the magnetic field in the plasmas used for nuclear fusion studies [50]. When light propagates through plasma, magnetic fields can change the polarization of light, either through rotating the linear polarization (Faraday effect) or changing the ellipticity (Cotton-Mouton effect). Polarimeters are also used in geophysics [86] and biomedical diagnostics [1]. As mentioned previously, for the most precise measurement of the electron's electric dipole moment, polarimetry is crucial for understanding the mechanisms that dominantly contribute to the systematic uncertainty [8].

Drawing upon the early work of G. G. Stokes [90, 89], various methods are available to measure the light polarization [36]. In the so-called 'division of amplitude' method, light is split to travel along optical paths with differing optical elements, the polarization state being deduced from the relative intensities transmitted along the paths [6, 5, 69, 42]. Alternatively, the light can be analyzed using optical elements whose properties vary spatially ('division of wavefront polarimetry'), with the polarization revealed by the spatially varying intensity [17, 104, 59]. Lower precision is typically attained using the two above methods as compared to the technique we follow, called 'rotating element polarimetry'. Instead of dividing or splitting the laser-beam, the orientation of an optical component is varied over time to obtain an intensity modulated series of measurements. In our case, the polarimeter is comprised of a rotating retarder, more specifically a quarter-waveplate, and a fixed analyzer. Based on previous experimental realizations [12, 43], this thesis presents an improved design of a rotating waveplate polarimeter.

Commercial polarimeters similar to the one presented here lack the internal calibration mechanism, the immunity to intensity fluctuations and a detailed error analysis. They attain uncertainties on the order of 1% in the relative Stokes parameters, and can typically handle up to several $\mathrm{mW/mm^2}$ [44, 92, 80]. The ACME experiment requires operating intensities of up to a hundred $\mathrm{mW/mm^2}$ with the best possible polarimeter accuracy. The polarimeter design presented in this thesis is easy to realize and is robust in its operation. With a calibration procedure introduced in Sec. 3.5, it is straightforward to internally calibrate the polarimeter without the need to remove or realign optical elements. The polarimeter is designed to be largely immune to intensity fluctuations and has been used at the high intensities required by ACME. The relative fraction of circularly polarized light can typically be measured with an uncertainty below 0.1 % as discussed in Sec. 3.6.

3.2 Stokes Parameters

In this section, the Stokes formalism which is needed for the description of the polarimeter is introduced. G. G. Stokes discovered [89, 90] that the polarization state of a beam of light at a particular point in space can be fully described by four measurable quantities which are called the Stokes parameters and are summarized in the Stokes vector. This representation is very useful for two reasons. First, the Stokes parameters allow for a description of partially polarized light in a practical form and second, they can be easily measured. Stokes showed that fully polarized light and partially polarized light can be characterized, in principle, by intensities transmitted after the light passes through each of four simple configurations of optical elements:

$$I = I(0^\circ) + I(90^\circ) = I(45^\circ) + I(-45^\circ) = I_{\mathrm{RHC}} + I_{\mathrm{LHC}}, \tag{3.1a}$$

$$M = I(0^\circ) - I(90^\circ), \tag{3.1b}$$

$$C = I(45^\circ) - I(-45^\circ), \tag{3.1c}$$

$$S = I_{\mathrm{RHC}} - I_{\mathrm{LHC}}. \tag{3.1d}$$

The total intensity I, and the two linear polarizations M and C, are given in terms of intensities $I(\alpha)$ measured after the light passes through a perfect linear polarizer whose transmission axis is oriented at an angle α with respect to the polarization of the incoming light. The circular polarization S is the difference between the intensity of right- and left-handed circularly polarized light, I_{RHC} and I_{LHC}.

S can be measured by putting a perfect quarter-waveplate before the linear polarizer. If $I_{\mathrm{QWP}}(\alpha, \beta)$ is the intensity of light after the beam first passes through a perfect quarter-waveplate with the fast axis given by the angle β and then through a linear polarizer whose axis is given by the angle α, the last Stokes parameter is given by [36]:

$$S = I_{\mathrm{RHC}} - I_{\mathrm{LHC}} = 2I_{\mathrm{QWP}}(45^\circ, 0^\circ) - I, \tag{3.2}$$

where I is obtained from Eq. 3.1a. Therefore, the Stokes parameters are in principle determined by the four directly measurable intensities $I(0^\circ)$, $I(90^\circ)$, $I(45^\circ)$, and $I_{\mathrm{QWP}}(45^\circ, 0^\circ)$. (Note that $I(-45^\circ)$ can be inferred from other intensities following Eq. 3.1a.) However, this simple method assumes a perfect orientation of optical elements by 90° and 45°, and an ideal quarter-waveplate. Furthermore, the simultaneous determination of all the parameters without removing or reinserting the waveplate is not realized. As we shall see, the method of a rotatable waveplate is much more robust, precise, allows for an imperfection in the retardance of the quarter-waveplate, and enables a measurement of all the relative Stokes parameters without modifying the setup.

Let us now relate the Stokes parameters to the more familiar representation of the electric field. At any instant point in space and time, the electric field of a light wave points in a particular direction. If the electric field follows a repeatable path during its oscillations, the light wave is said to be polarized. Averaged over some time which is long compared to the oscillation period of the light, however, the light may be only partially polarized or even completely unpolarized if the direction of the electric field varies in a non-periodic way. Partial elliptical polarization is the most general polarization state. In cartesian coordinates, the time-dependent electric field $\vec{\boldsymbol{\mathcal{E}}}$ of the plane wave traveling in the z direction with frequency ω and wavenumber k can be written as:

$$\vec{\boldsymbol{\mathcal{E}}} = \hat{\mathbf{x}}\,\mathcal{E}_{0x}\cos(\omega t - kz + \phi) + \hat{\mathbf{y}}\,\mathcal{E}_{0y}\cos(\omega t - kz), \tag{3.3}$$

where $\mathcal{E}_{0x}$ and $\mathcal{E}_{0y}$ are the absolute values of orthogonal electric field components, and ϕ represents the phase difference between the two orthogonal components.

A fully polarized electromagnetic plane wave is characterized by three parameters: $\mathcal{E}_{0x}$, $\mathcal{E}_{0y}$, and the relative phase ϕ. However, usually the relative phase as well as the absolute values of the amplitudes fluctuate, so that the direction of the electric field vector changes randomly over time. In this case, light is unpolarized or only partially polarized. The amplitudes $\mathcal{E}_{0x}$ and $\mathcal{E}_{0y}$ and the phase ϕ fluctuate enough so that an average over time reduces the size of the average correlations between electric field components. The Stokes formalism accounts for an additional parameter which is needed to resolve the degree of polarization. Therefore, in general four parameters describe a light wave in a particular point in space over an averaged time period. The Stokes vector, defined with respect to the polarization measured in the plane perpendicular to the propagation direction $\hat{k}$, is given by

$$\vec{S} = \begin{pmatrix} I \\ M \\ C \\ S \end{pmatrix} = \begin{pmatrix} \langle\mathcal{E}_{0x}\rangle^2 + \langle\mathcal{E}_{0y}\rangle^2 \\ \langle\mathcal{E}_{0x}\rangle^2 - \langle\mathcal{E}_{0y}\rangle^2 \\ 2\,\langle\mathcal{E}_{0x}\mathcal{E}_{0y}\cos\phi\rangle \\ 2\,\langle\mathcal{E}_{0x}\mathcal{E}_{0y}\sin\phi\rangle \end{pmatrix}, \tag{3.4}$$

where $\langle\cdot\rangle$ indicates the time average which is needed to express the polarization state through measurable intensities.

Note that we defined the Stokes vector for planar waves. It can be proven that in the case of a superposition of plane waves the total Stokes vector is the sum of the individual Stokes vectors [36]. Since any wave can be represented through a superposition of plane waves via the Fourier transform, the Stokes formalism is valid for any light waves. Because the fast oscillating term $\cos(\omega t)$ averages out, the Stokes parameters are independent of the frequency of light and can be applied to any light source, not only to a monochromatic one.

In addition to the requirement of an averaging interval long enough compared to the oscillation period, the average time should be long enough compared to the inverse bandwidth $\Delta\nu$ of the Fourier components that describe the light, or equivalently to the coherence time $\tau \simeq 1/\Delta\nu$. The reason is that Stokes parameters are determined in terms of intensity. Within a time interval smaller than the coherence time, the different frequency components can cause a beat note in the intensities which would cause the Stokes parameters to be ill-defined.

Let us now consider the difference between the squared total intensity I and the sum of the remaining squared Stokes parameters:

$$\begin{aligned} I^2 - (M^2 + C^2 + S^2) &= 4\left(\langle E_{0x}^2\rangle\langle E_{0y}^2\rangle - \langle E_{0x}E_{0y}\cos\phi\rangle^2 - \langle E_{0x}E_{0y}\sin\phi\rangle^2\right) \\ &\geq 4\langle E_{0x}^2\rangle\langle E_{0y}^2\rangle\left(1 - \langle\cos\phi\rangle^2 - \langle\sin\phi\rangle^2\right) \geq 0, \end{aligned} \tag{3.5}$$

where we used the Cauchy-Schwarz inequality $\langle x^2\rangle\langle\, y^2\rangle \geq \langle x\, y\rangle^2$. Therefore, the following relation between the four Stokes parameters is true:

$$M^2 + C^2 + S^2 \leq I^2, \tag{3.6}$$

with equality in the case of fully polarized light. The degree of polarization P that survives the averaging is defined as:

$$P = \frac{\sqrt{M^2 + C^2 + S^2}}{I} \leq 1, \tag{3.7}$$

The unpolarized part of the light contributes only to the first of the four Stokes parameters, I, and not to M, C or S. In general, any Stokes vector can be written as a superposition of a fully polarized and a fully unpolarized part [36]:

$$\vec{S} = \vec{S}_{\text{pol}} + \vec{S}_{\text{unpol}} = \begin{pmatrix} IP \\ M \\ C \\ S \end{pmatrix} + \begin{pmatrix} I(1-P) \\ 0 \\ 0 \\ 0 \end{pmatrix}, \tag{3.8}$$

where IP and $I(1-P)$ are the polarized and unpolarized parts of intensity, respectively.

Points on the Poincaré sphere (Fig. 3.1) represent the elliptical polarization state with a relative Stokes vector

$$\vec{s} = \begin{pmatrix} M/I \\ C/I \\ S/I \end{pmatrix} = \begin{pmatrix} \cos 2\chi \cos 2\psi \\ \cos 2\chi \sin 2\psi \\ \sin 2\chi \end{pmatrix}. \tag{3.9}$$

The linear rotation angle is defined by $\tan 2\psi = C/M$. The ellipticity angle is defined by

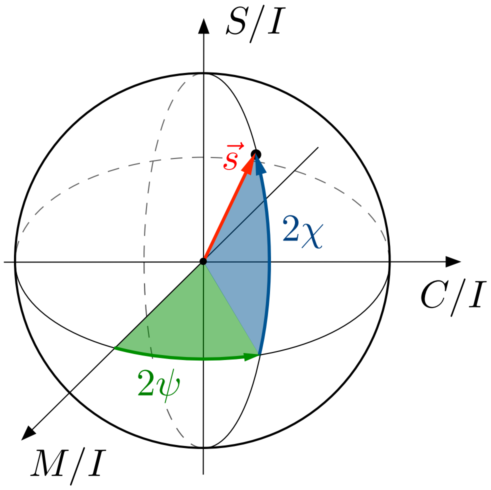

FIGURE 3.1: The three relative Stokes parameters on three orthogonal axes trace out the Poincaré sphere, with each point on the surface representing a possible state of fully polarized light. An example of a particular polarization state with the red relative Stokes vector $\vec{s}$ is shown. According to Eq. 3.9, the linear rotation angle is ψ and the ellipticity angle is χ.

$S/I = \sin 2\chi$. When $P = 1$, the light is completely polarized and the polarization vector lies on the Poincaré sphere. For partially polarized light, the length of the polarization vector is shortened such that it will now describe a point inside the sphere. When $P = 0$, the light is fully unpolarized.

While I describes the total light intensity, the dimensionless quantities M/I, C/I and S/I determine the polarization state of light. The linear polarization fraction is $L/I = \sqrt{(M/I)^2 + (C/I)^2}$ and the circular polarization fraction is S/I, with

$$(L/I)^2 + (S/I)^2 = P^2 \leq 1. \tag{3.10}$$

Because the relative intensities are summed in quadrature, in the case of fully polarized light nearly complete linear polarization (e.g. $L/I = 99\%$) corresponds to a still substantial circular polarization (e.g. $S/I = 14\%$).

Optical elements typically change the Stokes vector. Simple linear optical elements can be described by a Jones matrix which relates the electric field incident on the optical elements to the electric field that leaves the elements [36]. Equivalently[1], a Mueller matrix $\hat{M}$ transforms an input Stokes vector into the Stokes vector for the light leaving the optical elements [36],

$$\vec{S}_{\text{out}} = \hat{M}\ \vec{S}_{\text{in}}. \tag{3.11}$$

The explicit forms of most important Mueller matrices are written in App. A.2. In the formalism of Jones and Mueller matrices one assumes that an optical element changes

---

[1] A Mueller matrix $\hat{M}$ can be obtained from the corresponding Jones matrix $\hat{J}$ as $\hat{M} = \hat{A}\,(\hat{J} \otimes \hat{J}^*)\,\hat{A}^{-1}$ where $\hat{A} = ((1,0,0,1),(1,0,0,-1),(0,1,1,0),(0,\mathrm{i},-\mathrm{i},0))$ is the complex matrix needed for this transformation [34].

the incoming Stokes vector $\vec{S}_{\text{in}}$ linearly, i.e. such that the outgoing Stokes vector $\vec{S}_{\text{out}}$ can be expressed through a linear combination of the incoming Stokes parameters. This assumption is valid for linear interactions between the light and the optical device. Non-linear interactions like frequency doubling or parametric mixing are not considered within these formalisms. These non-linear effects start to occur at very high photon fluxes and determine the limit of the applicability of Jones and Mueller calculus [54].

3.3 Measurement Principle of a Rotating Waveplate Polarimeter

The Stokes vector $\vec{S}_{\text{in}} = (I, M, C, S)$ can be measured by mapping the four Stokes parameters of the incident light beam to the intensity of the outgoing beam, I_{out}. This technique relies on using optical elements with well-known polarization altering properties. The general scheme of a rotating waveplate polarimeter is shown in Fig. 3.2. Light travels first through a quarter-waveplate which can be rotated to determine the polarization state. After the light passes through a linear polarizer, the outgoing intensity is measured by the photodetector. All optical elements are aligned such that they are in planes perpendicular to the optical axis. As we shall see later, the polarizer is rotated to internally calibrate the waveplate retardance δ, the angular location of the fast axis of the waveplate β_0, and the orientation angle of the linear polarizer transmission axis α_0.

Although the measurement axis of the polarimeter is normal to its optics, the choice of the reference plane (shaded in Fig. 3.2) is arbitrary. We typically choose this plane to be aligned with the transmission axis of a calibration polarizer, through which we can

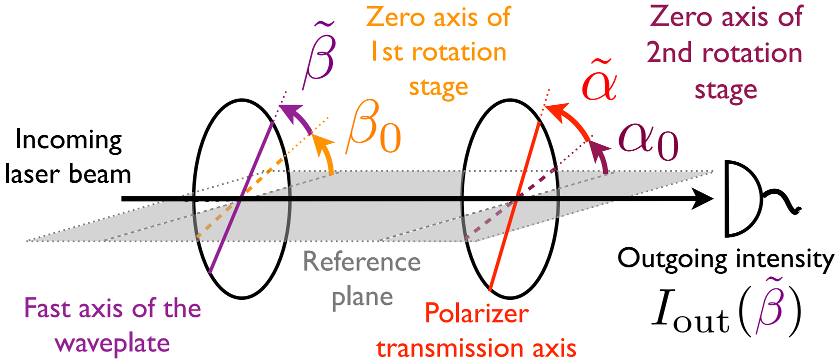

FIGURE 3.2: General scheme of a rotating waveplate polarimeter, comprised of a rotatable quarter-waveplate followed by a linear polarizer and a detector. The axes of the optical elements are specified w.r.t. a reference plane. The incoming laser-beam first passes through the waveplate with retardance δ whose fast axis is oriented at an angle $\beta_0 + \tilde{\beta}$ w.r.t. the reference plane. In combination with the polarizer (with transmission axis at an angle $\alpha_0 + \tilde{\alpha}$ w.r.t. the reference plane) the outgoing intensity is modulated. The intensity modulation $I_{\text{out}}(\tilde{\beta})$ is recorded by a photodetector as a function of the rotation degree of the waveplate.

pass light before it enters the polarimeter. With respect to this reference plane, the fast axis of the waveplate has an angle $\beta = \tilde{\beta} + \beta_0$, where $\tilde{\beta}$ is the angle of the fast axis of the quarter-waveplate with respect to an initially unknown offset angle β_0. Analogously, the transmission axis of the polarizer is $\alpha = \tilde{\alpha} + \alpha_0$, where $\tilde{\alpha}$ is the angle of the polarizer transmission axis with respect to an initially unknown offset angle α_0. The offset angles α_0 and β_0 represent the zero axes of the two rotation stages needed to rotate the optical components. The linear polarizer transmission angle α is left fixed during a determination of the four Stokes parameters for the incident light, and we typically set $\tilde{\alpha} = 0$ so that $\alpha = \alpha_0$. For the internal calibration procedure the linear polarizer is rotated by an angle $\tilde{\alpha} = 45°$. This calibration procedure, explained in Section 3.5, determines β_0, α_0 and the retardance of the waveplate $\delta \approx \pi/2$.

A succession of two Mueller matrices describes the rotating waveplate polarimeter of Fig. 3.2:

$$\vec{S}_{\text{out}} = \hat{P}(\alpha)\ \hat{\Gamma}(\delta, \beta)\ \vec{S}_{\text{in}}, \tag{3.12}$$

where $\hat{\Gamma}(\delta, \beta)$ is the Mueller matrix for a waveplate with a retardance δ whose fast axis is oriented at an angle β with respect to a reference plane. The Mueller matrix for a linear polarizer with transmission axis oriented at an angle α with respect to the reference plane is $\hat{P}(\alpha)$. Their explicit forms are given in App. A.2. In order to extract the Stokes parameters of the incoming light, $\vec{S}_{\text{in}}$, we use a photodetector to measure the intensity of the output light, I_{out}, which is the first component of the outgoing Stokes vector $\vec{S}_{\text{out}}$. The evaluation of the Mueller matrices in Eq. 3.12 leads to

$$\begin{aligned} I_{\text{out}}(\tilde{\beta}) = \;\; & I \;\; + S \sin\delta \sin(2\alpha_0 + 2\tilde{\alpha} - 2\beta_0 - 2\tilde{\beta}) \\ & + C \Big[\cos\delta \sin(2\alpha_0 + 2\tilde{\alpha} - 2\beta_0 - 2\tilde{\beta}) \cos(2\beta_0 + 2\tilde{\beta}) \\ & \qquad + \cos(2\alpha_0 + 2\tilde{\alpha} - 2\beta_0 - 2\tilde{\beta}) \sin(2\beta_0 + 2\tilde{\beta})\Big] \\ & + M \Big[\cos\delta \sin(2\alpha_0 + 2\tilde{\alpha} - 2\beta_0 - 2\tilde{\beta}) \sin(2\beta_0 + 2\tilde{\beta}) \\ & \qquad + \cos(2\alpha_0 + 2\tilde{\alpha} - 2\beta_0 - 2\tilde{\beta}) \cos(2\beta_0 + 2\tilde{\beta})\Big]. \end{aligned} \tag{3.13}$$

This result is in agreement with Stokes [89] for the special case of $\tilde{\beta} = \beta_0 = 0$, and with [12, 43, 76]. Setting $\delta = \pi/2$, $\tilde{\alpha} = \alpha_0 = 0$ and $\tilde{\beta} = \beta_0 = 0$ we obtain Eq. 3.2. Note that since we aim to determine the polarization state, we can ignore an overall constant pre-factor in Eq. 3.13 coming from possible absorbance in the optical elements or the intensity to photodetector voltage conversion.

The I, M, C and S, upon which the measured intensity I_{out} depends, are the Stokes parameters of the incident beam which we wish to determine. A measured signal on the polarimeter detector in Fig. 3.3 illustrates the variation of the transmitted intensity with the waveplate angle $\tilde{\beta}$ that is described in Eq. 3.13. From Eq. 3.13 one can identify the constant, the double-frequency and the quadrupole frequency components in terms of the rotation degree $\tilde{\beta}$. In terms of its Fourier coefficients, Eq. 3.13 can be written as

$$I_{\text{out}}(\tilde{\beta}) = C_0 + C_2\cos(2\tilde{\beta}) + S_2\sin(2\tilde{\beta}) + C_4\cos(4\tilde{\beta}) + S_4\sin(4\tilde{\beta}), \tag{3.14}$$

with the Fourier coefficients

$$C_0 = I + \frac{1+\cos(\delta)}{1-\cos(\delta)}\cdot[C_4\cos(4\alpha_0 + 4\tilde{\alpha} - 4\beta_0) + S_4\sin(4\alpha_0 + 4\tilde{\alpha} - 4\beta_0), \tag{3.15a}$$

$$C_2 = S\sin\delta\sin(2\alpha_0 + 2\tilde{\alpha} - 2\beta_0), \tag{3.15b}$$

$$S_2 = -S\sin\delta\cos(2\alpha_0 + 2\tilde{\alpha} - 2\beta_0), \tag{3.15c}$$

$$C_4 = \frac{1-\cos(\delta)}{2}[M\cos(2\alpha_0 + 2\tilde{\alpha} - 4\beta_0) - C\sin(2\alpha_0 + 2\tilde{\alpha} - 4\beta_0)], \tag{3.15d}$$

$$S_4 = \frac{1-\cos(\delta)}{2}[M\sin(2\alpha_0 + 2\tilde{\alpha} - 4\beta_0) + C\sin(2\alpha_0 + 2\tilde{\alpha} - 4\beta_0)]. \tag{3.15e}$$

We conclude that circular polarization, expressed through S, only contributes to S_2 and C_2 coefficients, whereas the Stokes parameters related to linear polarization, M and C, contribute to C_0, S_4 and C_4.

Inverting Eqs. 3.15 determines the Stokes parameters of the incoming light in terms of the Fourier coefficients:

$$I = C_0 - \frac{1+\cos(\delta)}{1-\cos(\delta)}\cdot[C_4\cos(4\alpha_0 + 4\tilde{\alpha} - 4\beta_0) + S_4\sin(4\alpha_0 + 4\tilde{\alpha} - 4\beta_0), \tag{3.16a}$$

$$M = \frac{2}{1-\cos(\delta)}[C_4\cos(2\alpha_0 + 2\tilde{\alpha} - 4\beta_0) + S_4\sin(2\alpha_0 + 2\tilde{\alpha} - 4\beta_0)], \tag{3.16b}$$

$$C = \frac{2}{1-\cos(\delta)}[S_4\cos(2\alpha_0 + 2\tilde{\alpha} - 4\beta_0) - C_4\sin(2\alpha_0 + 2\tilde{\alpha} - 4\beta_0)], \tag{3.16c}$$

$$S = \frac{C_2}{\sin(\delta)\sin(2\alpha_0 + 2\tilde{\alpha} - 2\beta_0)} = \frac{-S_2}{\sin(\delta)\cos(2\alpha_0 + 2\tilde{\alpha} - 2\beta_0)}. \tag{3.16d}$$

The Stokes parameters are thus determined by the Fourier coefficients that are extracted from measurements like the one in Fig. 3.3, along with the values of the angles α_0, β_0 and δ from the calibration to be described. The angle $\tilde{\alpha}$ is zero during a polarization measurement and is stepped away from zero only during a calibration, see Sec. 3.5.

Both of the two expressions for S must be used cautiously given the possibility that a denominator could vanish. Combining them gives a more robust expression that is independent of the two calibration angles, α_0 and β_0 [12],

$$S = -\text{sign}(\mathrm{S}_2)\frac{\sqrt{\mathrm{C}_2^2 + \mathrm{S}_2^2}}{\sin(\delta)}. \tag{3.17}$$

We choose to make the angle $2(\alpha_0 - \beta_0)$ small, whereupon $|S_2| > |C_2|$ for nonvanishing S and the sign of S is that of $-S_2$. Similarly, combining equations (3.16b) and (3.16c) gives

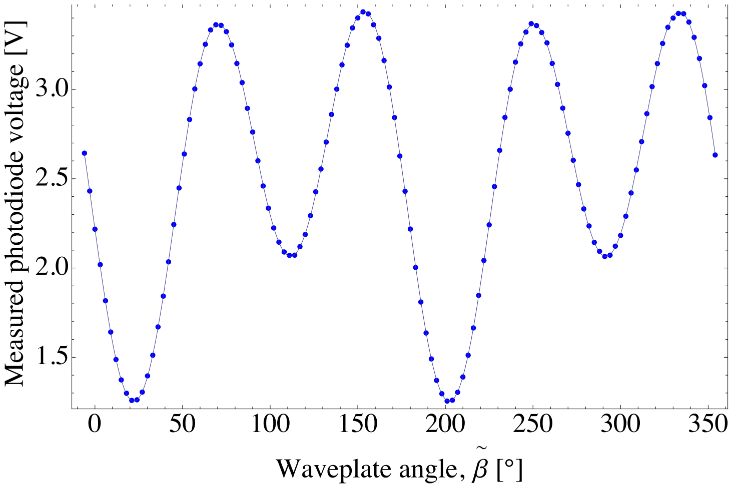

FIGURE 3.3: Illustration of how the light intensity transmitted through the polarimeter varies with the waveplate rotation angle $\tilde{\beta}$ as predicted by Eq. 3.13. The first component of the outgoing Stokes vector, which is the total intensity I_{out} proportional to the detector voltage U_{out}, is measured as a function of the rotation degree $\tilde{\beta}$ of the waveplate. The constant, the double-frequency and the quadruple frequency components (see Eqs. 3.13-3.14) from which one can extract the Stokes parameters of the incoming laser beam are clearly visible.

a more robust expression for the magnitude of the linear polarization $L = \sqrt{M^2 + C^2}$, independent of α_0 and β_0,

$$L = \frac{\sqrt{C_4^2 + S_4^2}}{\sin^2\left(\frac{\delta}{2}\right)}. \tag{3.18}$$

Both S/I and L/I still depend on all of the calibration angles since I does, but the use of the more robust expressions for S and L can reduce the uncertainties in S/I and L/I.

3.4 Laboratory Realization and Intensity Normalization

The laboratory realization of a rotating waveplate polarimeter, see Fig. 3.4, utilizes a quarter-waveplate (Thorlabs WPQ05M-1064), a polarizer (Thorlabs GL10-B) and two detectors (Thorlabs PDA100A). The waveplate is mounted on a first rotation stage, while the linear polarizer and the two detectors are mounted on a second rotation stage (both Newport URS50BCC). During a measurement, the angle $\tilde{\beta}$ is typically varied over time with 120 discretized values $\tilde{\beta} = \{0°, 3°, \ldots, 357°\}$ covering one full rotation of the waveplate. The linear polarizer angle can similarly be rotated for the internal calibration, though a restricted calibration rotation by $\sim 45°$ turns out to be optimal for reducing the uncertainties, as we shall see in Section 3.5.

The aperture before the polarimeter constrains the collimation of the beam inside the device. If the aperture is too large, the imperfections of optical elements (e.g. spatial inhomogeneity of the waveplate retardance) reduce the accuracy of the measurement. An

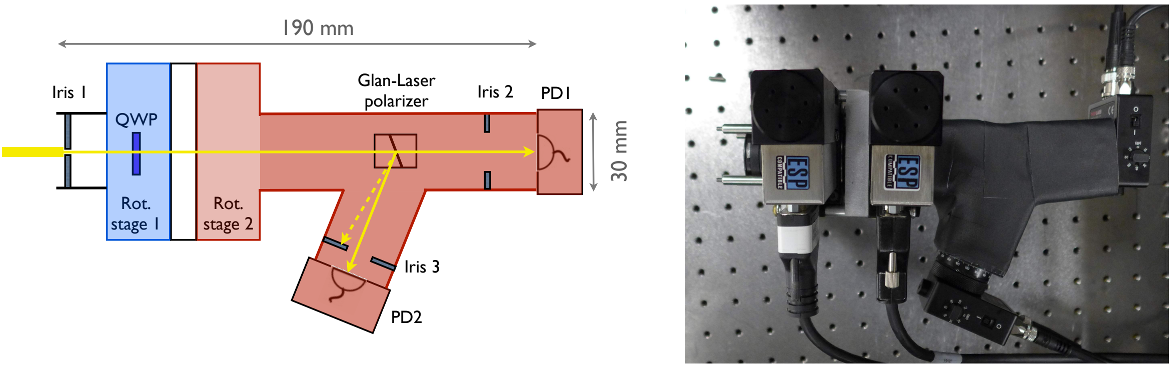

(a) (b)

FIGURE 3.4: Scale representation of the polarimeter (a) Schematic drawing with apertures, a quarter-waveplate (QWP) on the first rotating stage, and the linear Glan-Laser polarizer with the two detectors that rotate together on a second stage. The first aperture selects a small region of the laser-beam (iris diameter 1 mm) for the determination of Stokes parameters, whereas the second iris is used in combination with the first one to align the polarimeter. The first rotation stage rotates only the waveplate (in blue). The rotating parts controlled by the second rotation stage - the Glan-Laser polarizer and the two photodetectors - are depicted in red. (b) Photograph of the polarimeter on the optical table, view from the top according to the scheme in subfigure (a).

aperture which is too small results in errors due to diffraction. It was found that an aperture with a diameter of ~ 1 mm minimized the uncertainties for our measurements. Even in this case, the diffraction is still visible, as shown in Fig. 3.5(a). Fig. 3.5(b) shows measurements of the beam diameter at the distance of the polarimeter detector for the transmitted beam in dependence on the aperture size in front of the polarimeter. For aperture sizes larger than ~ 1 mm, the beam diameter becomes smaller as the aperture is closed. When the aperture size becomes smaller than ~ 1 mm, the diffraction dominates over clipping and the beam width starts to increase with a decreasing aperture size. The aperture becomes oval for diameters < 1 mm due to the design of the zero aperture iris diaphragm (part number Thorlabs SM1D12CZ).

The second aperture is placed directly in front of the detector for the transmitted beam and is used to align the polarimeter by maximizing the light admitted by the pair of apertures. The polarimeter is mounted on a kinematic alignment stage (Newport 9081). Therefore, the alignment can be performed without changing the pointing of the incoming laser beam. Note that after the alignment procedure, the aperture in front of the detector needs to be opened again as illustrated in Fig. 3.4(a) to ensure no loss of detected intensity due to diffraction.

Fluctuations in light intensity contribute to noise in the measured polarization since the Fourier components are deduced from the intensity of light transmitted through the polarimeter. Therefore, all laser intensity noise on timescales smaller than one polarimetry

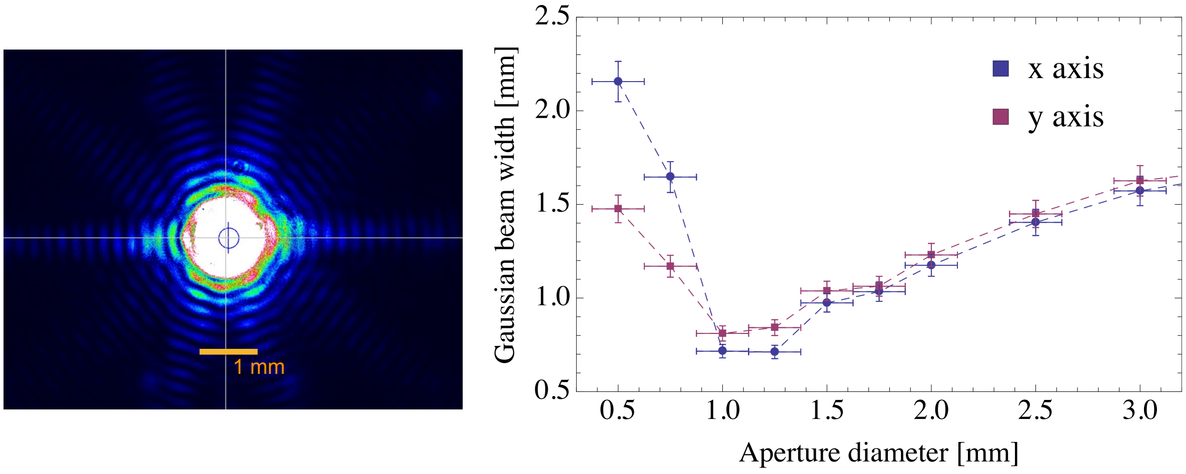

(a)

(b)

FIGURE 3.5: (a) Diffraction caused by the ~ 1 mm large aperture in front of the polarimeter at the distance of the detector for the transmitted beam. To make the diffraction pattern visible, the beam profiler is overexposed. (b) The fitted Gaussian laser beam width at the distance of the polarimeter detector for the transmitted beam in dependence on the aperture size in front of the polarimeter. For aperture sizes smaller than ~ 1 mm the beam diameter increases due to the prevailing diffraction.

measurement (around 1-3 minutes) directly affects the precision of the measured Stokes parameters. On ACME, the resulting fluctuations in S/I coming from intensity noise are typically up to $\sim 2\%$ without normalizing the intensity.

Therefore, a scheme which significantly suppresses effects of laser intensity noise on the polarimetry measurement is implemented. The following two challenges need to be taken into account for the development of the intensity normalization scheme. First, the additional components should not modify the polarization state of light inside the polarimeter since this will affect the precision of the ellipticity measurement. This requirement excludes the use of any beamsplitters in front of the polarimeter since they affect the polarization. Second, the design has to work at high powers. Taking these two requirements into consideration, the sideport of the Glan-Laser polarizer is used. Since a polarizer is needed anyway for the polarimetry measurement scheme, additional optical components are not required. Note that the Wollaston prism which is typically used for pure polarization purposes would not be suitable because of optical contacting adhesives and thus a lower damage threshold.

The Glan-Laser polarizer transmits light with one particular polarization, and sends the remaining light out through a sideport where we detect it for normalization purposes with a second detector, as shown in Fig. 3.4(a). The bandwidth of the detectors is 2.4 MHz which means that the polarimeter normalizes all intensity fluctuations on time scales larger than ~ 500 nanoseconds. The intensity of the incoming light source is proportional to the

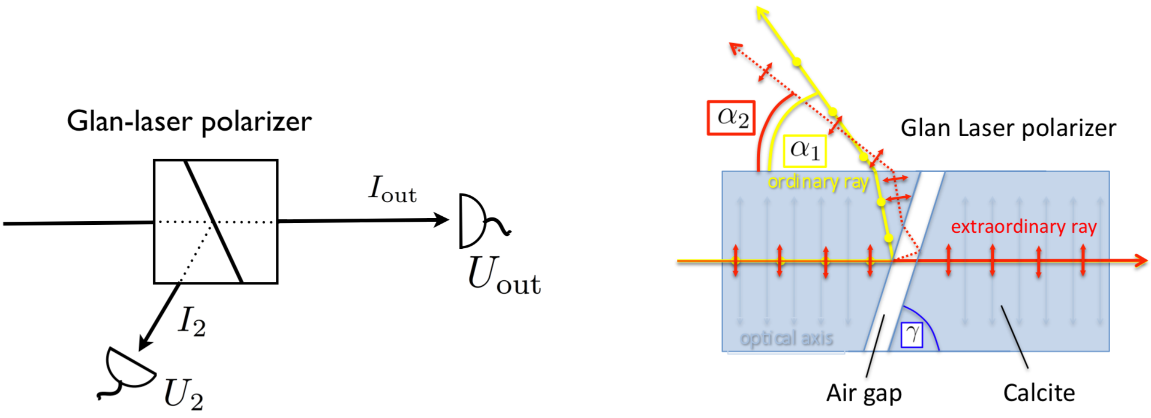

(a) (b)

FIGURE 3.6: Scheme of the Glan-Laser polarizer in the polarimeter which splits the analyzed light into transmitted and refracted beams. The refracted beam from the sideport is used to monitor the total intensity and correct for amplitude fluctuations in the light source. (a) The transmitted beam represents I_{out} from Eq. 3.13 resulting in the detector voltage U_{out}. The refracted beam from the sideport with the intensity I_2 resulting in the photodetector voltage U_2 provides the additional measurement needed for intensity normalization, see Eq. 3.21.
(b) Detailed drawing of the polarizer design, showing how a small portion of the extraordinary beam is reflected after passing the air gap and exits the sideport under an angle α_2. The ordinary beam is refracted under an angle α_1.

sum of both detector voltages. Relative gain and offset factors are applied to account for detector differences. The weighted sum signal is then used to correct the intensity of the light transmitted through the polarimeter to reduce the effect of intensity fluctuations. The calibrated offset and gain constants minimize the variation in the inferred intensity of light incident on the Glan-Laser polarizer.

For the intensity normalization of the polarimeter it is critical that the sum of the intensities of the two light beams is proportional to the total incoming intensity with a proportionality constant independent of the incoming polarization. Let us therefore examine the Glan-Laser polarizer in detail as depicted in Fig. 3.6(b). The Glan-Laser polarizer is a prism polarizer based on the principle of different critical angles for the ordinary and the extraordinary beams. In general, prism polarizers use the phenomenon of two refractive indices in an uniaxial crystal. The symmetry axis of the crystal is referred to as the optical axis. In such a crystal, e.g. calcite, the beam is separated into the beam propagating parallel and perpendicular to the optical axis, called extraordinary and ordinary rays, respectively. The two beams have different refractive indices n_e and n_o. For calcite the values are $n_e \simeq 1.485$ and $n_o \simeq 1.655$ [53]. The optical axis of the calcite crystal in the Glan-Laser polarizer is oriented perpendicular to the incoming beam. Therefore, until the reflection happening between the two parts of the Glan-Laser polarizer, the ordinary and extraordinary beams propagate in the same direction but with different velocities given by $v_o = c/n_o$ and $v_e = c/n_e$. The air gap separates the two prisms of the Glan-Laser polarizer, and is placed under the angle $\gamma \simeq 52^\circ$ w.r.t. the incoming beam, shown in blue in Fig. 3.6(b). The critical angle for the reflection of the ordinary and extraordinary rays is given by:

$$\sin\theta_{o,e} = \frac{1}{n_{e,o}}. \tag{3.19}$$

For the incoming angles $\theta > \theta_{o,e}$ or $\gamma = 90^\circ - \theta < \gamma_{o,e}$ the respective beam is subject to total reflection and is not transmitted. For calcite we obtain the values $\theta_o \simeq 37^\circ$ ($\gamma_o \simeq 53^\circ$) and $\theta_e \simeq 42^\circ$ ($\gamma_o \simeq 48^\circ$). Therefore, the two parts of the Glan-Laser polarizer have to be manufactured at an angle $48^\circ \lesssim \gamma \lesssim 53^\circ$ so that the ordinary beam is totally reflected whereas the extraordinary beam is transmitted.

The air gap, combined with the second part of the Glan-Laser polarizer, produces a second beam coming out of the sideport of the polarizer, as shown with the red dotted line in Fig. 3.6(b). Since this beam represents a small fraction of the transmitted extraordinary beam which is dependent on the incoming polarization, it can introduce an error in the intensity normalization scheme. However, this small part of the reflected extraordinary beam exits the polarizer at a different angle α_2 compared to the refracted ordinary beam with an exit angle α_1, as shown in Fig. 3.6(b). The angles were measured to be $\alpha_1 \simeq 66 \pm 2^\circ$ and $\alpha_2 \simeq 59 \pm 2^\circ$. This difference results from a different refractive index of the ordinary and the extraordinary beams. The latter is dependent on the beam direction w.r.t. the optical axis [68]. If the extraordinary and ordinary beams both propagate in the direction of the optical axis, their refractive index is equal. This could be the scenario for the ordinary and the reflected extraordinary beams which we consider in Fig. 3.6(b), though it is not the case.

It is important to ensure that the reflected part of the extraordinary beam coming out from the sideport together with the ordinary beam does not reach the second detector used for intensity normalization. Therefore an aperture is put before this detector, see 'Iris 3' in Fig. 3.4(a). Note that the aperture size has to be large enough to not clip part of the ordinary beam (including its diffraction tail caused by the first aperture in front of the polarimeter), but small enough to block the undesired reflected extraordinary beam.

After understanding the Glan-Laser polarizer and assuring ourselves that none of the spurious reflected beams distorts the measurement, let us consider the intensity normalization scheme in more detail. As illustrated in Fig. 3.6(a), we measure the voltages from each photodetector which are given by:

$$\begin{aligned} U_{\text{out}} &= o_{\text{out}} + g_{\text{out}}\, I_{\text{out}}, \\ U_2 &= o_2 + g_2\, I_2, \end{aligned} \tag{3.20}$$

where I_2 is the intensity of the beam from the sideport, I_{out} the intensity of the transmitted beam, o_{out}, o_2 the corresponding detector offsets and g_{out}, g_2 the gain factors. The offsets o_{out} and o_2 come from the electronics of the oscilloscope and the detector, and are typically on the order of $10 - 30$ mV. The gain factors g_{out} and g_2 are a combination of factors corresponding to the linear loss of intensity and the conversion from intensity to voltage. Therefore, the normalization scheme is insensitive to imperfections in the optics equivalent to a linear attenuation, for example different linear absorbance or scattering in the polarizer. The light in the reflection port allows us to normalize the intensity of the transmitted port as:

$$\frac{I_{\mathrm{out}}}{I} = \frac{U_{\mathrm{out}} + o_{\mathrm{out}}}{g\,(U_2 - o_2) + U_{\mathrm{out}} - o_{\mathrm{out}}}. \tag{3.21}$$

The offsets $o_{\mathrm{out}},\ o_2$ and the gain ratio $g = g_{\mathrm{out}}/g_2$ need to be determined. The electronic offsets o_{out}, o_2 can simply be measured by blocking the laser beam. It is important to monitor the offsets in the detectors from time to time since they were found to differ on a scale of $\sim$ 10 mV from day to day, and in particular after disconnecting and reconnecting the cables. Obviously, the offset also changes when some part of the BNC connector touches the optical table.

In the following two ways to measure the gain ratio are described. One simple method is to use the data from the calibration measurement with linearly polarized light described in the following section. The calibration is performed by placing a linear polarizer before the polarimeter so that the Stokes parameters C and S are zero, $C = S = 0$. In this case Eq. (3.13) reads:

$$I_{\mathrm{out}} = I - M\left[\cos\delta\sin(2\alpha_0 - 2\beta)\sin 2\beta + \cos(2\alpha_0 - 2\beta)\cos 2\beta\right]. \tag{3.22}$$

Using trigonometric identities this equation can be expressed in the form:

$$I_{\mathrm{out}} = I - M'\cos(4\beta + \phi), \tag{3.23}$$

where M' and ϕ are constants. Comparing with Eq. 3.20, the detector voltages can be written as:

$$U_{\mathrm{out},2} = c_{\mathrm{out},2} \pm g_{\mathrm{out},2}\, M'\ \cos(4\beta + \phi), \tag{3.24}$$

where $c_{\mathrm{out},2}$ are constants. The ratio of the fitted quadrupole frequency components gives the gain ratio $g = g_{\mathrm{out}}/g_2$.

A better method is to determine the gain ratio as follows. The aim is to normalize for the total intensity which is given by

$$\tilde{I}(\tilde{\beta}) = U_{\mathrm{out}}(\tilde{\beta}) - o_{\mathrm{out}} + \tilde{g}\,(U_2(\tilde{\beta}) - o_2) \tag{3.25}$$

and is recorded as a function of the waveplate rotation degree $\tilde{\beta}$. Let us assume a gain ratio $\tilde{g}$. If the assumed gain ratio $\tilde{g}$ equals the true gain ratio, the total intensity $\tilde{I}(\tilde{\beta})$ should

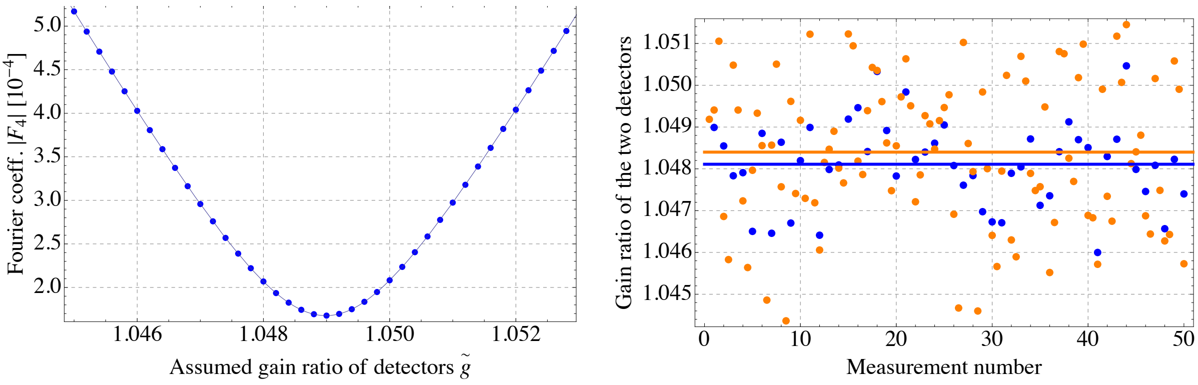

(a) (b)

Figure 3.7: Determination of the gain ratio from Eq. 3.21 needed to normalize the intensity. (a) Illustration of the second method described in the text. The gain ratio $\tilde{g}$ from Eq. 3.25 is varied to minimize the Fourier coefficient $|\tilde{F}_4|$ defined in Eq. 3.26. The value for $\tilde{g}$ where $|\tilde{F}_4|$ is minimized corresponds to the true gain ratio g we wish to find. (b) The two methods of gain determination are compared. Results of the first simple method described by Eq. 3.24 are depicted in orange. Results obtained with the second method are shown in blue. The first method yields a mean gain ratio of $\overline{g_1} = 1.0484(2)$ with a standard deviation $\sigma_1 = 1.5 \cdot 10^{-4}$. The second method yields $\overline{g_2} = 1.0481(1)$ with a standard deviation $\sigma_2 = 1.0 \cdot 10^{-4}$.

not show any variation correlated with the rotation degree of the waveplate $\tilde{\beta}$. Therefore, we can vary $\tilde{g}$ to keep $\tilde{I}$ as constant as possible with variation of $\tilde{\beta}$. Recalling Eq. 3.14, the correlation with $\tilde{\beta}$ will show up in the double-frequency and quadrupole frequency components. Therefore, for a given data set of $\tilde{I}(\tilde{\beta})$ with N measurements (typically $N = 120$ with $\tilde{\beta} = \{0°, 3°, \ldots, 357°\}$), we can calculate the Fourier series for a set of gain ratios $\tilde{g}$ and determine for which value of $\tilde{g}$ the double-frequency and quadrupole frequency components are minimized. The Fourier series coefficients are given by

$$\tilde{F}_k = \sum_{n=0}^{N-1} \tilde{I}(\tilde{\beta}_n) \cdot \mathrm{e}^{-2\pi i k n/N}. \tag{3.26}$$

The double-frequency component is resolved by the absolute value $|\tilde{F}_2|$ and the quadrupole frequency component by $|\tilde{F}_4|$. Interpolation over a set of discretized $\tilde{g}$ values determines the functions $|\tilde{F}_2(\tilde{g})|$ or $|\tilde{F}_4(\tilde{g})|$. The position of their minima corresponds to the true gain ratio g we wish to find. Note that for linearly polarized light the double-frequency components vanish whereas for circularly polarized light the quadrupole frequency components are zero, as is obvious from Eq. 3.13. Therefore, if light is dominantly linearly polarized, the coefficient $|\tilde{F}_4|$ should be used, whereas if the circular polarized fraction prevails, one should use the coefficient $|\tilde{F}_2|$.

The realization of the second method is illustrated in Fig. 3.7(a). For a range of $\tilde{g}$ values, the absolute value of the Fourier coefficient $|\tilde{F}_4|$ from Eq. 3.26 is calculated. The data points are interpolated and the position of the minimum determines the gain ratio g. In Fig. 3.7(b) the two methods for the gain ratio measurement are compared for a sequence of 50 measurements. The same data set was used for both methods. Points from the first simple method are shown in orange whereas the gain values obtained with the second method are depicted in blue. The mean values of gain ratios determined with the two methods agree within the statistical uncertainty. However, the standard deviation for the second method is smaller. Furthermore, the second method has the great advantage of being applicable to *any* incoming polarization. The gain ratio calibration can thus be incorporated into any polarimetry measurement and performed together with the data analysis using the above scheme. No separate measurements are needed in this case.

3.5 Calibration of Angles and Retardance

In order to determine the polarization properties of the incoming light, the angles α_0, β_0, and the retardance δ need to be known (recall Eqs. 3.16). There are several ways to determine these parameters [12, 43, 76]. Here we present a novel calibration technique which is fully automated and does not require to remove or realign optical components inside the polarimeter. This in situ calibration procedure is more precise than previous methods and therefore centrally responsible for the low uncertainties realized with the polarimeter presented in this thesis.

The previous calibration methods were performed as following. When the quarter-waveplate is removed, the polarizer can be aligned mechanically with the calibration polarizer by fitting Malus' law of two crossed polarizers. Doing so, one can typically achieve angle uncertainties of up to ±1°. The polarimeter has to be taken apart which likely changes alignment and takes experimenters time. Another shortcoming of this method is that the calibration cannot be performed automatically between measurements. Without removing the waveplate, it is in principle possible to acquire the calibration data for different incoming polarizations and perform a two dimensional fit. This procedure takes much more time and turns out to be even less robust than the first method. Investigations showed that this technique is unpractical and takes too much time [43]. Another technique is to place the retarder and polarizer on mounts that permit front-to-back rotation about an axis perpendicular to the direction of beam propagation [76]. This method is subject to various systematic errors due to misalignments and achieves uncertainties of only less than 1°. The technique presented in this thesis is simpler and about an order of magnitude more precise.

Similar to the methods mentioned above, we make use of the linear polarizer in order to calibrate the parameters α_0, β_0 and δ. The advance here is to mount the polarizer on the rotation stage allowing for an automated procedure with a carefully studied optimal rotation needed to minimize the calibration time and uncertainties. This calibration technique avoids realignments of optical elements caused by either temporarily removing or by flipping optical elements with respect to the light transmission axis.

The calibration procedure starts with a high extinction ratio polarizer (Thorlabs GL 10-B) placed in the light beam before it enters the polarimeter. The light analyzed by the polarimeter is in this case known to be almost fully polarized. The transmission axis of this external calibration polarizer then defines the reference plane in terms of which the linear polarizations M and C are determined. For the relative Stokes vector (1,0,0), Eqs. (3.16) simplify to

$$\begin{aligned} C_0 - \frac{1+\cos(\delta)}{1-\cos(\delta)} & [C_4 \cos(4\alpha_0 - 4\beta_0) + S_4 \sin(4\alpha_0 - 4\beta_0)] \\ & = \frac{2}{1-\cos(\delta)} [C_4 \cos(2\alpha_0 - 4\beta_0) + S_4 \sin(2\alpha_0 - 4\beta_0)], \qquad (3.27a) \\ \arctan \frac{S_4}{C_4} & = 2\alpha_0 - 4\beta_0. \qquad (3.27b) \end{aligned}$$

For the third linearly independent equation needed to determine the three calibration parameters we rotate the linear polarizer from $\tilde{\alpha} = 0$ to $\tilde{\alpha} = 45°$, a choice shortly to be justified, whereupon

$$\begin{aligned} \tilde{C}_0 - & \frac{1+\cos(\delta)}{1-\cos(\delta)} \cdot [\tilde{C}_4 \cos(4\alpha_0 + 4\tilde{\alpha} - 4\beta_0) + \tilde{S}_4 \sin(4\alpha_0 + 4\tilde{\alpha} - 4\beta_0)] \\ = & \frac{2}{1-\cos(\delta)} [\tilde{C}_4 \cos(2\alpha_0 + 2\tilde{\alpha} - 4\beta_0) + \tilde{S}_4 \sin(2\alpha_0 + 2\tilde{\alpha} - 4\beta_0)]. \qquad (3.28) \end{aligned}$$

These equations can be simplified when the waveplate is reasonably close to being a quarter-waveplate, $\cos\delta \simeq \frac{\pi}{2} - \delta$. They can be simplified further when we deliberately choose to make α_0 small, which means that the zero-axis of the internal polarizer is approximately aligned with the external polarizer that defines the reference plane for the Stokes parameters. The linearized calibration equations, derived in App. A.3, are then

$$\delta = \frac{\pi}{2} + 1 + 2\,\frac{\sqrt{C_4^2 + S_4^2} - C_0}{\sqrt{C_4^2 + S_4^2} + C_0}, \qquad (3.29a)$$

$$\alpha_0 = \frac{\cot\tilde{\alpha}}{2} - \frac{1}{\sin(2\tilde{\alpha})} \frac{\sqrt{S_4^2 + C_4^2} - \tilde{C}_0}{\sqrt{S_4^2 + C_4^2} - C_0}, \qquad (3.29b)$$

$$\beta_0 = \frac{1}{4}\left(\arctan\frac{S_4}{C_4} - 2\alpha_0\right). \qquad (3.29c)$$

The uncertainty in α_0 is determined by the standard error propagation:

$$\sigma_{\alpha_0}^2 = \left(\frac{\partial\alpha_0}{\partial\tilde{\alpha}}\right)^2 \sigma_{\tilde{\alpha}}^2 + \left(\frac{\partial\alpha_0}{\partial\tilde{C}_0}\right)^2 \sigma_{\tilde{C}_0}^2 + \left(\frac{\partial\alpha_0}{\partial C_0}\right)^2 \sigma_{C_0}^2 + \left(\frac{\partial\alpha_0}{\partial C_4}\right)^2 \sigma_{C_4}^2 + \left(\frac{\partial\alpha_0}{\partial S_4}\right)^2 \sigma_{S_4}^2, \quad (3.30)$$

with α_0 from Eq. 3.29b given our simplifying choice to make α_0 small.

To illustrate that the choice $\tilde{\alpha} \approx 45°$ minimizes uncertainties, Fig. 3.8 shows the uncertainty in α_0 for a typical choice of uncertainties in the normalized Fourier coefficients

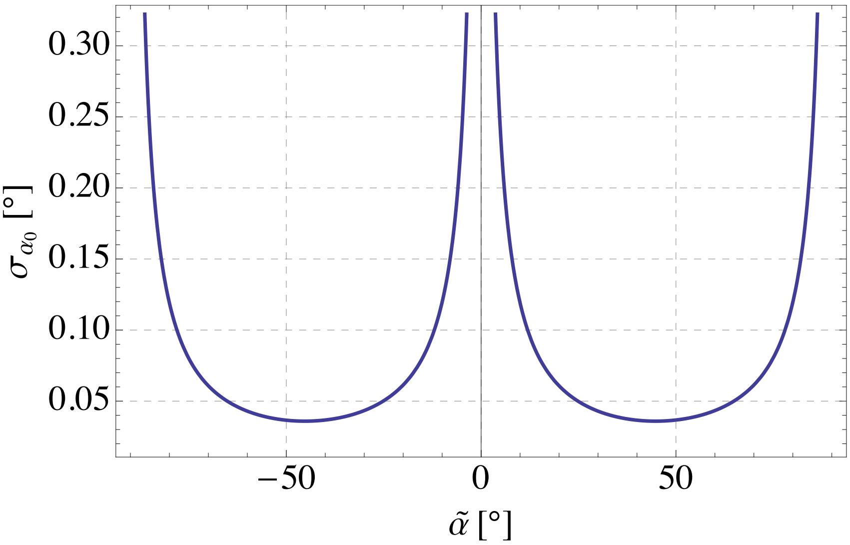

Figure 3.8: Determination of the optimal calibration angle $\tilde{\alpha}$ according to Eq. 3.30. The uncertainty σ_{α_0} of the calibration parameter α_0 is shown as a function of the change in the linear polarizer angle $\tilde{\alpha}$ during the calibration procedure. The minimum of uncertainty in α_0 demonstrates that a $45°$ step is close to the optimal value.

of 0.05% and an uncertainty in $\tilde{\alpha}$ of $0.02°$. For $\tilde{\alpha}$ close to $0°$ or $90°$ the equations (3.27) and (3.28) become degenerate and therefore the uncertainty in α_0 grows to infinity. When the uncertainties in the Fourier coefficients are approximately equal, the $45°$ choice minimizes the uncertainties in calibration parameters, typically making them less than $0.1°$.

To summarize, these are the calibration steps:

1. Place a linear polarizer before the polarimeter. Its polarization axis then defines the reference plane for the Stokes parameters M and C. Set $\tilde{\alpha} = 0$.
2. Perform at least one full rotation of the waveplate recording the output intensity $I_{\text{out}}(\tilde{\beta})$.
3. Determine the Fourier coefficients C_0, C_4, and S_4 from the scan in step 2.
4. Rotate the polarizer inside the polarimeter by $\tilde{\alpha} = 45°$ and repeat step 2.
5. Determine the Fourier coefficients $\tilde{C}_0$, $\tilde{C}_4$, and $\tilde{S}_4$ from the scan in step 4.
6. Using the Eqs. (3.27)-(3.28), calculate the calibration parameters δ, α_0, and β_0 from the measured Fourier coefficients.

3.6 Uncertainties

We recall from Eqs. 3.16 that the determination of the relative Stokes parameters depends on the calibration parameters α_0, β_0 and δ as well as the Fourier coefficients C_0, C_2, C_4, S_2, and S_4. The uncertainties arising from the calibration cause systematic errors in the measured Stokes parameters. The Fourier coefficients C_0, C_2, C_4, S_2, and S_4 are subject to both, statistical and systematic uncertainties. There are many possible systematic error sources. Much effort was invested in finding or excluding possible systematic errors. We focus on systematic uncertainties that arise from calibration parameters, waveplate imperfections, misalignment of the incident light pointing relative to the measurement axis, and the finite extinction ratio of the polarizer. The systematic errors are summarized in the last subsection 3.6.6 with Table 3.1.

Since we typically are not interested in the absolute rotation angle of polarization, we focus on errors for the degrees of circular polarization S/I and linear polarization L/I. For purposes on ACME, typically a measurement of the degree of circular polarization S/I is sufficient. From Eqs. 3.17 and 3.18 we found that the absolute values of S and L do not depend on the angles α_0 and β_0 but only on the retardance δ. However, the systematic errors due to imperfect knowledge of α_0 and β_0 enter the relative Stokes parameters S/I and L/I because the total transmitted intensity I is dependent on these angles.

3.6.1 Statistical Uncertainty

The statistical uncertainty arises from the detector, oscilloscope and data acquisition system electronic noise, digitization errors as well as residual intensity fluctuations. Fig. 3.9 shows a typical statistical fluctuation of S/I and L/I for around 300 successive measurements. This polarimetry data was obtained using a waveplate with the fast axis being almost aligned with the incident linear polarization rotation angle, resulting in only a small fraction of circular polarized light of $S/I \approx 3\%$. Subfigures (c) and (d) demonstrate that the distribution of measurement results is well in agreement with a Gaussian distribution with standard deviations of $\sigma_{S/I} = 0.0089(3)\%$ and $\sigma_{L/I} = 0.046(1)\%$. To sum up, statistical uncertainties that can be averaged down with more measurements are typically on the order of 0.01% for S/I and 0.05% for L/I. As we shall see, this is below the anticipated systematic errors. Therefore, there is no need to average down the statistical uncertainty.

3.6.2 Calibration Parameters

Let us now examine the systematic errors due to calibration parameters. Even though the expressions for S or L in Eqs. 3.17-3.18 do not depend on the angles α_0 or β_0, the impact of theses angles on the relative S/I and L/I arises from the expression for I

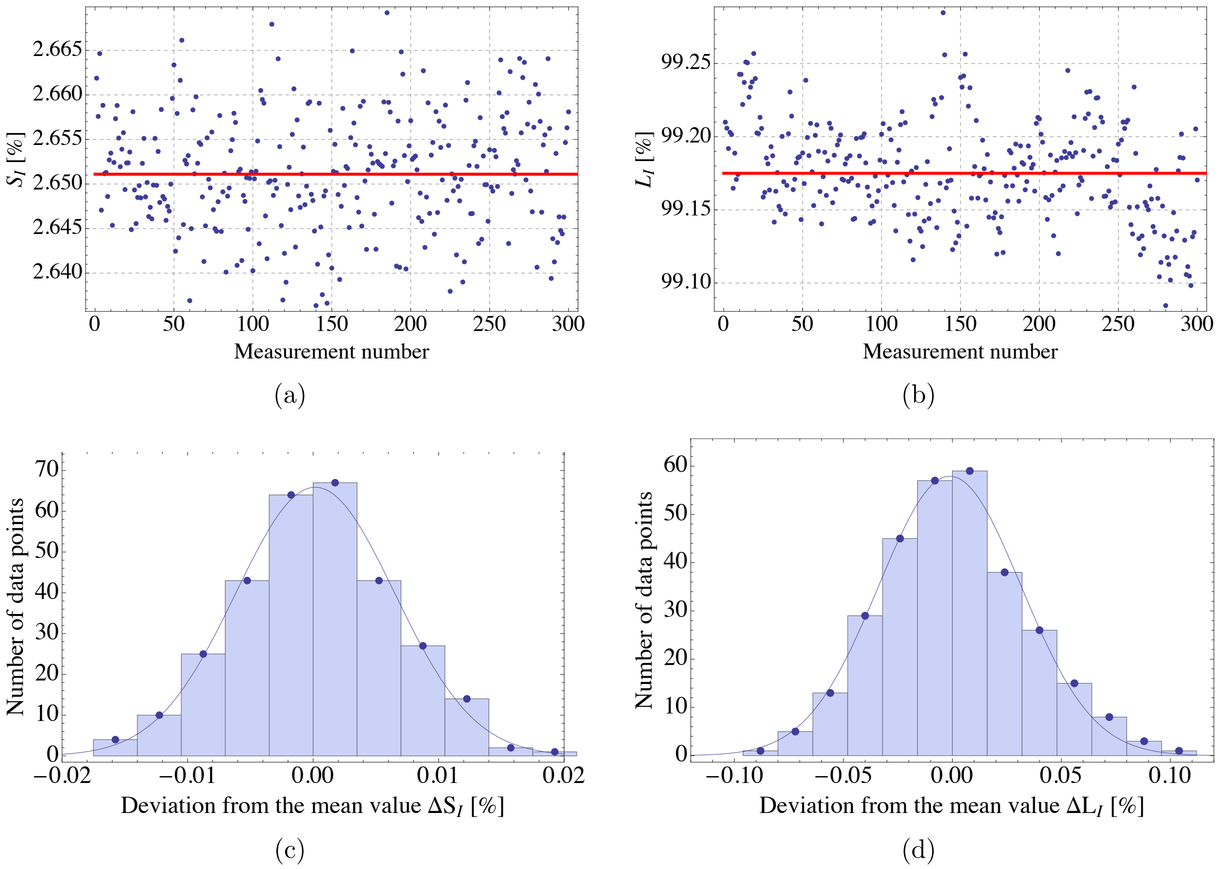

(a) (b)

(c) (d)

FIGURE 3.9: Statistical fluctuation in 300 successive measurements of S/I, subfigures (a) and (c), and L/I, subfigures (b) and (d). In (a) and (b), the red line marks the mean values. Histograms of the deviations from the mean values of $\overline{S/I} = 2.6511\%$ and $\overline{L/I} = 99.175\%$ are depicted in (c) and (d). The bin size is 0.0035% for S/I and 0.019% for L/I. A Gaussian is fitted to the histograms. The fitted standard deviations are $\sigma_{S/I} = 0.0089(3)\%$ and $\sigma_{L/I} = 0.046(1)\%$.

in Eq. 3.16a that depends on C_0, C_4 and S_4. Comparing with Eqs. 3.15a, 3.15d and 3.15e we realize that the values for C_0, C_4 and S_4 are dependent on the angles α_0 and β_0 separately. Therefore, the absolute orientation of the polarimeter w.r.t. the incoming polarization does matter for how the errors in α_0 and β_0 enter the measurement of S/I or L/I. Furthermore, I depends on the retardance δ and the Stokes parameters M and C of the incoming light. This means that the impact of calibration parameter uncertainties on S/I and L/I is dependent on the specific values of α_0, β_0, and δ, as well as on the Stokes parameters of incoming light.

Typically the calibration procedure determines the waveplate retardance to about $\delta_{\mathrm{err}} \sim 0.1^\circ$. Approximately the same uncertainty is obtained in the relative angle between the polarizer transmission axis and the initial orientation of the wave plate fast axis, $(\alpha_0 - \beta_0)_{\mathrm{err}} \sim 0.1^\circ$. We can examine how these uncertainties propagate into a systematic error on S/I and L/I numerically. When calculating the relative Stokes parameters according to Eq. 3.16 the true values of $\alpha_0 - \beta_0$ and δ are modified by $(\alpha_0 - \beta_0) \rightarrow (\alpha_0 - \beta_0) + (\alpha_0 - \beta_0)_{\mathrm{err}}$

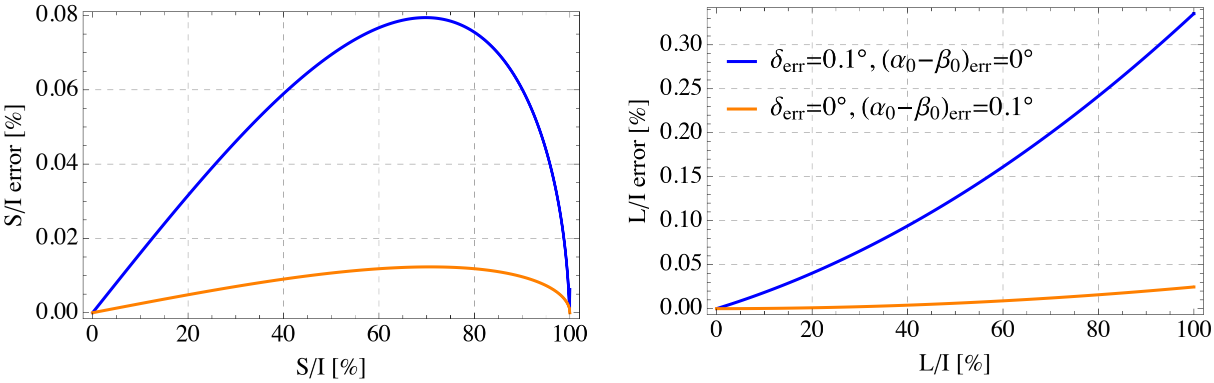

FIGURE 3.10: Calculated systematic errors in S/I (left) and L/I (right) due to calibration parameter uncertainties. The results are shown for typical calibration parameters of $\delta = 92°$, $\alpha_0 = 2°$, $\beta_0 = 20°$, and calibration uncertainties of $0.1°$ in δ (blue curve) and also for an uncertainty of $0.1°$ in $\alpha_0 - \beta_0$ (orange curve) for a range of S/I and L/I values. The curves for S/I are symmetric around zero.

and $\delta \to \delta + \delta_{\text{err}}$. We set the true calibration parameters to typical values of $\delta = 90°$, $\alpha_0 = 2°$ and $\beta_0 = 20°$. For given incoming polarizations with known S/I and L/I we can compute the Fourier coefficients according to Eq. 3.15 and determine S/I and L/I with modified calibration parameters with Eq. 3.16. Subtracting this result from the given incoming S/I and L/I we can identify the error due to the modified calibration parameters. This procedure is repeated for all possible S/I and L/I. Fig. 3.10 shows the results of this calculation. The errors from the retardance δ and the relative angle $\alpha_0 - \beta_0$ are analyzed separately. In the first case the error in $\alpha_0 - \beta_0$ is set to zero (blue curve) whereas the orange curve shows the case when the error in the retardance is zero. The contribution of the uncertainty in $\alpha_0 - \beta_0$ alone to errors in S/I and L/I (in orange) is typically much smaller than the contribution from the uncertainty in δ alone, shown in blue. The calibration uncertainties for S/I are always below 0.1%, and the calibration uncertainties for L/I are below 0.35% for any analyzed input polarization. For our example measurement of small S/I values the calibration uncertainty is below 0.05% for S/I.

3.6.3 Waveplate Imperfections

Even after input intensity fluctuations were normalized out, there was still a variation in the transmitted light intensity as the waveplate rotated. It was realized that this is related to waveplate imperfections. The initially observed variation for an achromatic waveplate (Thorlabs AQWP05M-980) is shown by the orange points in Fig. 3.11. This variation limited the uncertainty in S/I to about 0.3%. Using instead a monochromatic waveplate (Thorlabs WPQ05M-1064) suppressed this 'ripple', as shown by the blue points in Fig. 3.11.

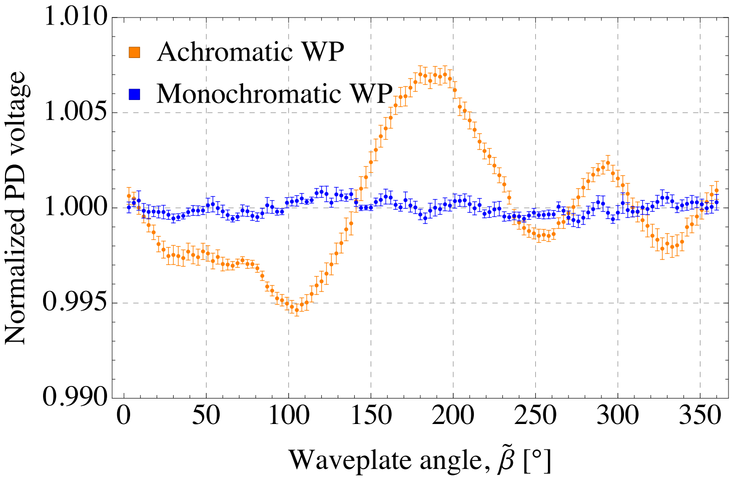

FIGURE 3.11: Investigation of systematic errors related to waveplate imperfections (‘ripple’). An achromatic waveplate (Thorlabs AQWP05M-980) shown in orange makes the detected intensity vary much more as a function of waveplate orientation than does a monochromatic waveplate (Thorlabs WPQ05M-1064) shown in blue. Error bars represent statistical uncertainty.

A similar phenomenon was observed in astrophysical applications of rotating waveplate polarimeters [41, 28]. There, by looking at the wavelength dependence of the systematic error, it was shown that the ripple of the rotating waveplate transmittance is caused by a Fabry-Perot-type interference effect. Later investigations supported this observation [19, 21].

Therefore, the ripple observed here is likely caused by the interference of the multiple layers of the waveplate. Each tested waveplate has its characteristic ripple spectrum. It was also found that this ripple significantly depends on alignment. By taking the Fourier transform of the measurement shown in Fig. 3.11, one can extract the limit on false Fourier components which would contribute to systematic errors in the polarimetry measurement. The remaining variations typically contribute an uncertainty of less than 0.01% in the normalized Fourier coefficients. This translates into an error in S/I of smaller than 0.01%.

3.6.4 Misalignment

The waveplate and the polarizer that make up the polarimeter are ideally aligned so that their optical surfaces are exactly perpendicular to the direction of propagation of the laser beam. Misalignment of the polarimeter from this configuration can introduce systematic errors. Various effects contribute to systematic errors related to misalignment. Therefore, this error source was investigated by intentionally misaligning the polarimeter in the plane parallel to the optical table w.r.t. the incoming laser beam.

Fig. 3.12 shows the measured systematic uncertainty that arises due to misalignment. This data was taken with a fixed elliptical polarization from a waveplate with $S/I \approx 16\%$

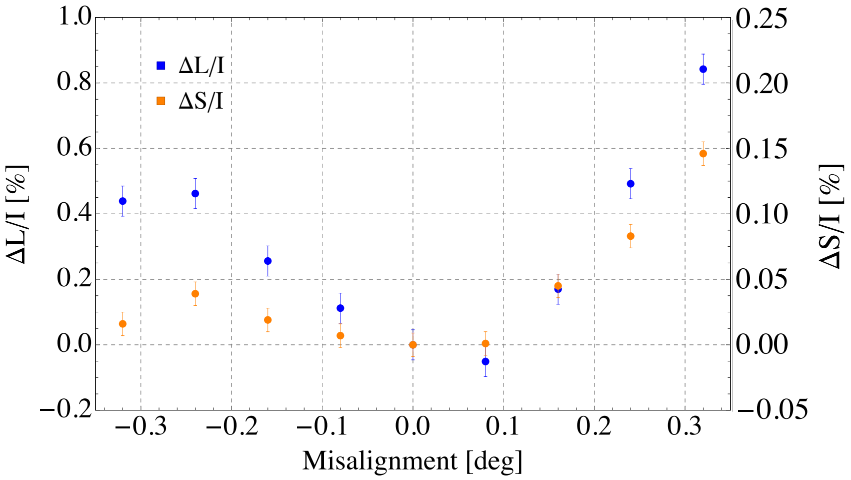

FIGURE 3.12: Systematic uncertainties $\Delta S/I$ in S/I (orange, right scale), and $\Delta L/I$ in L/I (blue, left scale), caused by misalignment of the polarimeter with respect to the light propagation axis. The measurements were performed with a fixed incoming polarization of $S/I \approx 16\%$ and $L/I \approx 98\%$. Error bars represent statistical uncertainty.

and $L/I \approx 98\%$. The polarimeter is mounted on a kinematic device alignment stage (Newport 9081) which makes it possible to misalign the setup by a fixed amount w.r.t. the incoming laser beam. An auxiliary measurement was performed to translate the number of turns of x- and y-screws of the stage into the angular deviation. One turn in the stage screw corresponds to $\sim 0.3°$ angular misalignment. The data in Fig. 3.12 was taken in steps of quarter turns. While aligning the polarimeter by maximizing the intensity transmitted through a pair of apertures, it is possible to detect intensity changes with less than an eights of a turn. Therefore, the polarimeter is routinely aligned to better than $0.05°$ which translates into uncertainties of 0.005% in S/I and 0.05% in L/I.

3.6.5 Finite Extinction Ratios of Polarizers

Two different polarizers can contribute to systematic uncertainty. First, the polarizer used inside the polarimeter and second, the polarizer used for calibration. The two linear polarizers used within and in front of the polarimeter each have a finite extinction ratio, $r = I_{\text{min}}/I_{\text{max}}$. A simple model of a polarizer perfectly transmits light along one axis and suppresses light transmission by a factor of r along the orthogonal axis. The corresponding Mueller matrix for such a polarizer is given in App. A.2. For polarizers used here the extinction ratio is specified to be $r \lesssim 10^{-5}$ rather than being perfectly $r = 0$. As turned out in tests of polarizers, see Sec. 4.3.3 in the next chapter, the extinction ratio was found to be even smaller than the specified value, $r < 10^{-6}$. For the analysis below we remain more conservative and assume the worst case scenario with the specified value of $r \sim 10^{-5}$.

The relative Stokes vector after circular polarized light passed through an imperfect polarizer is

$$\vec{s} = \begin{pmatrix} 1-2r \\ 0 \\ 2\sqrt{r(1-r)} \end{pmatrix} \simeq \begin{pmatrix} 1-2r \\ 0 \\ 2\sqrt{r} \end{pmatrix}, \tag{3.31}$$

Therefore, for an extinction ratio of $r \sim 10^{-5}$, there is a residual S/I of up to $2\sqrt{r} \simeq 0.6\%$. In previous polarimeter considerations, this residual circular polarization was thought to limit the absolute accuracy of the polarimeter [43]. However, this turns out to be not the case. The finite extinction ratio of the polarizer in the polarimeter modifies the Fourier components measured in the outgoing intensity I_{out}. The polarization is measured through Fourier components of this transmitted intensity I_{out} where the extinction ratio enters as r (and not as $\sqrt{r}$) which makes the effect much smaller. In a more detailed consideration, Eq. 3.13 is re-obtained with the transformation of the Stokes parameters $M \to M(1-2r)$, $C \to C(1-2r)$ and $S \to S(1-2r)$. Therefore, the measured Stokes parameters differ from the true values by a factor $1/(1-2r) \simeq 1+2r$, which is 0.002% for $r \simeq 10^{-5}$. Numerically solving Eqs. (3.16) with the residual Stokes parameters, the error on the calibration parameters is found to be less than 0.05° for α and β_0, and smaller than 0.001° for δ.

3.6.6 Summary of Systematic Errors

The summary of systematic errors is presented in Table 3.1. As discussed previously, the contribution of systematic errors is dependent on incoming polarization. For applications on ACME, the light is dominantly linearly polarized. Therefore we focus on polarizations with relative Stokes parameters $S/I < 30\%$ and $L/I > 95\%$.

Since the rotation stages are the core elements of the polarimeter, they were carefully tested to assure their specified accuracy. The polarimeter utilizes the precision rotation stages by Newport (URS50BCC) with a specified uni-directional repeatability of 0.002°, a bi-directional repeatability of 0.003°, and a reversal value (hysteresis) of 0.004°. These

Error source	$(L/I)_{\text{err}}$ [%]	$(S/I)_{\text{err}}$ [%]
$(\alpha_0 - \beta_0)$ calibration to ±0.1°	< 0.03	< 0.005
δ calibration to ±0.1°	< 0.35	< 0.05
Intensity normalization	< 0.1	< 0.02
Alignment of polarimeter	< 0.05	< 0.005
Imperfections of waveplate	< 0.012	< 0.006
Finite extinction ratio	< 0.002	< 0.002
Quadrature sum	< 0.4	< 0.06

Table 3.1: Summary of the systematic errors affecting the polarization measurement of the polarimeter for $S/I < 30\%$ and $L/I > 95\%$.

specifications were confirmed by tests. However, it was found to be important to reverse the direction of the rotation for each full cycle. In each full rotation a small drift of $\sim 0.0015°$ was observed which effectively corresponds to a change in the calibration angle β_0. This drift was observed to cancel after going in the opposite direction. Therefore, for successive polarimetry measurements, it is important to rotate the waveplate back and forth: one full rotation with increasing $\tilde{\beta}$ from 0° to 360° followed by a full rotation with decreasing $\tilde{\beta}$ from 360° to 0°. The accuracy of the rotation stages, including the drift, does not contribute significantly to systematic errors and is therefore not included in Table 3.1.

Systematic errors due to intensity normalization are mainly caused by the uncertainty in the measured gain ratio. They can be determined by propagating the uncertainties similar to the calculations in Sec. 3.6.2. This numerical analysis reveals an error in L/I of up to 0.1% and an error in S/I of up to 0.02% for dominantly linearly polarized light.

From Table 3.1 we conclude that the net uncertainty in S/I is smaller than 0.1%. The leading error is due to the calibration of the retardance of the waveplate. The systematic errors for L/I are significantly larger, up to 0.4%, mainly because of higher sensitivity to the waveplate delay, δ. From Eqs. 3.17 and 3.18, $S \propto \sin^{-1}(\delta)$ and $L \propto \sin^{-2}(\delta/2)$; a small deviation from $\delta = 90°$ is a first order effect in L and is second order for S. The larger uncertainty in L/I is not important for ACME since the measurement of S/I is most relevant.

4 Polarimetry Measurements on ACME

This chapter summarizes the measurement results performed with the polarimeter described in the previous chapter. In the first section the mechanical stress induced birefringence in vacuum windows of the ACME experiment is analyzed. It is demonstrated that the offset in the relative fraction of circular polarized light S/I due to mechanical stress can be reduced to fractions of percent by aligning the incoming polarization with the birefringence axis.

The second section presents a detailed investigation of thermally-induced birefringence in the electric field plates caused by the high intensity of the laser light. A particular focus of the work is a circular polarization gradient across a nominally linearly polarized laser beam which contributed substantially to a mechanism of the leading systematic error in the ACME Generation I measurement, see Sec. 2.4. The direct comparison of Generation I and II field plates proves that the new field plates suppress this effect by more than an order of magnitude. The small and well-characterized uncertainties of the polarimeter make it possible to conclude that on the second-generation ACME apparatus the thermally-induced birefringence is eliminated to 0.2% in S/I, and is therefore not significant enough to contribute to systematic errors in the next-generation measurement.

The last section summarizes polarimetry tests on optical components like waveplates and polarizers used in the ACME experiment. Contrary to the specifications of the company, the sideport of the Glan-Laser polarizer is found to produce linear polarization which is as good as in the transmitted beam. This result is very important for ACME since the two different ports of the Glan-Laser polarizer are used for polarization switching mentioned in Sec. 2.3. The polarization switching could contribute to AC Stark shift phases if the average ellipticity between the two switched polarizations is non-zero [9].

4.1 Mechanical Stress Birefringence

When the state preparation, refinement or readout laser beams pass through the interaction region of the experiment, they are transmitted through vacuum windows and electric field plates. The second-generation windows which are mounted to the vacuum chamber of the experiment, have dimensions of 5.5 x 3.5 x 0.75 inches and are made of Corning 7980 0A fused silica glass[1]. The electric field plates are made of the same glass substrate.

---

[1] The first-generation windows were made of borosilicate BK-7 glass.

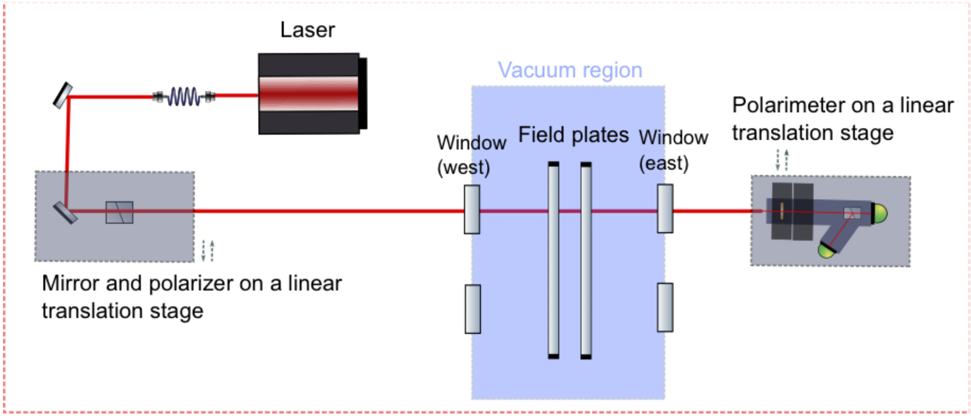

FIGURE 4.1: Experimental setup to measure the total mechanical stress birefringence in windows and electric field plates. After the polarized laser beam passes through the vacuum region of the ACME experiment, its polarization is monitored by the polarimeter. The deviation from the initially linear polarized beam gives information about the total birefringence in the windows and the field plates. The mirror with the polarizer as well as the polarimeter are mounted on linear translation stages to scan across the whole window. Diagram not to scale.

In addition they are coated with an electrically conducting and transparent layer of indium tin oxide to fulfill their purpose of polarizing the molecules (see Ch. 2 for details).

The field plates as well as the windows can both introduce imperfections to laser polarizations. We first consider mechanical stress birefringence caused by the mounts of the windows and estimate the residual birefringence due to material properties of the windows and electric field plates. After that, the birefringence changes due to differential pressure on vacuum windows are discussed. The setup to measure these effects is shown in Fig. 4.1. We start with a low-power ~ 10 mW laser beam with a wavelength of 703 nm which is sent into the Glan-Laser polarizer after being reflected by mirrors. The last mirror and the polarizer are mounted together on a linear translation stage to scan across the whole optically accessible horizontal window range of ~ 40 mm. The polarizer is placed on a rotational mount to orient its transmission axis w.r.t. the optical table. After being polarized, the laser beam passes through the vacuum region and is measured by the polarimeter. Like the mirror with a polarizer, the polarimeter is mounted on a linear translation stage to enable a scan across the whole optically accessible horizontal window range.

4.1.1 Determination of the Birefringence Axis

The impact of birefringence on outgoing polarization depends on the orientation of incident linear polarization of light passing through the birefringent material. If this orientation angle is perfectly aligned with the birefringence axis, the polarization will remain unchanged. Therefore, to determine the maximum effect of the birefringence of the combined system of windows and field plates, we need to determine the total birefringence axis first. It can be shown that a network of linear birefringent materials is described by a single retarder followed by a polarization rotator [47, 102]. Hence, we can describe the birefrigent network of windows and field plates by the Mueller matrices $\hat{\Gamma}(\delta, \beta)$ and $\hat{R}(\alpha)$ which represent the retarder with a retardance δ and the birefringence axis oriented at an angle β, and the rotator of an angle α, respectively. Their excplicit form is given in App. A.2. With an incoming Stokes vector $\vec{S}_{\text{in}} = (1, \cos 2\gamma, \sin 2\gamma, 0)$ for linear polarized light from a polarizer oriented at an angle γ passing through a network of birefringent materials, the outgoing Stokes vector $\vec{S}_{\text{out}}$ is given by:

$$\vec{S}_{\text{out}} = \hat{R}(\alpha) \cdot \hat{\Gamma}(\delta, \beta) \cdot \vec{S}_{\text{in}} = \begin{pmatrix} 1 \\ \cos(2\theta)\cos(2\beta - 2\gamma) + \cos(\delta)\sin(2\theta)\sin(2\beta - 2\gamma) \\ \sin(2\theta)\cos(2\beta - 2\gamma) - \cos(\delta)\cos(2\theta)\sin(2\beta - 2\gamma) \\ \sin(2\beta - 2\gamma)\sin(\delta) \end{pmatrix}, \tag{4.1}$$

where we defined $\theta = \alpha + \beta$. The orientation angle γ of incoming linear polarization is controlled by the rotation mount of the polarizer and set to be around 0° when the polarizer transmission axis is approximately (±5°) aligned with the optical table.

If we consider only the relative fraction of circular polarized light S/I, then the absolute rotation of the linearly polarized fraction is irrelevant. According to Eq. 4.1 we expect the circular polarized fraction of light to vary as a function of the polarizer transmisson angle γ as following:

$$S/I = \sin\delta \sin(2\beta - 2\gamma). \tag{4.2}$$

To perform the measurement of the birefringence axis angle β, the polarizer needs to be rotated (corresponding to the variation of γ) while the relative fraction of circular polarization S/I is recorded by the polarimeter. The results are shown in Fig. 4.2. To account for possible systematic errors an offset parameter o in the fit function is added to the ideal case of Eq. 4.2:

$$(S/I)_{\text{fit}} = \sin\delta \sin(2\beta - 2\gamma) + o. \tag{4.3}$$

From the fit to the data for S/I in Fig. 4.2 we find $2\beta = 0.39(5)°$ and $\delta = 0.1284(2)$. The offset parameter is $o = (-0.061 \pm 0.015)\%$ which is on the level of the estimated systematic uncertainty discussed in the previous chapter. The fact that $\beta \approx 0°$ means that the birefringence axis is approximately aligned with the optical table.

The values for δ and β from the fit of S/I are used to fit the data for M/I and C/I where the remaining free parameter is α. From the fit of M/I this parameter is determined to be $\alpha = -4.68(4)°$ and agrees with the result from the C/I fit of $\alpha = -4.64(5)°$. Recall that this angle describes the rotation of linear polarization. However, since the reference

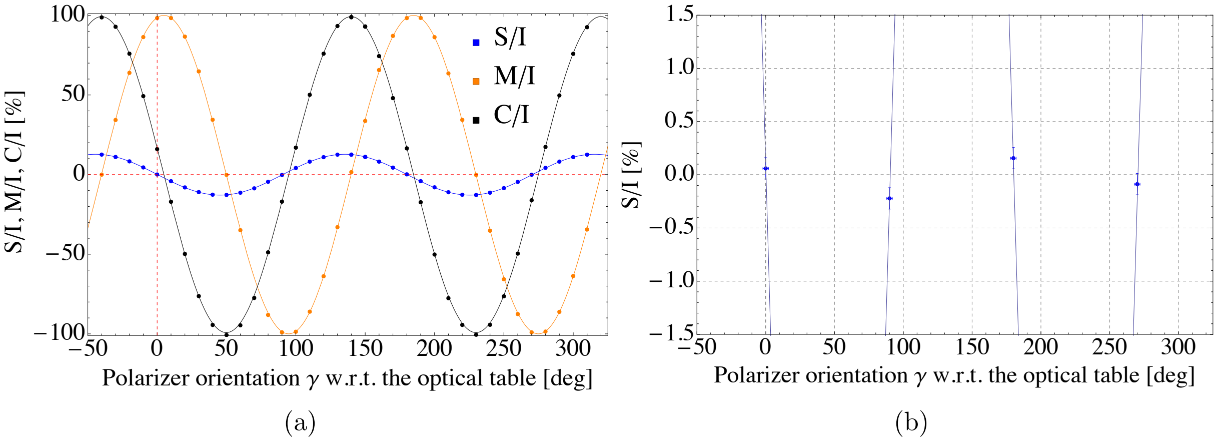

FIGURE 4.2: Determination of the birefringence axis of the combined system of windows and field plates. (a) The relative Stokes parameters S/I, M/I and C/I as a function of the angle γ between the optical table and the polarizer transmission axis. The data for S/I is fitted with a function from 4.3. The data for M/I and C/I is fitted according to Eq. 4.1 with fit parameters δ and β fixed to those from the fit of S/I. (b) Zoom into (a): the four data points where the S/I is minimal together with the fit from (a) are shown. This plot demonstrates that the offset in S/I can be eliminated to fractions of percent by aligning the polarization with the birefringence axis which is found to be approximately aligned with the optical table.

plane for the polarimeter is defined by the calibration polarizer which is aligned with the optical table by eye to ±5°, a non-zero value of α could also correspond to slightly different orientations of the calibration polarizer and the polarizer from Fig. 4.1 used for this measurement. Note also that the polarimeter is placed on a different optical table than the one in front of the vacuum region, which could also be misaligned by few degrees w.r.t. each other. The only way to put a precise limit on the linear rotation angle α would be to use the polarizer in front of the vacuum region as a calibration polarizer, with the polarimeter being on the other optical table. This would require to dismount the windows and the field plates for calibration and mount them back in for the above measurement of δ, β and α. But as mentioned in Chapter 2, the global polarization rotation as well as the relative angle between the state preparation and readout laser beams do not affect the electron EDM signal, assuming they are uncorrelated with other parameters of the experiment. Therefore, in principle, the precise determination of α is not important.

However, it is discussed that the ACME Generation II setup could use additional rotation stages with half- and quarter-waveplates on both state preparation/refinement and read-out laser beams for fine polarization control [65]. These waveplates would have the purpose to manipulate the polarizations after the laser beams are polarized but before they enter the vacuum region. In this case the linear rotation angle α could play a role and would need to be considered more carefully.

In Fig. 4.2 (b) the four data points for S/I are shown, where the orientation of the polarizer is such that its transmission axis is aligned with the birefringence axis. Note that the relative fraction of circularly polarized light S/I is minimized every 90°. For these orientations of the polarizer transmission axis, S/I can be reduced to fractions of percent as is demonstrated in this figure.

4.1.2 Mechanical Stress Birefringence due to Vacuum Window Mounts

From the results of the total birefringence axis measurement in the previous subsection, we know that an orientation of the polarizer around 45° w.r.t. the optical table maximizes the birefringence effect. Hence, for the following measurements this orientation of the polarizer transmission axis is chosen.

The mechanical birefringence in the state preparation region is characterized in detail. The results are shown in Fig. 4.3. To distinguish contributions of the two windows and the field plates, measurements were performed in gradual steps. First, the relative circular polarization S/I was measured across the whole optically accessible window region of ~ 40 mm with windows on both sides of the vacuum chamber as well as the two field plates inside the chamber. The results depicted with blue data points in Fig. 4.3 (a) show that the relative fraction of circular polarized light is $\sim 14\%$ varying by $\sim 1\%$ across the whole window. However, note that between two neighboring data points in the center region of the window, S/I does not vary significantly above a fraction of percent. The values are separated spatially by 2.5 mm, which is about the width of the laser beam.

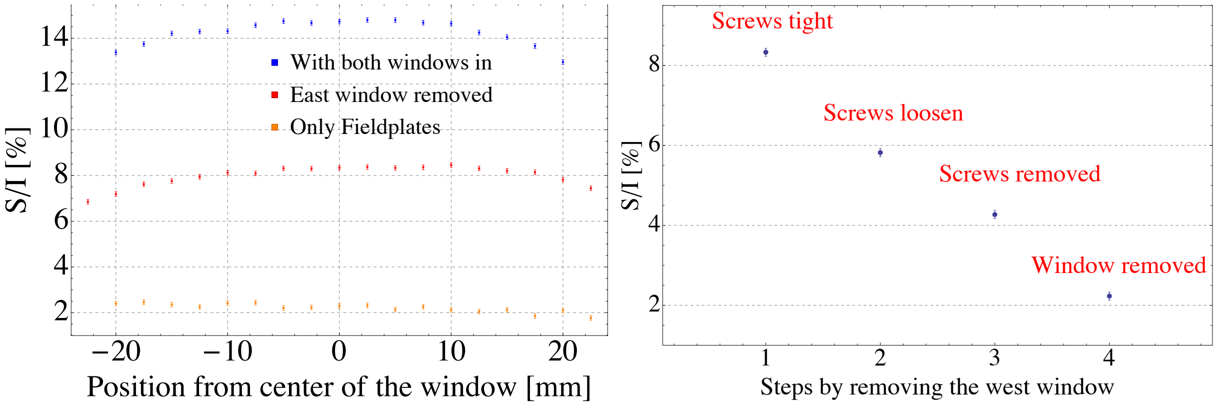

(a) (b)

FIGURE 4.3: (a) Measured total birefringence in the state preparation region across the whole horizontal optically accessible window region. Blue data points show the first measurement set where both windows are in. Afterwards the east window was removed, see red data points. Finally, shown in orange, after the second window is removed, only the contribution of field plates remains. (b) Gradual steps of removing the second window with corresponding polarimetry measurements. Measurements were performed in the window center. The first step ('screws tight') corresponds to the red data point in the center of figure (a), whereas the last step ('window removed') agrees with the center orange point in figure (a).

Later polarimetry tests on the ACME experiment (see Fig. 4.10 in the following section) confirmed that within the horizontal laser beam width, there are no gradients of S/I above 0.1%.

Afterwards the window facing the outgoing laser beam from the vacuum region ('east window') was removed and the scan of S/I was repeated, see red data points in Fig. 4.3 (a). The mean value of S/I across the window dropped from $\sim$ 14% to $\sim$ 8% by removing one window. Similar to the setup with both windows in, the value of S/I varied by $\sim$ 1% from the center to the edges of the window. As previously, the value of S/I did not change significantly within the width of the laser beam which is approximately equal to the distance between two neighboring data points. Since the ThO molecules travel between field plates, with the east window being removed the polarimeter measures most closely the polarization which is 'seen' by the molecules. As later measurements show, the field plate on the east side distorts the polarization from the region in between the field plates not above $\sim$ 2%. Therefore, one can expect that the laser light which prepares or refines the required state in the ThO molecules, has a circular polarization of $\sim 6-8\%$ if the linear polarized light is diagonally or anti-diagonally oriented w.r.t. the optical table. However, as demonstrated in the previous section, recall Fig. 4.2 (b), by aligning the linear polarization with the birefringence axis, the S/I can be reduced to fractions of percent.

In the final step the west window was removed gradually. Each step a polarimetry measurement was recorded in the center of the window. Fig. 4.3 (b) shows the results. In the first step the screws are tight and the window is in place. This measurement agrees with Fig. 4.3 (a), red data points in the center of the window. In the second step the screws are loosen such that they are still holding the window. Doing so, the value of S/I dropped by $\sim$ 2%. Further decrease in S/I is observed by about the same amount when the screws are removed. During this polarimetry measurement the window was held in place by hands. Finally the window was removed and the residual S/I of $\sim$ 2% coming from the field plates was observed.

4.1.3 Residual Birefringence due to Material Properties

According to the specifications of Corning 7980 fused silica glass from which the second-generation field plates and the windows are made, the residual birefringence is $\Delta n \leq 1\,\mathrm{nm/cm}$ [24]. With a field plate thickness of $t = 12.7$ mm and a wavelength of $\lambda = 703$ nm, we obtain a maximum retardance of

$$\delta = 2\pi\, t\, \Delta n/\lambda \simeq 1.17 \cdot 10^{-2}. \tag{4.4}$$

Recalling Eq. 4.2, with a birefringence axis being oriented at $\beta = 45°$ w.r.t. the incoming linear polarization, and for $\delta \ll 1$, this retardance causes a relative fraction of circular polarized light of approximately the same amount:

$$S/I = \sin\delta \simeq \delta \simeq 1.2\%. \tag{4.5}$$

Having two field plates and therefore twice the thickness, leads to an S/I of up to 2.4% which is above the measured value of 2.2% and therefore within the specifications. Since the windows have a similar thickness of $t = 1.9$ cm, the estimate of residual birefringence also agrees with the measurement from step 3 to 4 in Fig. 4.3 (b) where the window without the screws was removed and a change of $\sim 2\%$ in S/I was observed.

4.1.4 Effect of Differential Pressure Across the Window

Pumping out the chamber puts a differential pressure of one atmosphere across the windows. Therefore, the mechanical stress changes and the resulting birefringence is modified. We can make an order-of-magnitude estimate by assuming the stress of $\sigma = 1\,\text{atm}$ and relating it to the resulting birefringence. The stress-optics law [57, 26] states that the difference in principal stresses results in a change of the refractive index Δn as:

$$\Delta n = K(\sigma_{xx} - \sigma_{yy}), \tag{4.6}$$

where K is the stress-optical coefficient, and σ_{xx}, σ_{yy} are the corresponding principal stresses in the x or y direction, respectively. For Corning 7980 glass, $K = 3.5 \cdot 10^{-3}\,\text{GPa}^{-1}$ [24]. Assuming $\sigma_{xx} - \sigma_{yy} \simeq 1\,\text{atm}$, the refractive index changes by $\Delta n \simeq 3.5 \cdot 10^{-7}$ which leads to a change in the retardance of

$$\Delta\delta = \Delta n \cdot 2\pi t/\lambda \simeq 5.9 \cdot 10^{-2}, \tag{4.7}$$

where $t = 1.9\,\text{cm}$ is the thickness of the window and $\lambda = 703\,\text{nm}$ the used wavelength of light. According to Eq. 4.5 this change in retardance corresponds to $\Delta S/I \simeq 6\%$.

The experimental results reveal an effect on the estimated scale, though lower than expected. During the pump down, the polarimeter measured continuously at one position of the window, as shown in Fig. 4.4 (a). When the pump is switched on, the value of S/I drops by $\sim 2\%$. After that, a mechanical relaxation is observed, where the S/I increases by $\sim 0.5\%$ on a scale of around 15 minutes. A day after the pump down a polarimetry scan across the whole window was taken and compared to the measurement before the pump down, see Fig. 4.4 (b). The differential pressure changed the value of S/I by $1-3\%$ and the distribution of S/I across the window is comparable to the one in Fig. 4.3 (a). Note that the windows were removed and mounted back in between those data sets. Since small changes in tightening strength of the window screws affect the S/I on the order of 2%, it is in correspondence with the change of S/I by few percent between Figs. 4.3 and 4.4.

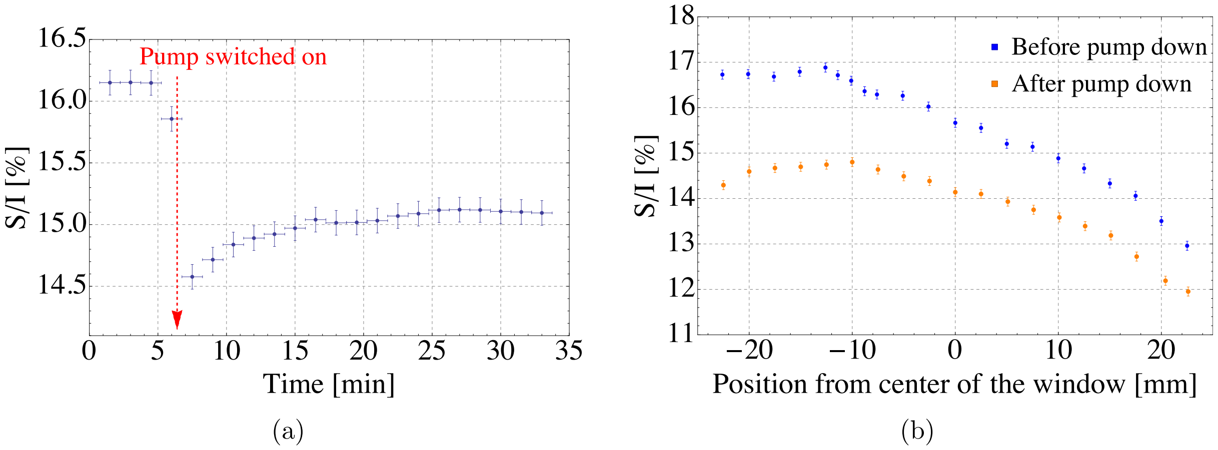

FIGURE 4.4: (a) Stress-induced ellipticity change during the pump down. Around 6 minutes after the polarimetry measurements started, the pump is switched on. This results in a differential pressure across the windows of around one atmosphere within seconds. A mechanical relaxation after the pump down on a scale of ~ 15 min. is observed. (b) Change of S/I across the whole state preparation region after pumping out the vacuum chamber. Blue data points show the measurement set before the pump down, whereas orange data points were taken on the next day after the pump down.

4.2 Thermally-induced Birefringence in the Electric Field Plates

In addition to purely mechanical stress birefringence due to mounts or differential pressure, the polarization imperfection in the laser beams may be caused thermally. For example, this effect was observed in UHV vacuum windows [87], laser output windows [29], and Nd:YAG rods [55]. In the ACME Generation I measurement, thermally-induced birefringence contributed to a systematic error mechanism that dominated the systematic uncertainty [8]. The high power laser beams were intense enough to create thermal gradients in glass electric field plates coated with a conducting layer of indium tin oxide. The absorbed heat leads to mechanical stress which, as we have seen in the previous section, causes birefringence. For the second-generation ACME setup new field plates were designed which should suppress this effect. This section discusses a detailed investigation of these second-generation field plates. After summarizing a theoretical model for thermally-induced birefringence and estimating the size of the effect, a direct experimental comparison of first- and second-generation plates on a separated setup is presented. Finally, a test on the ACME Generation II setup demonstrates that thermally-induced birefringence is not a concern for the next-generation electron EDM measurement.

4.2.1 Theoretical Model and Estimates

First, let us introduce a model for thermally-induced birefringence. The discussion presented here uses results of [48, 43] and goes beyond it by considering the thermally-induced offset in S/I, relating the gradient and offset coefficients to each other, and making an estimate of both coefficients for the first- and second-generation field plates. As we shall see in the next subsection where the experimental results are presented, the offset in S/I turns out to be a more accurate tool for the characterization of thermally-induced birefringence because it is more sensitive to thermal effects.

The thermally-induced stress in a material is related to the deposited position-dependent heat per unit volume, $Q(\vec{r})$, via the following equation [7]:

$$\nabla^4\phi = \frac{E\beta}{\kappa}Q(\vec{r}). \tag{4.8}$$

Here, we introduced the Airy stress ϕ and the following three material properties: E – the Young's modulus, β – the coefficient of thermal expansion, and κ – the thermal conductivity of the material. The Airy stress is related to the usual principal stresses in the x or y directions and the shear stress σ_{xy} via

$$\frac{\partial^2\phi}{\partial x^2} = \sigma_{yy}, \quad \frac{\partial^2\phi}{\partial y^2} = \sigma_{xx}, \quad \frac{\partial^2\phi}{\partial x\partial y} = \sigma_{xy}. \tag{4.9}$$

For thermal stresses the shear terms σ_{xy} vanish [7].

Assuming a small fraction of absorbed light intensity, the absorbed heat per unit volume $Q(x, y)$ can be expressed through the incoming intensity of the laser light $I(x, y)$ and the absorbance α as:

$$Q(x, y) = \alpha\, I(x, y). \tag{4.10}$$

Given the wavelength λ, the absorbance α can be calculated from the imaginary part of the refractive index, also called extinction coefficient $\mu = \mathrm{Im}\, n$ [10]:

$$\alpha = 4\pi\mu/\lambda. \tag{4.11}$$

The transmitted intensity of light is given by $I(z) = I_0\,\mathrm{Exp}[-\alpha\, z]$ which is the Beer-Lambert law [101]. For $\alpha\, z \ll 1$ we obtain $I(z) \simeq I_0(1 - \alpha\, z)$, and the absorbed intensity per unit length is therefore $\alpha\, I_0$ in agreement with Eq. 4.10.

We already discussed how to obtain the change in S/I from the mechanical stress in the previous section. As previously, we consider the case where the birefringence in maximal, i.e. where the birefringence axis is oriented at 45° w.r.t. the incoming linear polarization transmission axis. Recalling Eqs. 4.6 and 4.7, the relative Stokes parameter is related to the principal stresses as:

$$S_I \equiv S/I = \frac{2\pi t}{\lambda} K(\sigma_{xx} - \sigma_{yy}), \tag{4.12}$$

where K is the stress-optical coefficient, λ the wavelength of incident light and t the thickness of the material. It should be remarked that the same intensity I enters Eq. 4.10 for the absorbed heat as is used to normalize the Stokes parameter in Eq. 4.12. But the latter is not affected by the derivatives on the left side of Eq. 4.8 where we relate the stress to the relative Stokes parameter. Eq. 4.8 describes the impact of intensity for the absorbed heat which has already been included on the right side of this equation. Therefore, for clarity, we define the symbol for the relative Stokes parameter representing the circular polarization as

$$S_I \equiv S/I. \tag{4.13}$$

To find the solution to Eq. 4.8, we need to know the distribution of the intensity which for a Gaussian beam is given by

$$I(x, y) = I_0\, \mathrm{e}^{-2x^2/w_x^2 - 2y^2/w_y^2}, \tag{4.14}$$

where w_x and w_y are the beam waists in the x and y directions, and I_0 the peak intensity which is related to the total power of the laser beam,

$$P_{\text{tot}} = \int_{-\infty}^{\infty}\int_{-\infty}^{\infty} I(x, y)\mathrm{d}x\mathrm{d}y = \frac{\pi}{2} I_0 w_x w_y. \tag{4.15}$$

Let us assume that we have a stretched beam $w_y \gg w_x$, and can approximate $I(x, y) \simeq I(x)$ around the center of the beam, $y \simeq 0$. Then the intensity can be written as:

$$I(x) = \frac{2P_{\text{tot}}}{\pi w_x w_y}\, \mathrm{e}^{-2x^2/w_x^2}. \tag{4.16}$$

Due to the assumption of a stretched beam, we can make the approximation that the stresses change only along x and hence, $\partial^2\sigma_{xx}/\partial y^2 \simeq 0$. Combining this result with Eqs. 4.10-4.12 and 4.16, Eq. 4.8 simplifies to:

$$\frac{\partial^2}{\partial x^2} S_I(x) = \frac{4\,g}{\sqrt{2\pi} w_x}\, \mathrm{e}^{-2x^2/w_x^2}, \tag{4.17}$$

with g being a constant which we call ‘gradient coefficient’ dependent on the material as well as properties of the laser beam:

$$g = 4\pi\sqrt{2\pi}\frac{P_{\text{tot}}}{\lambda^2 w_y}\frac{KE\beta\mu}{\kappa}\, t. \tag{4.18}$$

Due to the symmetric intensity distribution, the boundary conditions are $S_I(0) = \text{const} \equiv$

o and $\partial S_I(0)/\partial x = 0$. After integrating Eq. 4.17 we find the analytical solution:

$$S_I(x) = g\left(w_x\left(1 - \mathrm{e}^{-2x^2/w_x^2}\right) - \sqrt{2\pi}x\mathrm{Erf}(\sqrt{2}x/w_x)\right) + o. \tag{4.19}$$

Note that the gradient of $S_I(x)$ is given by:

$$\frac{\partial}{\partial x}S_I(x) = g\,\mathrm{Erf}(\sqrt{2}x/w_x). \tag{4.20}$$

When the intensity of the laser beam has dropped to 13.5%, at $x = w_x$, the gradient value is already close to its maximum since $\mathrm{Erf}(\sqrt{2}) \simeq 0.95$:

$$\frac{\partial}{\partial x}S_I(x)|_{x=w_x} \simeq \frac{\partial}{\partial x}S_I(x)|_{\max} \simeq g. \tag{4.21}$$

We remark that the solution in Eq. 4.19 becomes unphysical for large x: $S_I \to \pm\infty$ for $x \to \pm\infty$ where obviously $S_I(\pm\infty) = 0$ should be true. The reason is the following: In the derivation we assumed the intensity $I(x,y)$ to be independent of y and therefore neglected the change of stresses in the y direction which is not a good assumption for large x. Therefore, we cannot derive an analytical expression for the thermally-induced offset o from the case of a stretched beam. We shall rather examine the solution for a circular Gaussian beam with $w_x = w_y = w$, $I_{\mathrm{circ.}}(r) = I_0\,\mathrm{e}^{-2r^2/w^2}$. By transforming the biharmonic operator on the right side of Eq. 4.8 into cylindrical coordinates, one can find the solution which fulfills the boundary conditions $S_I(\pm\infty) = 0$ and $\partial S_I(0)/\partial x = 0$ [48]:

$$S_{I\,\mathrm{circ.}}(x) = o\,\frac{w^2\left(1 - e^{-2x^2/w^2}\right)}{2x^2}, \tag{4.22}$$

with

$$o = 2\pi\frac{P_{\mathrm{tot}}}{\lambda^2}\frac{KE\beta\mu}{\kappa}\,t. \tag{4.23}$$

Note that $S_{I\,\mathrm{circ.}}(0) = o$ according to L'Hôpital's rule. Far from the center of the beam, the elongated shape of the beam can be approximated to be circular. Therefore, the offset parameter o derived from the case of a circular beam can be used as an estimate for the offset in the case of a stretched beam; comparing Eq. 4.18 with Eq. 4.23 yields:

$$\frac{o}{g} \approx \frac{w_y}{5}. \tag{4.24}$$

The dependence on the vertical width of the beam w_y in the gradient coefficient g can be viewed as a reduction of the effective power in the horizontal direction, whereas in the case of a circular beam the power in both dimensions is included. Both, the gradient and offset coefficients, have the same dependence on material properties as well as the total power and wavelength of light. As we shall see, the most relevant and changeable quantities are the thickness of the material t, its thermal expansion coefficient β, and the total light power P_{tot}. Thus we can summarize the dependence of thermally-induced birefringence as following:

$$(S/I)_{\text{Thermal}} \propto t \cdot \beta \cdot P_{\text{tot}}. \tag{4.25}$$

To minimize the effect of thermally-induced birefringence, we shall look for a material with a low thermal-expansion coefficient β, reduce the thickness t, and minimize the needed total laser power P_{tot}.

Let us now consider two materials superimposed on each other, e.g. glass coated with some other transparent material, where both materials contribute to thermally-induced birefringence due to the incident laser beam. In the first material the retardance δ_1 is induced whereas in second it is δ_2. Since for thermally-induced stresses the birefringence axis β is solely determined by the geometry of the beam, this axis is equal for both materials, $\beta_1 = \beta_2$. Therefore, the two materials can be viewed as a single retarder with a total retardance of $\delta = \delta_1 + \delta_2$. In this case, as becomes evident from Eq. 4.5, for small retardances $\delta_1 \ll 1$ and $\delta_2 \ll 1$, their impact on S/I is simply given by their sum:

$$S_I \simeq \delta_1 + \delta_2. \tag{4.26}$$

Recalling the thermal cause for this birefringence, S_I is then given by Eq. 4.19 with the gradient coefficient

$$g = 4\pi\sqrt{2\pi}\frac{P_{tot}}{\lambda^2 w_y}\left(\frac{K_1 E_1 \beta_1 \mu_1}{\kappa_1}\,t_1 + \frac{K_2 E_2 \beta_2 \mu_2}{\kappa_2}\,t_2\right), \tag{4.27}$$

and an analogous expression for the offset coefficient o:

$$o = 2\pi\frac{P_{tot}}{\lambda^2}\left(\frac{K_1 E_1 \beta_1 \mu_1}{\kappa_1}\,t_1 + \frac{K_2 E_2 \beta_2 \mu_2}{\kappa_2}\,t_2\right). \tag{4.28}$$

The subscript ‘1’ denotes the properties of the first material (i.e. the glass) and the subscript ‘2’ of the second (i.e. the coating).

Let us now examine the thermally-induced birefringence in a glass plate coated with indium-tin-oxide (ITO) quantitatively. Table 4.1 lists an overview over the material properties which enter Eqs. 4.27 and 4.28 for three types of glasses as well as the ITO coating.

For glasses, the stress-optical coefficient K, the Young's modulus E, the extinction coefficient μ and the thermal conductivity κ are all comparable to each other within a factor of 1 to 1.5. The decisive property is the thermal expansion coefficient β which is about an order of magnitude lower for fused silica as opposed to borosilicate glass. Fused silica is the better material for the suppression of thermally-induced birefringence, and was therefore chosen for the second-generation field plates.

For the inevitable ITO coating needed to make the field plates electrically conduc-

Material property	Glass			Coating
	Borosilicate (Borofloat)	Borosilicate (N-BK7)	Fused silica (Corning 7980)	Indium-tin-oxide (ITO)
Stress-optical coeff. K [10^{-3} GPa^{-1}]	4.0 [82]	2.77 [25]	3.5 [24]	~ 1
Young's modulus E [GPa]	64 [82]	82 [25]	73 [24]	116 [63]
Thermal exp. coeff. β [10^{-6}/K]	3.25 [82]	7.1 [25]	0.52 [24]	8.5 [32]
Extinction coeff. $\mu = \operatorname{Im} n$	10^{-7} [51]	10^{-7} [51]	10^{-7} [51]	$\sim 10^{-2}$ [31, 74]
Thermal conductivity κ [W / (m K)]	1.2 [82]	1.11 [25]	1.38 [24]	5.86 [4, 100]
Product $KE\beta\mu/\kappa$ [fm / W]	69	145	9	$\sim 10^7$

TABLE 4.1: Material properties relevant for thermally-induced birefringence according to Eqs. 4.27 and 4.28 where the product $KE\beta\mu/\kappa$ determines the decisive material factor. Three types of glasses as well as the indium-tin-oxide (ITO) coating for electric field plates are compared. Comparing the product of material properties, the choice of fused silica glass suppresses the thermally-induced birefringence whereas the high impact of ITO demands to make the coating as thin as possible.

tive, the product of material properties contributing to thermally-induced birefringence, $KE\beta\mu/\kappa$, is several orders of magnitude larger than for glass. The value for the stress-optical coefficient of indium-tin-oxide is not found in the literature but can be assumed to be on the same order of magnitude as for other transparent materials. Comparing more than 50 different materials, the stress-optical coefficient is always around $10^{-3}\,\mathrm{GPa}^{-1}$ [97, 103, 64]. The most important property of ITO responsible for the high impact on thermally-induced birefringence is the extinction coefficient which is around 100,000 times larger compared to glass. It is therefore important to make the coating as thin as possible.

The specific estimates of gradient and offset coefficients for the first- and second-generation field plates are presented in Table 4.2. Furthermore, the lenses for the beam expansion are included, since, as we shall see, they are found to contribute to thermally-induced birefringence. Apart from the material properties discussed above, the total power of the laser beam P_{tot}, the wavelength of light λ, and the thicknesses of the glass and the coating, t_1 and t_2, enter Eqs. 4.27 and 4.28. In addition, the vertical width of the beam, w_y, is needed to determine the gradient coefficient which is set to $w_y \simeq 30\,\mathrm{mm}$ according to the experimental setup. The wavelength of light is set to $\lambda = 1090\,\mathrm{nm}$ while both the offset and gradient coefficients are calculated per total power. For both generations the field plates have the same thickness of 0.5" = 12.7 mm. The first-generation field plates are made of borosilicate 'Borofloat' glass whereas for the second generation the better

System	**Gen. I plate**	**Gen. II plate**	**Lenses**
Glass type	Borosilicate (Borofloat)	Fused Silica (Corning 7980)	Borosilicate (N-BK7)
Glass thickness t_1 [mm]	12.7	12.7	$\sim$ 10 (aver.)
ITO coating thickness t_2 [nm]	200	20	0 (no ITO)
Gradient coeff. per total power g/P_{tot} [%/(mm $\cdot$ W)], for $w_y = 30\,\text{mm}$, see Eq. 4.27	0.25	0.03	0.13
Offset coeff. per total power o/P_{tot} [%/W], see Eq. 4.28	1.52	0.17	0.77

Table 4.2: Estimates of thermally-induced birefringence coefficients per total power based on the theoretical model described in Sec. 4.2.1. Three systems are compared: the generation I and II electric field plates coated with indium-tin-oxide (ITO), and the lenses used for the beam expansion. The relevant material constants are summarized in Table 4.1. Using those, the gradient and offset coefficients per total laser beam power are calculated for the wavelength of $\lambda = 1090\,\text{nm}$ according to Eqs. 4.27 and 4.28.

glass was used, 'Corning 7980 0A' fused silica. Furthermore, the second-generation field plates feature a ten times thinner coating, 20 nm instead of 200 nm. This makes them to be around an order of magnitude better in terms of their contribution to thermally-induced birefringence. For both generations the relative contribution of the ITO coating to the total gradient and offset coefficients is approximately around $60 - 70\%$.

As described in Chapter 2, the beam needs to be expanded in the vertical direction to reach all the molecules passing through the interaction region. The large vertical width of $w_y \simeq 30\,\text{mm}$ requires to polarize the beam before it passes through the lenses. Therefore, the lenses may also introduce polarization imperfections, in particular through thermally-induced birefringence. Easily available lenses are made of N-BK7 borosilicate glass. The averaged thickness of the lenses is estimated to be $\sim$ 10 mm. However, it is not clear how the varying thickness of the material will influence the thermal effects described by the theoretical model in this section. Also note that the beam is circular when it enters the first lens, and elongated when it passes the second lens. This could change the gradient and offset coefficients in S/I in an unexpected way. Nevertheless, we can make a rough estimate with the average thickness. According to this estimate, presented in the last column of Table 4.2, the lenses could significantly contribute to the thermally-induced birefringence.

Finally, we remark that the estimate of offset coefficients in Table 4.2 is around six times larger than that of gradient coefficients, see Eq. 4.24. Therefore, we expect the offset in S/I to be a more sensitive probe for thermally-induced birefringence. However, recall that it is the ellipticity gradient which substantially contributes to the systematic error mechanism in the ACME experiment.

4.2.2 Separate Measurements on First- and Second-generation Field Plates

The thermally-induced birefringence in the first- and second-generation field plates was directly compared on a separated setup, see Fig. 4.5. We start with a collimated high-power laser beam with the total power of up to 6 W, wavelength 1090 nm, and a circular Gaussian beam shape with waists of $w_x \simeq w_y \simeq 1.4\,\mathrm{mm}$. The laser beam is first polarized with the Glan-Laser polarizer, with its transmission axis being oriented at 45° w.r.t. the x axis (which is the birefringence axis) to maximize the birefringence effect. Then the beam is expanded in the y direction using two cylindrical lenses with focal lengths of $f = 10$ mm (LJ1878L2-C) and $f = 200$ mm (LJ1309L1-C), so that the beam shape is elongated with $w_x = 1.4\,\mathrm{mm} \ll w_y \simeq 30\,\mathrm{mm}$. The laser beam then passes through the glass plate and enters the polarimeter. S/I is measured as the polarimeter is translated on a linear translation stage in the x direction across the narrow illuminated area on the field plate.

The measurement results are shown in Fig. 4.6. The intensity profile of the laser beam in the x direction is the gray curve. The spatial variation of S/I for the first-generation plate are the blue points, the data from the second-generation plate is shown in orange. From both data sets the contribution of lenses was substracted (red data points) which was measured separately by removing the field plate. The smooth curves represent the fits to the data with a function from Eq. 4.19. The left figures (a), (c) and (e) show the absolute value of S/I, whereas on the right side, figures (b), (d) and (f), an offset to the corresponding left figures is substracted to visualize and compare the gradients. Both, the offset and gradient in S/I, are clearly magnified with increasing power. For the

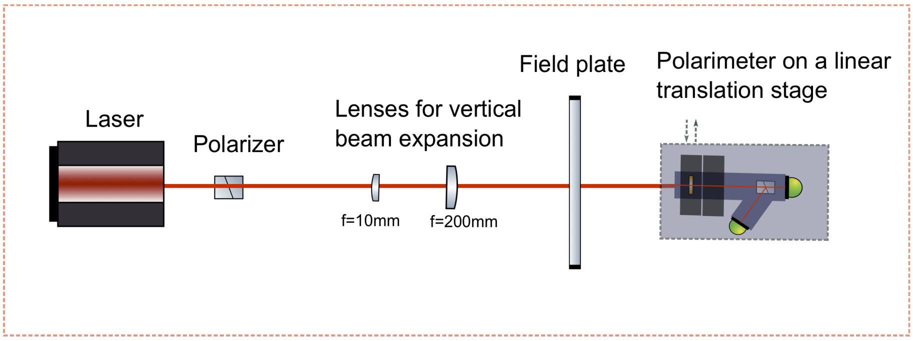

FIGURE 4.5: Experimental setup to measure the thermally-induced birefringence in electric field plates. After being polarized, the laser beam passes through the telescope (a set of two lenses) which expands the beam in the vertical direction to reproduce the elongated beam shape used in the ACME experiment. The polarimeter is placed directly after the field plate on a linear rotation stage to scan across the beam profile and thereby to record polarization gradients and offsets. For a separate measurement of thermally-induced birefringence in the lenses, the field plate is removed.

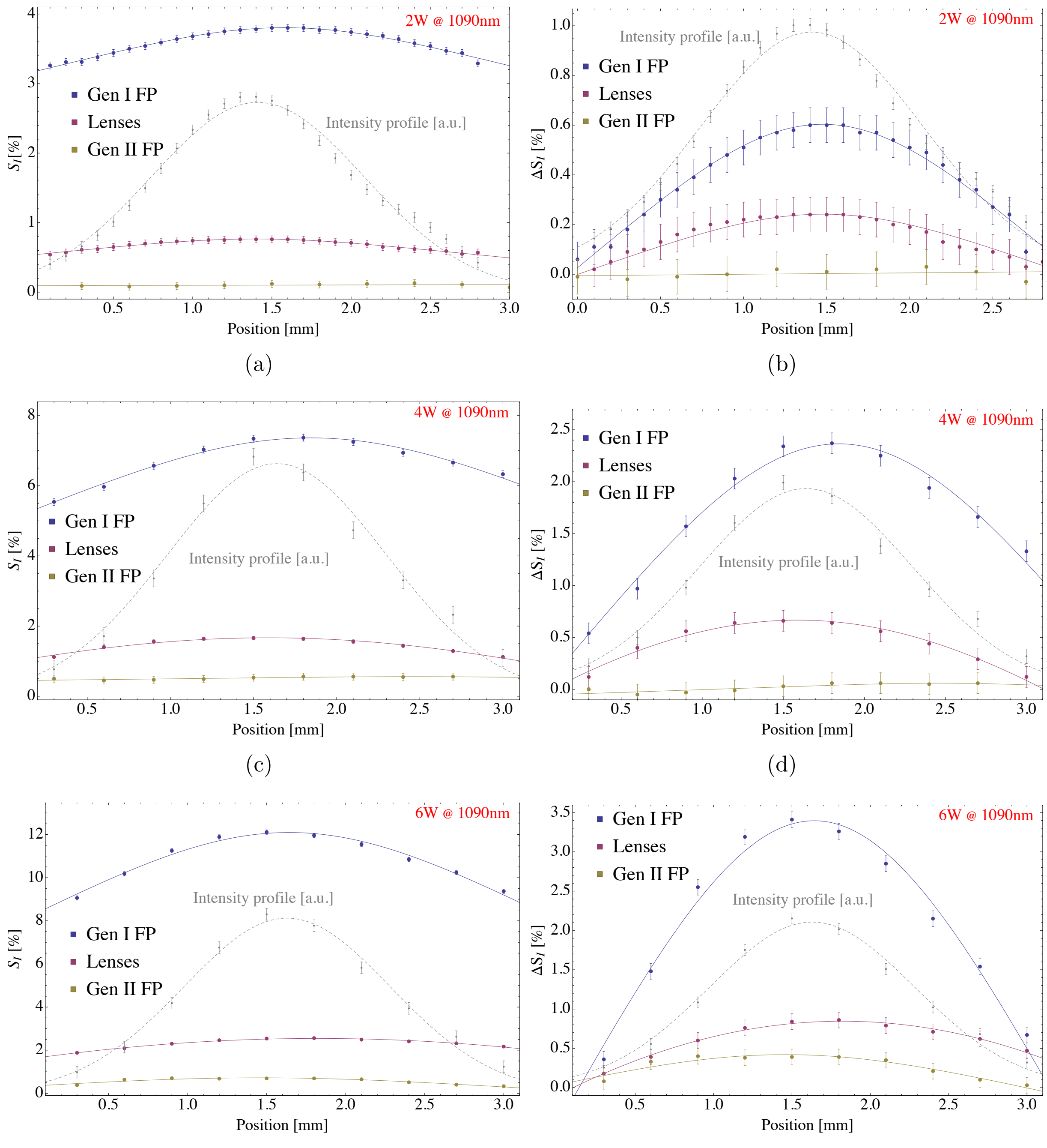

(a) (b) (c) (d) (e) (f)

FIGURE 4.6: Thermally-induced birefringence measurements for total laser powers of 2 W, 4 W, and 6 W, produced with the experimental setup shown in Fig. 4.5. The first-generation (in blue) and second-generation (in orange) field plates are compared to each other, with the separately measured contribution of the lenses (in red) substracted. All data was fitted with the function from Eq. 4.19, fit results are summarized in Table 4.3. To visualize the gradient more clearly, on the right, ΔS_I shows the same data for S_I with a substracted offset. Measurements were taken with an elongated Gaussian laser beam at 1090 nm with waists $w_x = 1.4\,\mathrm{mm} \ll w_y \simeq 30\,\mathrm{mm}$. Error bars represent a quadrature sum of statistical and systematic uncertainties discussed in Sec. 3.6. The averaging of gradients due to the aperture in front of the polarimeter is discussed in App. A.4.

Coefficient	$P_{\text{tot}} = 2$ W			$P_{\text{tot}} = 4$ W			$P_{\text{tot}} = 6$ W		
	Lenses	FP I	FP II	Lenses	FP I	FP II	Lenses	FP I	FP II
g [%/mm]	0.25(3)	0.63(3)	0.02(2)	0.65(5)	1.78(10)	0.03(5)	0.63(10)	3.45(20)	0.43(8)
o [%]	0.76(1)	3.80(1)	0.12(1)	1.68(2)	7.36(6)	0.53(2)	2.55(5)	12.10(9)	0.72(3)

TABLE 4.3: Thermally-induced gradient and offset coefficients in S/I from the fits to the data in Fig. 4.5 with the function from Eq. 4.19. The fit results are summarized for three systems (the first- and second-generation field plates, denoted as 'FP I' or 'FP II', and the lenses) at three total power values of $P_{\text{tot}} = 2$ W, 4 W, and 6 W.

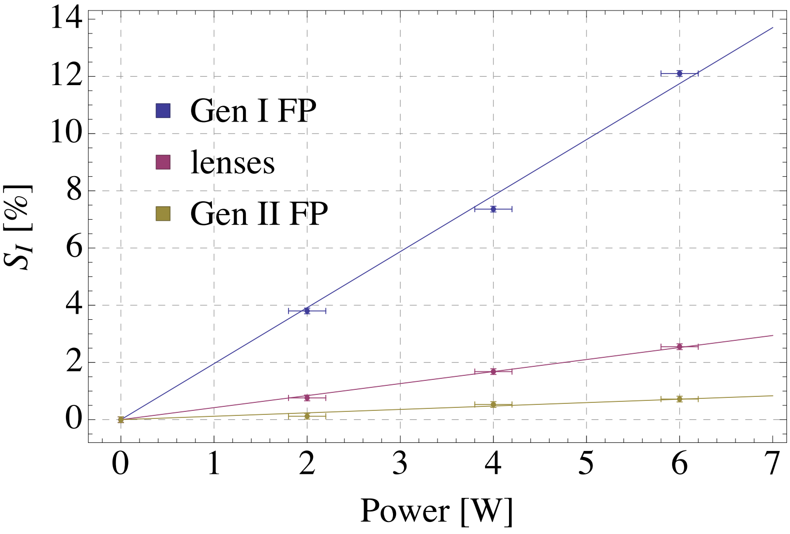

FIGURE 4.7: Thermally-induced birefringence offset $S_I(x = 0) = o$ in dependence on the total power of the laser beam P_{tot} with fit results from Table 4.3. The linear power dependence matches the prediction by Eq. 4.28. For first-generation field plates a linear fit yields $o/P_{\text{tot}} = 1.95(5)$ [%/W], for lenses $o/P_{\text{tot}} = 0.42(1)$ [%/W], and for second-generation field plates $o/P_{\text{tot}} = 0.12(1)$ [%/W]. These values agree within a factor of 1-2 with the theoretical estimate from Table 4.2.

second-generation field plates the gradient starts to be visible only at the highest power value, whereas for the first-generation field plates the gradient is on the order of $1-3\%$.

The polarization gradients observed in the first-generation polarimetry measurements on ACME were larger, on the order of $5-10\%$ with a total power of $2-4$ W [8, 9, 43]. This is due to the fact that these measurements were performed not on a separated setup, but directly on the first-generation ACME apparatus. In this case two field plates and two windows are subject to thermally-induced birefringence. In addition, the first-generation vacuum windows were made of borosilicate (BK7) glass which has a large impact on thermally-induced birefringence as discussed in the previous subsection. Therefore, the total thermally-induced S/I gradients observed on the first generation ACME experiment were a few factors larger compared to the measurements from a separated setup where the contribution of one field plate is isolated.

The fit results to the data shown in Fig. 4.6 are summarized in Table 4.3. Recall that the theoretical estimates of these coefficients are given in Table 4.2. As predicted, the gradient coefficient g is always smaller than the offset o. The ratio o/g is around $2-6\,\mathrm{mm}$ as expected from Eq. 4.24 with $w_y \simeq 30$ mm. Comparing the experimental values of o and g with theoretical estimates, we find an agreement within a factor of $1-2$. Given the simplicity of the theoretical model, and taking the uncertainty in the material properties of ITO and various imperfections into account, this agreement is very satisfying.

The offset coefficients from Table 4.3 are represented graphically as a function of the total power in Fig. 4.7. We find the expected linear dependence from Eq. 4.28. Performing a linear fit, the offset coefficients per total power can be extracted. For the first-generation field plates we obtain the value of $o/P_{\mathrm{tot}} = 1.95(5)$ %/W which is a factor of 16 larger than the corresponding value for the second-generation plates. This agrees well with the theoretical estimate from Table 4.2 where an order of magnitude difference was predicted. For lenses we find a value which is about a factor of two smaller than expected, $o/P_{\mathrm{tot}} = 0.42(1)$ %/W. The thermally-induced birefringence in lenses can be suppressed by an order of magnitude by replacing them with fused silica lenses. A lot of effort has been put to order large ($f = 200$ mm) custom-made fused silica lenses made of 'Corning 7980 0A' but unfortunately the surface quality was very unsatisfying. However, at planned laser powers of ~ 0.2 W in the second-generation ACME experiment, even the current lenses should not produce a concerning amount of thermally-induced birefringence. Fur-

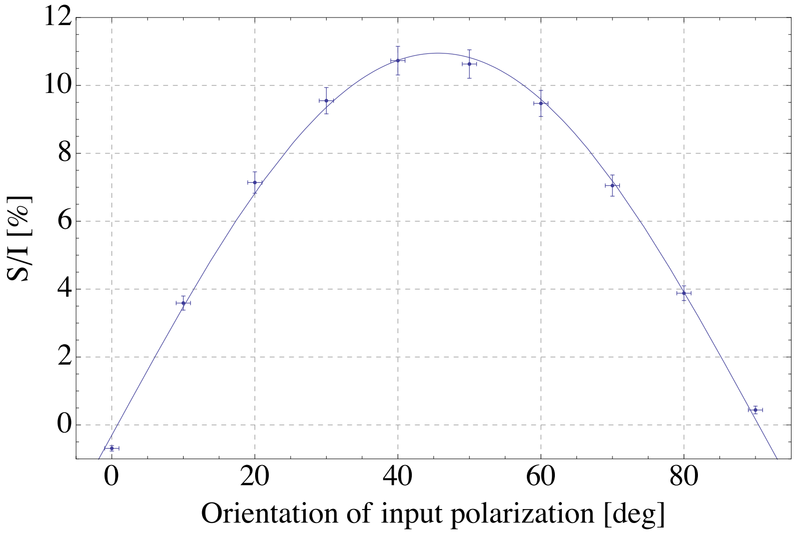

FIGURE 4.8: Thermally-induced S/I in dependence on the orientation of incoming linear polarization w.r.t. the elongated beam axes. The prediction of the beam axes defining the birefringence axis is confirmed. Measurements were performed in the center of the beam with a total power of ~ 5.5 W. The uncertainty of the power is added to the error bars on measured S/I according its linear power dependence. This makes the error bars larger for higher values of S/I.

thermore, the state preparation/refinement and readout procedure can be performed such that the birefringence axis is aligned with the state preparation/refinement and readout laser beams. This can be achieved by setting the corresponding magnetic field strength such that the phase precesses by an angle equal to integer values of 90°.

Finally, we would like to test the prediction that the birefringence axis for thermally-induced birefringence is aligned with the symmetry axes of the elongated beam. For this measurement the polarizer before the lenses, depicted in Fig. 4.5, was placed on a rotation mount. The value of S/I was recorded by the polarimeter as the input polarization orientation was varied. Measurements were performed at the center of the beam where the thermally-induced birefringence is maximized. The results are shown in Fig. 4.8. Since the output beam of the laser has some polarization, the power had to be adjusted with a power-meter every time the polarizer was rotated. This puts an additional uncertainty on S/I (according to the linear dependence on the incident laser power) which makes the error bars larger for higher values of S/I. The data is fitted with a $\cos(2\beta)$-function according to Eq. 4.2. As predicted, the impact of thermally-induced birefringence is minimized when the input polarization is aligned with the x or y axes of the elongated beam, corresponding to the orientation of input polarization of 0° or 90°. This result demonstrates that the birefringence axis matches the symmetry of the elongated beam.

4.2.3 Thermally-induced Birefringence Test on the Generation II ACME Setup

After the second-generation field plates were investigated on a separated setup, a test for thermally-induced birefringence was performed on the second-generation ACME apparatus. The setup is depicted in Fig. 4.9. We start with a circular Gaussian laser beam, $w_x = w_y = 1.4$ mm, at the wavelength of 703 nm which is used in the state preparation/refinement and readout region for the second-generation ACME measurement scheme. This laser beam is polarized by the Glan-Laser polarizer and enters the telescope consisting of two cylindrical lenses with $f = 10$ mm (Thorlabs LJ4918 or AYL1210-B) and $f = 200$ mm (Thorlabs LJ1309L1-B). After that the elongated Gaussian beam, $w_x = 1.4$ mm and $w_y \simeq 30$ mm, passes the two windows and two second-generation field plates in the vacuum region of the ACME experiment. On the other side of the vacuum chamber the polarimeter is placed on a linear translation stage to record the polarization across the x profile of the laser beam. Because of fiber coupling and impure polarization losses, the highest achievable power after the polarizer is around 1.1 W. Measurements were performed at low power, ~ 10 mW, and at the highest possible power of 1.1 W.

The results are shown in Fig. 4.10. The upper red curve is the intensity profile of the beam in the x direction. Blue and purple data points show the measurements at low power with the LJ4918 lens and the a-cylindrical AYL12010-B lens, respectively. Orange

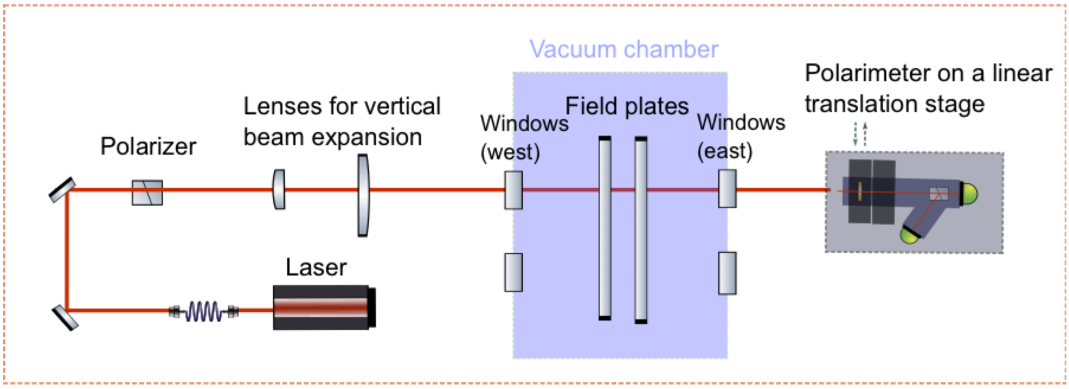

FIGURE 4.9: Setup for the thermally-induced birefringence test on the second-generation ACME apparatus. After the laser beam passes through the Glan-Laser polarizer, it is expanded in the vertical direction by two lenses with focal lengths of $f = 10$ mm and $f = 200$ mm, leading to beam waists of $w_x = 1.4$ mm and $w_y \simeq 30$ mm. Then the laser beam is transmitted through the vacuum chamber, where two vacuum windows and two field plates are on its way. Finally, the polarization of the laser beam across the x direction is measured by the polarimeter on a linear translation stage. Diagram not to scale.

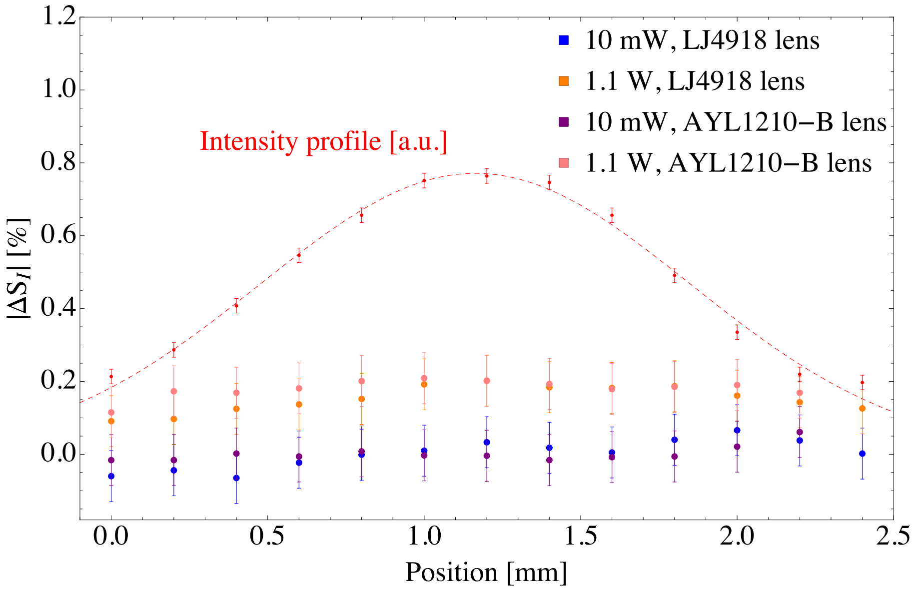

FIGURE 4.10: Measurement results of the thermally-induced birefringence test on the second-generation ACME apparatus. The upper red curve is the intensity profile of the laser beam with the wavelength of $\lambda = 703$ nm. Measurements were performed at low power (10 mW) and highest possible power (1.1 W) with two different lenses. Blue (at 10 mW) and orange (at 1.1 W) data points show measurements with the Thorlabs LJ4918 lens, purple (at 10 mW) and pink (at 1.1 W) data points were taken with the a-cylindrical Thorlabs AYL1210-B lens. No significant thermally-induced S/I is observed. Error bars represent a quadrature sum of statistical and systematic uncertainties discussed in Sec. 3.6.

and pink data points are the corresponding high-power data points. As discussed in the previous section, mechanical stress in the vacuum windows gives rise to a significant offset in S/I. This offset, $S/I \approx 14\%$, was subtracted from the measured values to visualize the contribution of the thermal effect. We find that no significant thermally-induced birefringence is produced by the intense laser beam passing through the windows and the field plates. Only a small offset of $\sim 0.2\%$ is visible. This value is approximately in agreement with the results from the separated setup. Since the power is barely sufficient to show an effect of thermally-induced birefringence we expect the value to be lower than in the linear regime. Naturally, the process would not start linearly, but rather as a more smooth higher-order dependence on the power.

For the second-generation ACME experiment the use of a five times lower power than in the above measurements is planned (~ 0.2 W). Since no concerning deviation in S/I even at ~ 1 W was observed, we conclude that thermally-induced birefringence is not an issue for systematic errors in the ACME's second-generation electron EDM measurement.

4.3 Tests of Optical Elements

This section summarizes the tests of typical optical elements used in the ACME laboratory, including half- and quarter-waveplates, windows and polarizers. Of a special interest is the polarization purity of the sideport of the Glan-Laser polarizer. This polarizer is used for polarization switching which is described in Chapter 2. A different polarization purity in the transmitted and reflected beams of the Glan-Laser polarizer could be a serious source of systematic errors [9]. The manufacturing company does not guarantee the same extinction ratio for the sideport as for the transmitted port, and even states it to produce only partially polarized. As we shall see, contrary to the specifications of the company, the laser beam coming through the sideport of the Glan-Laser polarizer is found to be as good polarized as the transmitted beam. This result is important because it means that the Glan-Laser polarizer can be undoubtedly used for polarization switching.

4.3.1 Imperfection of the Retardance in Half- and Quarter-Waveplates

Let us first consider one of the most common optical elements in the lab, the waveplates. For ACME, the imperfections of waveplates are particularly interesting, if the proposed scheme [65] to manipulate the polarization with two waveplates directly before the laser beam enters the vacuum region of the experiment is realized. However, even in the current setup, the waveplates are the last optical elements before the laser beam enters the vacuum region. Half-waveplates are used after the polarizer to dither the polarization angle and thereby measure the contrast (see Ch. 2). Imperfections of those affect the polarization which reaches the molecules.

Let us assume that we start with a horizontally polarized beam and would like to modify its polarization with the help of a waveplate with retardance δ. The incoming Stokes vector is therefore $\vec{S}_{\text{in}} = (1, 1, 0, 0)$, with the total intensity being normalized to 1. According to the Mueller calculus, the outgoing Stokes vector is

$$\vec{S}_{\text{out}} = \hat{\Gamma}(\delta, \beta) \cdot \vec{S}_{\text{in}} = \begin{pmatrix} 1 \\ \sin^2(2\beta)\cos\delta + \cos^2(2\beta) \\ \sin(4\beta)\sin^2(\delta/2) \\ \sin(2\beta)\sin\delta \end{pmatrix}, \tag{4.29}$$

where $\hat{\Gamma}(\delta, \beta)$ represents the waveplate with a retardance δ and the birefringence axis oriented at an angle β (see App. A.2 for the explicit form of this matrix). For a near half-waveplate we can approximate $\delta \simeq \pi + \Delta$ and obtain:

$$\vec{S}_{\text{HWP}} \simeq \begin{pmatrix} 1 \\ \Delta^2/4 + (1 - \Delta^2/4)\cos(4\beta) \\ (1 - \Delta^2/4)\sin(4\beta) \\ -\Delta\sin(2\beta) \end{pmatrix}. \tag{4.30}$$

The approximation $\delta \simeq \pi/2 + \Delta$ for a near quarter-waveplate yields:

$$\vec{S}_{\text{QWP}} \simeq \begin{pmatrix} 1 \\ 1/2 - \Delta/2 + (1 + \Delta)\cos(4\beta)/2 \\ (1 + \Delta)\sin(4\beta)/2 \\ (1 - \Delta^2/2)\sin(2\beta) \end{pmatrix}. \tag{4.31}$$

Note that even the perfect quarter-waveplate ($\Delta = 0$) apart from changing the amount of circular polarization also rotates the remaining fraction of linear polarization by up to 45° corresponding to a variation of M/I from 0 to 100%.

Since the definition of the absolute linear rotation angle is arbitrary, let us consider for simplicity and clarity only the relative Stokes parameters M/I and S/I. For a near half-waveplate, from Eq. 4.30 we find:

$$(M/I)_{\text{HWP}} \simeq \Delta^2/4 + (1 - \Delta^2/4)\cos(4\beta), \tag{4.32a}$$

$$(S/I)_{\text{HWP}} \simeq -\Delta\sin(2\beta). \tag{4.32b}$$

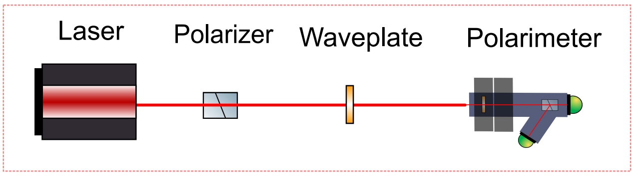

FIGURE 4.11: Experimental setup to test waveplates. The laser beam (power ∼ 10 mW, wavelength 690 nm) is polarized by the Glan-Laser polarizer and is transmitted through the waveplate which is tested. The orientation of the waveplate is changed by the rotation stage while the polarimeter measures the polarization.

Analogously, from Eq. 4.31, for a near quarter-waveplate the following expressions are valid:

$$(M/I)_{\mathrm{QWP}} \simeq 1/2 - \Delta/2 + (1+\Delta)\cos(4\beta)/2, \tag{4.33a}$$

$$(S/I)_{\mathrm{QWP}} \simeq (1 - \Delta^2/2)\sin(2\beta). \tag{4.33b}$$

We obtain the useful and interesting result that for a quarter-waveplate, the deviation from the perfect retardance has a first-order impact on circular polarization and second-order impact on linear polarization. Oppositely, for a half-waveplate, the imperfection in the retardance is a first-order effect for linear polarization and second-order for circular polarization.

Let us now consider the observations. The simple setup to test the waveplates is depicted in Fig. 4.11. We start with a low-power (∼ 10 mW) laser beam, wavelength $\lambda = 690$ nm, which is polarized by the Glan-Laser polarizer. The waveplate is placed on a rotation stage between the polarizer and the polarimeter. The orientation of the waveplate is changed in gradual steps, typically 4°. Within each step the polarimeter measures the outgoing polarization.

Here, we present measurements of three zero-order half-waveplates and three zero-order quarter-waveplates. For each of the two waveplate categories, following types were chosen: an achromatic waveplate, a monochromatic waveplate at the closest to $\lambda = 690$ nm available specified wavelength, and a monochromatic waveplate with the specified wavelength being substantially different from the used wavelength of $\lambda = 690$ nm. For each waveplate, the data is fitted with Eqs. 4.32 (for half-waveplates) or Eqs. 4.33 (for quarter-waveplates). The value of Δ is determined from the fit of the relative Stokes parameter which is most sensitive to a change in retardance. As discussed above, for half-waveplates the value of S/I is most affected by Δ, whereas for quarter-waveplates it is M/I. The measurement results are reported in Table 4.4 and displayed in Figs. 4.12 and 4.13.

Let us first examine Fig. 4.12 where the measurements from half-waveplates are depicted. Note that the initial birefringence axis orientation is different for each waveplate

Waveplate type	Specified wavelength	Part number (TL = Thorlabs, NP = Newport)	Measured Δ, from fits shown in Figs. 4.12(a) and 4.13(b) [rad]
Quarter-Waveplates			
Achromatic	690-1000 nm	NP 10RP54-2	0.008(3)
Monochrom.	694 nm	TL WPQ05M-694	0.019(2)
Monochrom.	532 nm	NP 05RP34-532	0.417(3)
Half-Waveplates			
Achromatic	690-1200 nm	TL AHWP05M-980	0.0935(3)
Monochrom.	694 nm	TL WPH05M-694	0.0288(2)
Monochrom.	633 nm	TL WPH05M-633	0.2557(6)

TABLE 4.4: Overview of the tested half- and quarter-waveplates with corresponding part numbers. The measurements were performed at $\lambda = 690$ nm with results presented in Figs. 4.12 and 4.13. In the last column the values for the retardance deviation Δ from the perfect case of a half- or quarter-waveplate are written. They were extracted from fits to the data in Figs. 4.12(b) and 4.13(a) according to Eqs. 4.32b and 4.33a.

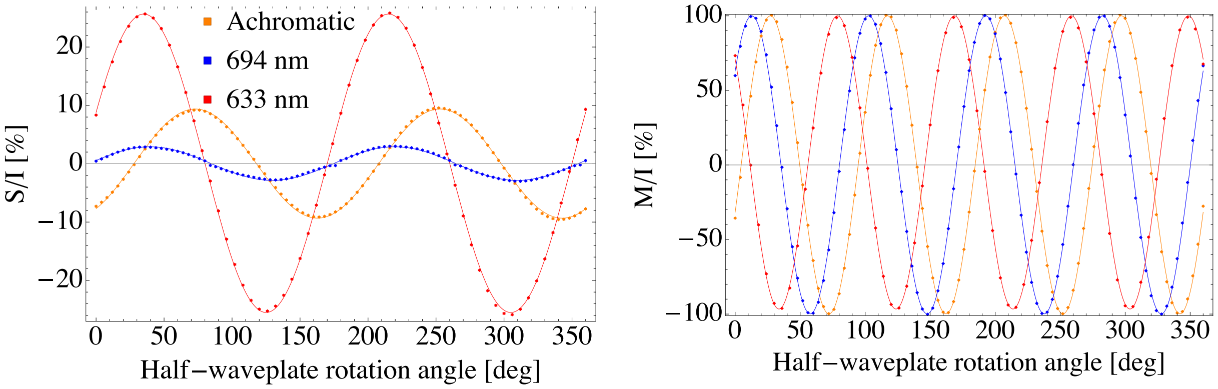

(a)

(b)

FIGURE 4.12: Polarimetry measurements for the three half-waveplates (HWP) listed in Table 4.4: achromatic HWP (orange), monochromatic HWP for 694 nm (blue), monochromatic HWP for 633 nm (red). (a) Circular polarization represented by the relative Stokes parameter S/I with fits according to Eq. 4.32b (b) Linear polarization represented by the relative Stokes parameter M/I with fits according to Eq. 4.32a.

which is why the curves are shifted w.r.t. each other. Looking at linear polarization, M/I in Fig. 4.12(b), we barely see a difference between the waveplates. This observation follows our prediction from Eq. 4.32(a) where a small Δ is a second-order deviation from the perfect case of a half-waveplate. On the contrary, in the data for S/I, Fig. 4.12(a), we see a substantial difference since Δ enters Eq. 4.32(b) to a first order. As expected, the best half-waveplate is the monochromatic one specified for $\lambda = 694$ nm. However, this waveplate still produces elliptical polarization with an S/I of up to $\sim 3\%$ which corresponds to $\Delta \sim 3 \cdot 10^{-2}$ rad. Given a small deviation of 4 nm from the specified wavelength which leads to $\Delta \sim 1 \cdot 10^{-2}$ rad, and the specified retardance accuracy of

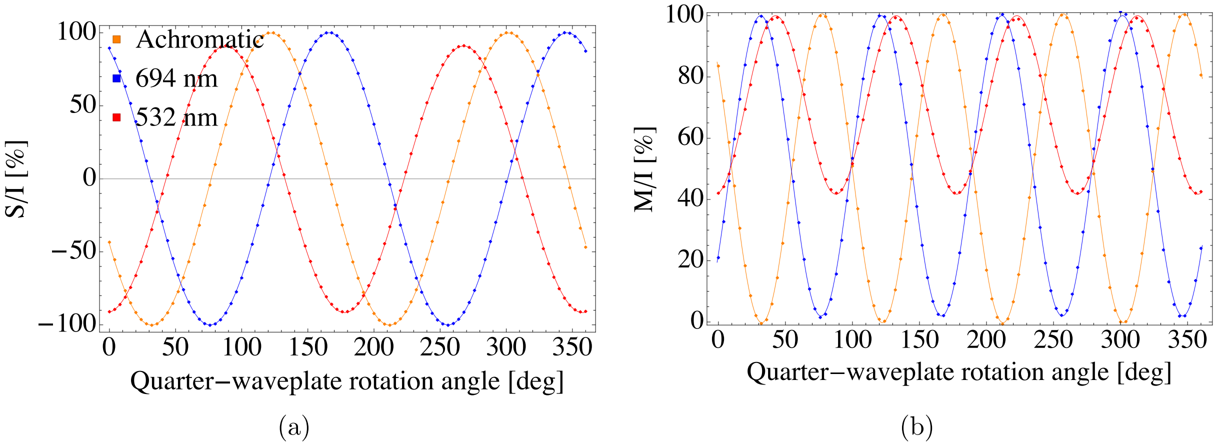

(a) (b)

FIGURE 4.13: Polarimetry measurements for the three quarter-waveplates (QWP) listed in Table 4.4: achromatic QWP (orange), monochromatic QWP for 694 nm (blue), monochromatic QWP for 532 nm (red). (a) Circular polarization represented by the relative Stokes parameter S/I with fits according to Eq. 4.33b (b) Linear polarization represented by the relative Stokes parameter M/I with fits according to Eq. 4.33a.

$\lambda/300$ which translates into $\Delta \sim 2 \cdot 10^{-2}$ rad, this value is just within our expectations. The achromatic waveplate is designed with a retardance accuracy of $\lambda/55$ corresponding to $\Delta \sim 10^{-1}$ rad which matches our observed value of $\Delta = 0.0935(3)$ rad. It is interesting to compare this number to the monochromatic half-waveplate for 633 nm which produces an S/I of up to $\sim 25\%$ with $\Delta = 0.2557(6)$ rad.

The measurement results for quarter-waveplates are shown in Fig. 4.13. As expected, the deviation Δ from the perfect case of a quarter-waveplate has a smaller impact on circular polarization represented by S/I than for linear polarization represented by M/I. Even the monochromatic waveplate for 532 nm, see red data points in subfigure (a), shows little deviation from the perfect behavior of a quarter-waveplate for S/I. On the contrary, if we look on corresponding red points for M/I in subfigure (b), this deviation is substantial. Instead of varying between 0% and 100%, the value of M/I reaches values only between $\sim 40\%$ and 100%. Comparing the data for the achromatic waveplate (in orange) and monochromatic waveplate for 694 nm (in blue), we surprisingly find that the achromatic one is closer to the perfect scenario. Looking at the value of Δ in Table 4.4, for the achromatic waveplate we find $\Delta \sim 0.01$ rad compared to $\Delta \sim 0.02$ rad for the monochromatic one. However, the last value is also within our expectations from the specifications of the retardance accuracy of $\lambda/300$ corresponding to around the same value of $\Delta \sim 0.02$ rad.

To summarize, for typical waveplates we find an imperfection in the retardance at least on the order of $\Delta \sim 10^{-2}$ rad. This leads to the deviation of at least few percent from the perfect behavior in the relative Stokes parameters. To achieve better retardance values, one could make use of the mechanical stress birefringence by applying a small stress on the waveplate (e.g. with little screws).

4.3.2 Mechanical Stress Birefringence in Broadband Precision Windows

As discussed in Sec. 4.1, mechanical stress leads to birefringence. Apart from investigating stress-induced birefringence in the large vacuum windows, smaller and thinner circular windows of one or two inches diameter with a thickness of 5 or 12 mm were tested. These broadband precision windows are for example used for reference cavities. The part numbers are Thorlabs WG11050-B, WG12012, and WG41050-B.

Even given the fact that two different glass substrates were used (borosilicate N-BK7 and fused silica UVFS), no significant difference was observed between the windows. Without tightening the windows onto their mounts, almost no birefringence was observed and the value of S/I was different from zero by only $0.1 - 0.2\%$. However, when the windows are only slightly fixed onto their mounts, an increase in the measured S/I is observed on the order of fractions of per cent. When tightening them with a typical strength, the value of S/I is around $1 - 3\%$.

To investigate the stress-induced birefringence in windows more quantitatively, a separated setup would be needed where one could determine the applied stress. However, in practice this investigation would not be very useful since one does not typically measure the stress while mounting the windows. Instead, one could measure the birefringence directly. As a rule of thumb, when using the windows with usual mounts, one may expect a change in the relative Stokes parameters of a few percent.

4.3.3 Extinction Ratio of a Polarizers

As other optical elements, polarizers are not ideal. Their performance is limited by the extinction ratio $r = I_{\mathrm{min}}/I_{\mathrm{max}}$ which is defined as the ratio of the smallest achievable intensity after a succession of two identical polarizers, I_{min}, and the corresponding largest possible intensity, I_{max}.

In a simple model of a partial polarizer, light is perfectly transmitted along one axis whereas along the orthogonal axis only a small fraction r of the incoming light intensity remains. The Mueller matrix $\hat{P}_{\mathrm{imp}}(\alpha)$ for such an optics, where α is the orientation of the transmission axis, is given in App. A.2. From this model, let us determine the residual fraction of circular polarization after the imperfect polarizer in dependence on the incoming value of S/I. The largest variation of the relative fraction of circular polarization S/I can be produced by a quarter-waveplate. Assuming linearly polarized light going into the waveplate, the Stokes vector after the quarter-waveplate, $\vec{S}_{\mathrm{QWP}}$, is given by Eq. 4.29 with $\delta = \pi/2$ (where we neglect imperfections in the retardance). The value of S/I after linear polarized light passed through the quarter-waveplate is:

$$(S/I)_{\mathrm{QWP}} = \sin(2\beta), \tag{4.34}$$

where β is the orientation of the birefringence axis of the waveplate. This value of S/I enters the imperfect polarizer whose ability to suppress circular polarization we wish to determine. We can calculate the Stokes vector after the polarizer as

$$\vec{S}_{\text{out}} = \hat{P}_{\text{imp}}(\alpha) \cdot \vec{S}_{\text{QWP}}. \tag{4.35}$$

From the ratio of the last and first components of this vector, we obtain the following value for S/I after the polarizer:

$$(S/I)_{\text{out}} \simeq \frac{4\sqrt{r}\sin(2\beta)}{\cos(4\beta - 2\alpha) + \cos(2\alpha) - 2}, \tag{4.36}$$

where we expanded the solution in series for small r and kept the leading term only. Therefore, we expect a residual fraction of circular polarization of up to $2\sqrt{r}$ having a polarizer with an extinction ratio of r. For a typical polarizing beam splitter, r is around $10^{-3} - 10^{-4}$ which leads to a residual S/I of $2 - 6\%$. Glan-Laser polarizers have $r < 10^{-5}$ and should therefore produce a residual fraction of circularly polarized light of less than 0.6%.

Let us now turn to the experimental test of polarizers. The setup is depicted in Fig. 4.14(a). We start with a laser beam ($\sim$ 10 mW, 690 nm) which is polarized and passes through a quarter-waveplate on a rotation stage to obtain a varying elliptical polarization as in Eq. 4.34. The polarizer which we wish to test is placed between the waveplate and the polarimeter. The incoming S/I into the polarizer is gradually changed by the rotation stage of the waveplate, and the outgoing S/I is measured by the polarimeter. We compare the suppression properties of a usual polarizing beam splitter (Thorlabs PBS102-B) to a Glan-Laser polarizer (Thorlabs GL10-B).

The results are shown in Fig. 4.14(b). The S/I before the tested polarizer is depicted in orange with a fit according to Eq. 4.34. This data was taken separately by removing the polarizer between the waveplate and the polarimeter. The right orange scale demonstrates that the incoming S/I varies between approximately -100% and 100% as expected. The left blue scale refers to the data with a tested polarizer suppressing this incoming circular polarization.

For the polarizing beam splitter we find a residual S/I of up to $\sim 3\%$ agreeing with our estimates above, see circled blue data points. This data is fitted with a function from Eq. 4.36. Naively one may expect that the S/I after the suppression of the polarizer follows the $\sin(2\beta)$-function of the incoming S/I. However, as we found from Eq. 4.36 this is not the case and the shape of the $\sin(2\beta)$-dependence is highly distorted. Looking at the observed variation of S/I, this prediction is clearly confirmed which supports our model of the imperfect polarizer. However, we also find that the variation of S/I after the polarizer is not symmetric around zero, but has an offset of $\sim 1\%$ which was not predicted by the

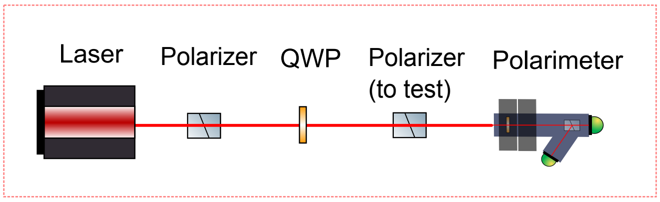

(a)

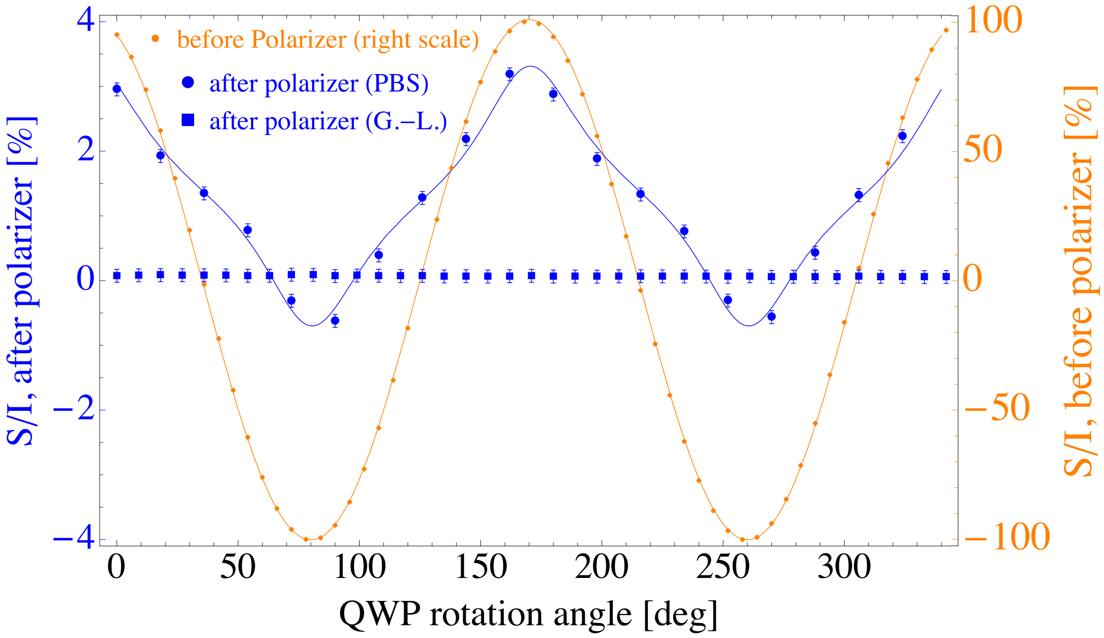

(b)

FIGURE 4.14: Test of how well the polarizing beamsplitter cube and the Glan-Laser polarizer suppress the circular polarization (a) Experimental setup. The varying fraction of circular polarization is produced by a polarizer followed by a quarter-waveplate (QWP) on a rotation stage. The polarizer whose suppression properties we wish to determine is placed directly afterwards, with a polarimeter measuring the outgoing polarization. (b) Measurement results. The orange data points with the right scale show the relative fraction of circular polarization S/I before the tested polarizer, varying between -100% and 100% according to Eq. 4.34. The blue data points with a left scale show the suppressed S/I after the tested polarizer. Circled points with a fit according to Eq. 4.36 represent a typical polarizing beam splitter (PBS) where the residual variation of S/I is clearly visible. Squared data points which show almost no residual S/I refer to measurements with a Glan-Laser polarizer with a much better extinction ratio.

model. This shows the limitation of the simple model where we neglected some possible changes of internal birefringence properties, for instance due to the cement between the two prisms, or depolarization effects.

In contrary to the polarizing beam splitter, no variation of outgoing S/I from the Glan-Laser polarizer is measured, see squared blue data points. The residual S/I is around 0.1% corresponding to an extinction ratio $r \simeq 3 \cdot 10^{-7}$ which is smaller than the specified $r \lesssim 10^{-5}$. Given the fact that some companies offer Glan-Laser polarizers with an extinction ratio of $r < 10^{-8}$ upon request [11], the extinction ratio of our polarizer is not surprising, though it is better than expected. Since our polarimeter is limited by systematic errors on the order of $\sim 0.1\%$ (as discussed in Sec. 3.6.6), a better extinction ratio is not needed for our purposes. In addition to the Glan-Laser polarizers, also the Glan-Taylor, Glan-Thompson and Wollaston polarizers have been tested. They all showed a residual S/I of 0.1% or less.

4.3.4 Extinction Ratio of the Sideport of the Glan-Laser Polarizer

As described in Sec. 2.3, in the ACME experiment the polarization of the readout laser beam needs to be rapidly switched between the orthogonal states of linear polarization in order to normalize the measured phase against molecule number fluctuations. If the average ellipticity between the two switched polarizations is non-zero, the polarization switching could contribute to AC Stark shift phases causing a systematic error [9].

To implement the polarization switching scheme, a polarizer which splits the beam into orthogonal ordinary and extraordinary rays is most practical. As we have seen in the previous subsection, usual polarizing beam splitters do not produce a pure enough polarization. Not all the polarizers provide the opportunity to use both beams, e.g. the Glan-Thompson polarizer is only designed with a transmission port. In addition, the polarizer has to be immune against the high intensities used in the ACME experiment.

The Glan-Laser polarizer has one of the best available extinction ratios, features a sideport and is suitable for high intensities. However, the extinction ratio is only specified for the transmission port, and not for the sideport which was thought to produce only partially polarized light.[2] Nevertheless, after looking closer at the design of the Glan-Laser polarizer in Chapter 3, recall Fig. 3.6(b), we have good reasons to believe that the reflected ordinary ray has a very pure polarization. The small portion of the extraordinary ray which could diminish the polarization purity escapes the sideport at a different angle. The two reflected rays are separated by $\sim 7°$ and can easily be distinguished from each other. Therefore, we predict the reflected ordinary ray to have a high extinction ratio. Indeed, the residual fraction of circular polarization from the sideport of the Glan-Laser polarizer was measured with the polarimeter and, as we shall see below, was found to be around 0.1% as in the transmitted port.

---

[2] Thorlabs states in the description of the Glan-Laser polarizer: '*Extinction ratio is only defined for the output ray. A significant amount of reflected light escapes the polarizers through the side port, including all of the ordinary ray and some of the extraordinary ray. As such, the escape ray is not fully polarized. The output ray has a very pure polarization with an extinction ratio of 100 000:1. While these transmitted extraordinary rays are highly polarized, the reflected ordinary rays are only partially polarized.*' [93]

Like for the polarizer tests in the previous subsection, we measure the residual fraction of circular polarization S/I from the sideport in dependance on the circular polarization coming from a polarizer followed by the quarter-waveplate as described by Eq. 4.34. This leads to highest possible incoming S/I of around 100% corresponding to fully circular polarized light and therefore to the 'worst case scenario' for a polarizer whose purpose is to suppress circular polarization. Since the transmitted and reflected beams of the Glan-Laser polarizer are orthogonally polarized, the sideport can be modeled as a polarizer rotated by 90° with a corresponding Mueller matrix $\hat{P}(90°)$ (see App. A.2 for its explicit form). The Stokes vector of the beam coming out of the sideport can therefore be calculated as $\vec{S}_{\text{sideport}} = \hat{P}(\pi/2) \cdot \vec{S}_{\text{QWP}}$ with $\vec{S}_{\text{QWP}}$ from Eq. 4.29 with $\delta = \pi/2$. Comparing the first component of $\vec{S}_{\text{sideport}}$ to Eq. 4.34 we find that the intensity transmitted through the sideport varies with the same dependence on β as $(S/I)_{\text{QWP}}$:

$$I_{\text{sideport}}(\beta) = I_0 \sin^2(2\beta) = I_0 \, (S/I)^2_{\text{QWP}}. \tag{4.37}$$

By fitting the transmitted intensity through the sideport, we can therefore deduce the incoming circular polarization after the quarter-waveplate.

The experimental setup is shown in Fig. 4.15(a). The laser beam ($\sim$ 10 mW, 690 nm) passes through the polarizer followed by a quarter-waveplate on a rotation stage to produce a varying fraction of circular polarization as in Eq. 4.34. After that the light enters the Glan-Laser polarizer. The transmitted beam is blocked whereas the polarization from the sideport is monitored by the polarimeter while the quarter-waveplate is gradually rotated.

The measurement results are presented in Fig. 4.15(b). The gray data points with a dashed fit curve represent the transmitted intensity through the sideport. From this intensity, according to Eq. 4.37, we deduce the relative fraction of circular polarized light before the Glan-Laser polarizer and after the quarter-waveplate, $(S/I)_{\text{QWP}}$, see the orange curve with the right scale. The blue data points show the S/I measurements from the sideport revealing a very pure polarization with a residual fraction of circular polarized light of around 0.1%. No variation of residual S/I in dependence on the incoming S/I is detected. Based on the discussion in the previous subsection 4.3.3, we therefore conclude that the sideport has the same extinction ratio as for the transmitted beam of $r < 10^{-6}$. This result has been communicated with Thorlabs.

Since we demonstrated that both ports of the Glan-Laser polarizer have the high extinction ratio to produce very pure linear polarized light, this polarizer meets the requirements for polarization switching on ACME. Note that in this case the sideport is used as the incoming port whereas in our measurements above, see Fig. 4.15(a), it is the port for the outgoing beam. If unpolarized or partially polarized light enters the sideport, it will be separated into an ordinary and extraordinary ray. Because the beam enters the sideport

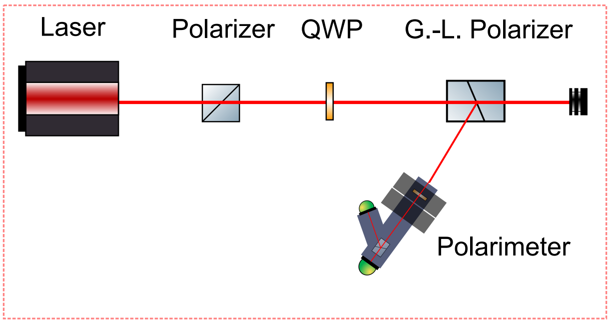

(a)

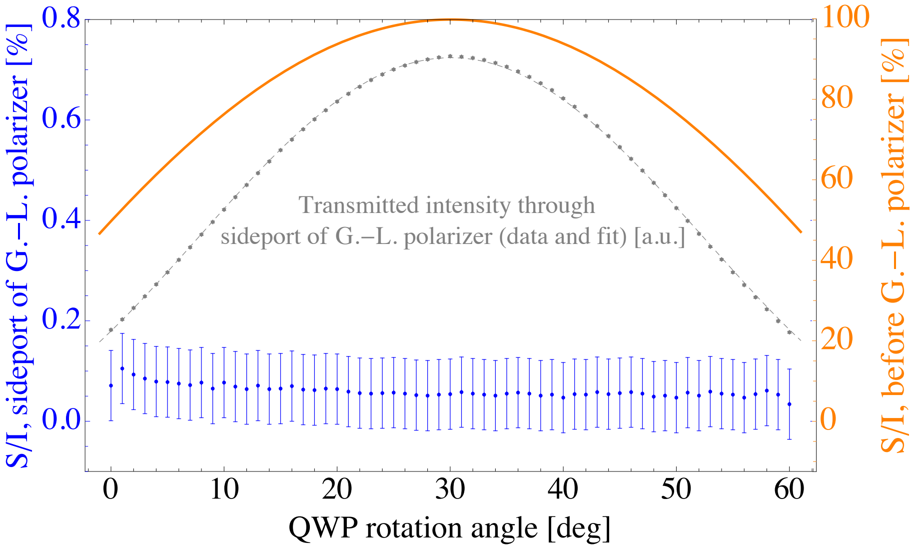

(b)

FIGURE 4.15: Measurement of polarization purity from the sideport of the Glan-Laser polarizer (a) Experimental setup. The varying fraction of circular polarization is produced by a polarizer followed by a quarter-waveplate (QWP) on a rotation stage. The Glan-Laser polarizer is placed afterwards, with the transmitted beam being blocked and the beam from the sideport being measured by the polarimeter. (b) Measurement results. The transmitted intensity through the sideport in dependence on the QWP rotation angle is represented by gray data points. From this data the S/I after the QWP was deduced according to Eq. 4.37, see the orange curve with the right scale. The blue data points with the left scale refer to S/I measurements from the sideport. No variation of the residual S/I is observed which is around 0.1% independent of the incoming polarization. Error bars represent a quadrature sum of systematic and statistical uncertainties (see Sec. 3.6).

of the polarizer at an angle of $\sim 66°$, see Fig. 3.6(b), the two rays will be spatially separated since they are not parallel or orthogonal to the optical axis of the crystal. Due to the Fermat's principle of light, the ordinary ray follows the same path as in the mirrored case where it goes in the opposite direction like our test setup of Fig. 4.15(a). The extraordinary ray will be emitted at a different angle and therefore does not disturb the ordinary ray which we care about. Therefore, the sideport of the Glan-Laser polarizer can unquestionably be used for polarization switching of the ACME readout laser beam.

5 Summary

This thesis presents a contribution to the second-generation ACME experiment which aims for the most precise electron electric dipole moment (EDM) measurement. A more precise limit on the electron EDM restricts various models of particle physics beyond the Standard Model and is important for the progress in fundamental physics, in particular for the research on the matter-antimatter asymmetry of the universe. The ACME collaboration utilizes the great advantage of a high effective electric field in a thorium monoxide molecule to perform a spin-precession measurement in a carefully chosen state allowing to suppress many possible systematic errors.

The leading systematic errors in the first generation of the ACME experiment are due to imperfect polarizations present in the laser light preparing and reading out the states of the molecules. In particular, a high intensity laser propagating through glass plates coated with indium tin oxide deposits heat onto the plates, thereby leading to thermally-induced birefringence. In addition to the known procedures to suppress this systematic error in the ACME's first-generation measurement, future generations of the ACME experiment use field plates with improved thermal and optical characteristics as well as lower laser intensities to minimize this effect. A precise characterization of the laser light polarization is needed to monitor the polarization purity on ACME as well as to test the thermally-induced birefringence in the new field plates. Therefore, polarimetry is a focus of this thesis.

A self-calibrating polarimeter with an improved performance that allows to carefully characterize the polarization state of the ACME experiment lasers, in particular the ellipticity present in the laser beam, has been developed in this work. This device precisely determines the relative Stokes parameters that characterize the polarization of laser light. In comparison to previous laboratory realizations and commercially available polarimeters, the polarimeter presented in this thesis is more precise, has high power-handling capabilities, is immune against intensity fluctuations in the measured laser beam, and is calibrated internally without the need for removing or realigning any optical elements. The calibration procedure is critical for the low uncertainties that have been achieved. A detailed study of various systematic uncertainties shows that the relative amount of circular polarization can be measured to better than 0.1%.

The polarimeter's usefulness is demonstrated by performing various polarimetry measurements on ACME. In particular, the first-generation field plates are directly compared to the new field plates in terms of the thermally-induced birefringence. The characterization of circular polarization across a nominally linearly polarized laser beam reveals a greatly suppressed thermally-induced polarization change in the second-generation field plates. Furthermore, the stress-induced birefringence in vacuum windows is found to be of no concern. Various optical elements such as waveplates and polarizers are investigated. Contrary its specifications, the sideport of the Glan-Laser polarizer is found to produce very pure linear polarization and can therefore be undoubtedly used for polarization switching on ACME.

To conclude, a polarimetry test on the second-generation ACME setup demonstrates that the circular polarization gradient is below 0.1% even at the highest possible second-generation laser intensity. This value is one to two orders of magnitude lower than in ACME's first-generation apparatus. Therefore, the polarization of laser light for the second-generation electron EDM measurement is well under control. The substantial reduction of thermally-induced birefringence as well as the precise monitoring of polarization with the improved polarimeter described in this thesis are crucial for suppressing and excluding systematic errors in future generations of ACME.

A Appendix

A.1 Estimate of the Baryon-to-Photon Ratio

Even at night, our universe is full of ‘light’ - not visible light, though, but microwave radiation from the Cosmic Microwave Background (CMB). Remarkably, on average all the photons coming from visible light (for instance from all the stars) are negligible in comparison to the number of photons from the CMB. Therefore, the present average density of photons in our universe is approximately $n_\gamma \simeq 400/\mathrm{cm}^3$ which is simply given by the $T \simeq 2.7\,\mathrm{K}$ cold blackbody radiation distribution:

$$n_\gamma = \frac{2\zeta(3)}{\pi^2}\left(\frac{k\,T}{\hbar\,c}\right)^3, \tag{A.1}$$

with $2\zeta(3)/\pi^2 \simeq 0.244$. The density of baryons is around a billion times smaller, today we find on average one baryon per four cubic meters. However, as we shall see below, this number is huge compared to the estimate from the standard cosmological model which points to the lack of understanding of the origin of baryons in our universe.

Note that the baryon-to-photon ratio n_b/n_γ remains constant after the baryons decouple from thermal equilibrium. While the number of baryons is conserved to a very good approximation, as the universe expands, their density is decreased with the third power of the universe scale factor a, $n_b \propto a^{-3}$. The number density of photons is given by the blackbody-radiation temperature T of the universe and scales as $n_\gamma \propto T^3$. Our universe cools down and the temperature of the CMB decreases as $T \propto a^{-1}$ [62]. Therefore, the ratio n_b/n_γ is ‘frozen’.

We set throughout the following calculation $\hbar = c = k = 1$. The temperature of the photon field when baryons and anti-baryons stop annihilate is determined by the ‘freeze-out’ condition:

$$\Gamma \simeq H, \tag{A.2}$$

where Γ is the interaction rate and H is the expansion rate of the universe determined by the Hubble equation:

$$H = \sqrt{\frac{8\pi G}{3}\rho}, \tag{A.3}$$

where G is the gravitational constant and ρ the total energy density. In the beginning, our universe was radiation dominated. This era lasted for thousands of years. When the baryons decoupled from thermal equilibrium, our universe was younger than a second, even a millisecond [62]. At that time certainly being radiation dominated, the energy density of the universe is given by the Stefan-Boltzmann law:

$$\rho = \frac{\pi^2}{30} g^* T^4, \tag{A.4}$$

where $g^* = \sum_B g_B + 7/8 \sum_F g_F$ is the effective number of the degrees of freedom for relativistic species consisting of bosons with g_B and fermions with g_F [62]. Therefore, the expansion rate of the universe in a radiation dominated era is given by:

$$H = \sqrt{\frac{8\pi^3\, g^*}{45}} \frac{T^2}{M_{\mathrm{Pl}}}, \tag{A.5}$$

where we inserted the Planck mass $M_{\mathrm{Pl}} = \sqrt{\hbar c/G} = 1/\sqrt{G} \simeq 1.2 \cdot 10^{19}\,\mathrm{GeV}$.

The interaction rate is given by $\Gamma = n_b \langle \sigma v \rangle$, where n_b is the baryon density, σ the interaction cross section and v the velocity of baryons [62]. The product $\langle \sigma v \rangle$ for the nucleon-antinucleon annihilation is approximately given by the inverse of the mass of the pion squared, $\langle \sigma v \rangle \simeq 1/m_\pi^2$ with $m_\pi \simeq 140\,\mathrm{MeV}$. This relation goes back to Quantum Chromodynamics, where the interaction between nucleons can be approximated by a pion exchange, and agrees with experimental data from colliders [67].

From statistical mechanics, we know that the number density of non-relativistic particles with energy $E(\vec{p}) \simeq m \gg T$ in thermal equilibrium is given by

$$n = \frac{g}{(2\pi)^{3/2}} \int f(\vec{p}) \mathrm{d}^3 p \simeq \frac{g}{(2\pi)^{3/2}} (mT)^{3/2} \mathrm{e}^{-m/T}, \tag{A.6}$$

where g is the number of the degrees of freedom (e.g. spin states) and $f(\vec{p}) = [\exp(E(\vec{p})/T) \pm 1]^{-1} \simeq \exp(-m/T)$ is the Fermi-Dirac or Bose-Einstein distribution. Therefore, for temperatures $T \ll m_b \simeq 0.94\,\mathrm{GeV}$ the baryon density in thermal equilibrium is given by:

$$n_b \simeq \frac{g_b}{(2\pi)^{3/2}} (m_b T)^{3/2} \mathrm{e}^{-m_b/T}. \tag{A.7}$$

The baryon density is given by Eq. A.7 as long as baryons are in thermal equilibrium. The 'frozen' baryon density is determined by the last moment when baryons were in thermal equilibrium. This 'last moment' is approximately derived by the condition of Eq. A.2. Using Eqs. A.7 and A.5, Eq. A.2 simplifies to:

$$\sqrt{m_b/T}\, \mathrm{e}^{-m_b/T} \simeq \sqrt{\frac{4}{45}\pi^3} \frac{\sqrt{g^*}}{g_b} \frac{m_\pi^2}{M_{\mathrm{Pl}}\, m_b} \simeq 1.3 \cdot 10^{-20}, \tag{A.8}$$

where $g^* = 10.75$ (photons, three neutrinos species, electrons and positrons, two spin orientations) and $g_b = 4$ (protons and neutrons with two spin orientations). Solving this equation numerically, we find $m_b/T \sim 50$ which means that the baryon density freezes out at $T \sim m_b/50 \sim 20\,\mathrm{MeV}$. Inserting this temperature into corresponding expressions for n_b (Eq. A.7) and n_γ (Eq. A.1) yields:

$$\frac{n_b}{n_\gamma} \sim 10^{-18} - 10^{-20}. \tag{A.9}$$

This result is in agreement with [13, 23].

In the above derivation we neglected the chemical potential μ. That is why our estimate predicts the same number of baryons and anti-baryons. Taking the chemical potential into account, one can show that the excess of particles over antiparticles is given by [62]:

$$n_b - n_{\bar{b}} \simeq \frac{g_b\,T^3}{6\,\pi^2}\frac{\partial J_{\mp}^{(3)}}{\partial \beta}, \tag{A.10}$$

where $\beta \equiv \mu/T$ and $J_{\mp}^{(3)}$ is a lengthy function given in [62] dependent on β and $\alpha \equiv m_b/T$. The chemical potential is determined by the sum over the relevant quantum numbers Q_a: $\mu = \sum_a Q_a \mu_a$ [98]. Eq. A.10 illustrates how the matter-antimatter asymmetry can arise.

However, even if we assume that in our above estimate all the anti-baryons are washed away, the discrepancy between the observed baryon-to-photon ratio of $\sim 10^{-9}$ and our estimate of $\sim 10^{-18}$ will remain. This nine order of magnitude difference is a striking indication for our lack of understanding of the origin of matter in our universe. Note that the 'freeze-out' of baryons happens at around 20 MeV where no 'new physics' is present. This means that there must be a mechanism which produces an excess of baryons over anti-baryons before they decouple from thermal equilibrium – called 'baryogenesis' [13, 56]. In this case a constant baryon density from baryogenesis adds to Eq. A.7.

A.2 Mueller Matrices

The Mueller matrices can be found in the standard literature on optics and polarization [36, 20, 52, 10, 83]. Here we give the explicit form of Mueller matrices used in this thesis. This includes a waveplate, a perfect polarizer and an imperfect polarizer.

The Mueller matrix for a waveplate with retardance δ and the fast axis aligned with the reference plane is:

$$\hat{\Gamma}(\delta, 0) = \begin{pmatrix} 1 & 0 & 0 & 0 \\ 0 & 1 & 0 & 0 \\ 0 & 0 & \cos\delta & \sin\delta \\ 0 & 0 & -\sin\delta & \cos\delta \end{pmatrix} \tag{A.11}$$

The Mueller matrix for a linear polarizer with its transmission axis aligned with the reference plane is:

$$\hat{P}(0) = \frac{1}{2}\begin{pmatrix} 1 & 1 & 0 & 0 \\ 1 & 1 & 0 & 0 \\ 0 & 0 & 0 & 0 \\ 0 & 0 & 0 & 0 \end{pmatrix} \tag{A.12}$$

In the simplest model, the imperfect linear polarizer with a finite extinction ratio r perfectly transmits light along one axis whereas along the orthogonal axis only a small fraction r of the incoming light intensity remains. The Mueller matrix for such an optics is:

$$\hat{P}_{\mathrm{imp}}(0) = \frac{1}{2}\begin{pmatrix} 1 & 1-2r & 0 & 0 \\ 1-2r & 1 & 0 & 0 \\ 0 & 0 & 2\sqrt{r(1-r)} & 0 \\ 0 & 0 & 0 & 2\sqrt{r(1-r)} \end{pmatrix} \tag{A.13}$$

A rotation by an angle θ is described by the matrix:

$$\hat{R}(\theta) = \begin{pmatrix} 1 & 0 & 0 & 0 \\ 0 & \cos(2\theta) & -\sin(2\theta) & 0 \\ 0 & \sin(2\theta) & \cos(2\theta) & 0 \\ 0 & 0 & 0 & 1 \end{pmatrix} \tag{A.14}$$

For rotated optical components the Mueller matrices transform as:

$$\hat{M}(\theta) = \hat{R}(\theta)\hat{M}(0)\hat{R}(-\theta). \tag{A.15}$$

For a waveplate with a retardance δ and the birefringence axis oriented at an angle β the Mueller matrix is therefore given by

$$\hat{\Gamma}(\delta, \beta) = \hat{R}(\beta)\hat{\Gamma}(\delta, 0)\hat{R}(-\beta), \tag{A.16}$$

where the evaluation yields:

$$\hat{\Gamma}(\delta, \beta) = \begin{pmatrix} 1 & 0 & 0 & 0 \\ 0 & \cos^2 2\beta + \cos\delta\sin^2 2\beta & \cos 2\beta\sin 2\beta(1-\cos\delta) & -\sin 2\beta\sin\delta \\ 0 & \cos 2\beta\sin 2\beta(1-\cos\delta) & \cos\delta\cos^2 2\beta + \sin^2 2\beta & \cos 2\beta\sin\delta \\ 0 & \sin 2\beta\sin\delta & -\cos 2\beta\sin\delta & \cos\delta \end{pmatrix} \tag{A.17}$$

Analogously, the Mueller matrix for a linear polarizer with transmission axis oriented at an angle α can be calculated as:

$$\hat{P}(\alpha) = \hat{R}(\alpha)\hat{P}(0)\hat{R}(-\alpha) = \frac{1}{2}\begin{pmatrix} 1 & \cos 2\alpha & \sin 2\alpha & 0 \\ \cos 2\alpha & \cos^2 2\alpha & \cos 2\alpha \sin 2\alpha & 0 \\ \sin 2\alpha & \cos 2\alpha \sin 2\alpha & \sin^2 2\alpha & 0 \\ 0 & 0 & 0 & 0 \end{pmatrix} \tag{A.18}$$

The expression for the Mueller matrix of an imperfect polarizer oriented at an angle α, $\hat{P}_{\text{imp}}(\alpha)$, can be calculated analogous to $\hat{\Gamma}(\delta, \beta)$ or $\hat{P}(\alpha)$.

A.3 Derivation of Linearized Calibration Equations

Here, the linearized calibration equations 3.29 shall be derived. Recall that we define the reference plane parallel to the transmission axis of the calibration polarizer. Then the incident light has the relative Stokes vector (1,0,0) and from Eq. 3.16 we obtain for $\tilde{\alpha} = 0$:

$$\frac{M}{I} = 1 = \frac{\frac{2}{1-\cos(\delta)}[C_4 \cos(2\alpha_0 - 4\beta_0) + S_4 \sin(2\alpha_0 - 4\beta_0)]}{C_0 - \frac{1+\cos(\delta)}{1-\cos(\delta)} \cdot [C_4 \cos(4\alpha_0 - 4\beta_0) + S_4 \sin(4\alpha_0 - 4\beta_0)]}, \tag{A.19}$$

$$\frac{C}{I} = 0 = \frac{\frac{2}{1-\cos(\delta)}[S_4 \cos(2\alpha_0 - 4\beta_0) - C_4 \sin(2\alpha_0 - 4\beta_0)]}{C_0 - \frac{1+\cos(\delta)}{1-\cos(\delta)} \cdot [C_4 \cos(4\alpha_0 - 4\beta_0) + S_4 \sin(4\alpha_0 - 4\beta_0)}. \tag{A.20}$$

We have three parameters to calibrate, so we need a third equation. We can rotate the polarizer in the polarimeter by a degree $\tilde{\alpha}$ and use Eq. A.19 with $\alpha_0 \to \alpha_0 + \tilde{\alpha}$. Note, that using Eq. A.20 with $\alpha_0 \to \alpha_0 + \tilde{\alpha}$ does not help since they would be linearly dependent. Therefore, from Eqs. A.19, A.19 with $\alpha_0 \to \alpha_0 + \tilde{\alpha}$, and A.20 the equation set for calibration is determined to be:

$$\begin{aligned} C_0 - \frac{1+\cos(\delta)}{1-\cos(\delta)}&[C_4 \cos(4\alpha_0 - 4\beta_0) + S_4 \sin(4\alpha_0 - 4\beta_0)] \\ &= \frac{2}{1-\cos(\delta)}[C_4 \cos(2\alpha_0 - 4\beta_0) + S_4 \sin(2\alpha_0 - 4\beta_0)], \end{aligned} \tag{A.21a}$$

$$\begin{aligned} \tilde{C}_0 - \frac{1+\cos(\delta)}{1-\cos(\delta)} &\cdot [\tilde{C}_4 \cos(4\alpha_0 + 4\tilde{\alpha} - 4\beta_0) + \tilde{S}_4 \sin(4\alpha_0 + 4\tilde{\alpha} - 4\beta_0)] \\ &= \frac{2}{1-\cos(\delta)}[\tilde{C}_4 \cos(2\alpha_0 + 2\tilde{\alpha} - 4\beta_0) + \tilde{S}_4 \sin(2\alpha_0 + 2\tilde{\alpha} - 4\beta_0)], \end{aligned} \tag{A.21b}$$

$$\arctan \frac{S_4}{C_4} = 2\alpha_0 - 4\beta_0. \tag{A.21c}$$

Let us define $\gamma = 2\alpha_0 - 4\beta_0$. We use the following trigonometric identities:

$$\begin{aligned} \cos(2\alpha_0 + \gamma) &= \cos 2\alpha_0 \cos \gamma - \sin 2\alpha_0 \sin \gamma \\ \sin(2\alpha_0 + \gamma) &= \sin 2\alpha_0 \cos \gamma + \cos 2\alpha_0 \sin \gamma \end{aligned} \tag{A.22}$$

With this, the first calibration equation A.21a can be rewritten as:

$$C_0 = \cos\gamma \left(\frac{2C_4}{1-\cos\delta} + \frac{1+\cos\delta}{1-\cos\delta}[C_4 \cos 2\alpha_0 + S_4 \sin 2\alpha_0] \right) + \\ \sin\gamma \left(\frac{2S_4}{1-\cos\delta} + \frac{1+\cos\delta}{1-\cos\delta}[S_4 \cos 2\alpha_0 - C_4 \sin 2\alpha_0] \right). \tag{A.23}$$

With the approximation $\cos\delta \simeq \frac{\pi}{2} - \delta$ for $\delta \approx \pi/2$ we can find the linearized solution for the retardance δ:

$$\delta = \frac{\pi}{2} + 1 + \frac{2(-C_0 + C_4 \cos\gamma + S_4 \sin\gamma)}{C_0 + C_4 \cos(2\alpha_0 + \gamma) + S_4 \sin(2\alpha_0 + \gamma)}. \tag{A.24}$$

Furthermore, we know from Eq. A.21c that:

$$\cos\gamma = \cos\arctan(S_4/C_4) = \frac{C_4}{\sqrt{S_4^2 + C_4^2}}, \tag{A.25}$$

$$\sin\gamma = \sin\arctan(S_4/C_4) = \frac{S_4}{\sqrt{S_4^2 + C_4^2}}. \tag{A.26}$$

Therefore the equation A.24 for δ simplifies to:

$$\delta = \frac{\pi}{2} + 1 + 2\,\frac{-C_0 + \sqrt{C_4^2 + S_4^2}}{C_0 + \cos 2\alpha_0 \sqrt{C_4^2 + S_4^2}}. \tag{A.27}$$

Using this result for the second calibration equation A.21b we obtain:

$$\delta = \frac{\pi}{2} + 1 + 2\,\frac{-\tilde{C}_0 + \sqrt{\tilde{C}_4^2 + \tilde{S}_4^2}}{\tilde{C}_0 + \cos(2\alpha_0 + 2\tilde{\alpha})\sqrt{\tilde{C}_4^2 + \tilde{S}_4^2}} \tag{A.28}$$

The comparison of the two above equations leads to an equation for α_0:

$$\frac{-C_0 + \sqrt{C_4^2 + S_4^2}}{C_0 + \cos 2\alpha_0 \sqrt{C_4^2 + S_4^2}} = \frac{-\tilde{C}_0 + \sqrt{\tilde{C}_4^2 + \tilde{S}_4^2}}{\tilde{C}_0 + \cos(2\alpha_0 + 2\tilde{\alpha})\sqrt{\tilde{C}_4^2 + \tilde{S}_4^2}}. \tag{A.29}$$

Now we perform a trigonometric expansion and linearize in α_0 ($\cos 2\alpha_0 \simeq 1$, $\sin 2\alpha_0 \simeq 2\alpha_0$) which leads to:

$$\frac{-C_0 + \sqrt{C_4^2 + S_4^2}}{C_0 + \sqrt{C_4^2 + S_4^2}} = \frac{-\tilde{C}_0 + \sqrt{\tilde{C}_4^2 + \tilde{S}_4^2}}{\tilde{C}_0 + \cos(2\tilde{\alpha})\sqrt{\tilde{C}_4^2 + \tilde{S}_4^2} - 2\alpha_0 \sin(2\tilde{\alpha})\sqrt{\tilde{C}_4^2 + \tilde{S}_4^2}}. \tag{A.30}$$

Resolving this equation for α_0 yields:

$$\alpha_0 = \frac{\left(\tilde{C}_0 - \sqrt{\tilde{C}_4^2 + \tilde{S}_4^2}\right)\left(C_0 + \sqrt{C_4^2 + S_4^2}\right) - \left(\tilde{C}_0 + \cos(2\tilde{\alpha})\sqrt{\tilde{C}_4^2 + \tilde{S}_4^2}\right)\left(C_0 - \sqrt{C_4^2 + S_4^2}\right)}{2\sin(2\tilde{\alpha})\sqrt{\tilde{C}_4^2 + \tilde{S}_4^2}\left(\sqrt{C_4^2 + S_4^2} - C_0\right)}. \tag{A.31}$$

We can simplify this expression using the identity following Eq. 3.15 with $\tilde{\alpha} = 0$ and $\tilde{\alpha} \neq 0$:

$$\sqrt{C_4^2 + S_4^2} = \sqrt{\tilde{C}_4^2 + \tilde{S}_4^2} = \frac{1 - \cos\delta}{2}. \tag{A.32}$$

Note, that we cannot use this identity to determine δ. We neglected a constant pre-factor in Eq. 3.13 because we are not measuring the absolute intensity but rather the normalized relative Stokes parameters. In the case of an absorbance or intensity-voltage conversion factor a in Eq. 3.13, the above equation reads

$$\sqrt{C_4^2 + S_4^2} = \sqrt{\tilde{C}_4^2 + \tilde{S}_4^2} = a\frac{1 - \cos\delta}{2}. \tag{A.33}$$

Since we do not know a, we cannot use this identity to determine δ.

Using Eq. A.32, we arrive at the simplest form of the linearized expression for α_0:

$$\begin{aligned}\alpha_0 &= \frac{\tilde{C}_0 - \sqrt{S_4^2 + C_4^2} + \cos^2(\tilde{\alpha})\left(\sqrt{C_4^2 + S_4^2} - C_0\right)}{\sin(2\tilde{\alpha})\left(\sqrt{C_4^2 + S_4^2} - C_0\right)} \\ &= \frac{\cot\tilde{\alpha}}{2} - \frac{1}{\sin(2\tilde{\alpha})}\frac{\sqrt{S_4^2 + C_4^2} - \tilde{C}_0}{\sqrt{S_4^2 + C_4^2} - C_0}.\end{aligned} \tag{A.34}$$

From Eq. A.21c, β_0 is given by:

$$\beta_0 = \frac{1}{4}\left(\arctan\frac{S_4}{C_4} - 2\alpha_0\right). \tag{A.35}$$

From Eq. A.27, the solution for δ for small α_0 is:

$$\delta = \frac{\pi}{2} + 1 - 2\,\frac{C_0 - \sqrt{C_4^2 + S_4^2}}{C_0 + \sqrt{C_4^2 + S_4^2}}. \tag{A.36}$$

Note that this expression is independent of $\tilde{\alpha}$ which means that the precision of the rotation stage with the polarizer affects the calibration of δ only to the second order. Furthermore, Eq. A.36 means that to a good approximation the retardance δ can be calibrated without using the second rotation stage.

Eqs. A.34, A.35, and A.36 form the set of linearized calibration equations used to derive the optimal calibration rotation angle $\tilde{\alpha}$ in Sec. 3.5.

A.4 Averaging Error of Ellipticity Gradients

When measuring the ellipticity gradients shown in Fig. 4.5, the polarimeter is translated on a linear stage[1] in the x direction across the laser beam. The linear stage is controlled electronically via LabView with an accuracy of less than $1\,\mu$m. Therefore, the polarimeter can resolve spatial polarization changes on a micrometer scale. Typically, this high resolution is not needed and the polarimeter measures spatial polarization changes on a scale of fractions of a millimeter, as in Fig. 4.5. However, the measured polarization is an average over the aperture in front of the polarimeter which has a diameter of $d \simeq 1\,$mm. Here we shall briefly examine how the averaging changes the measured shape of gradients depicted in Fig. 4.5 with corresponding fit results in Table 4.3.

Assume that we measure a spatially dependent circular polarization $S_{I,\mathrm{true}}(x)$ described by the function from Eq. 4.19 with an aperture of diameter d. The polarimeter measures n averaged values at positions $x_n = x_s + n\,\Delta x$, where Δx is the incremental step and x_s the initial position. The averaged data points are given by:

$$S_{I,\mathrm{aver}}(x_n) = \frac{1}{d}\int_{x_n-d/2}^{x_n+d/2} S_{I,\mathrm{true}}(x)\,\mathrm{d}x. \tag{A.37}$$

Fig. A.1 shows an example of the simulated scenario with $w_x = 1.4$ mm, $g = 0.63\,\%/\mathrm{mm}$, $o = 3.80\%$, $\Delta x = 100\,\mu$m, $d = 1$ mm, $x_s = 0\,$mm. The orange curve shows the true function $S_{I,\mathrm{true}}$ from Eq. 4.19 with these parameters. The blue points represent the averaged values according to Eq. A.37. These points are fitted with the function from Eq. 4.19 leaving the parameters g and o free. From the fit to the blue averaged points we obtain the result $g = 0.60\,\%/\mathrm{mm}$ and $o = 3.73\%$. Compared to the true values, the error is $g_{\mathrm{err}} = 0.03\,\%/\mathrm{mm}$ and $o_{\mathrm{err}} = 0.07\,\%$.

The above calculation is performed for every measured gradient from Fig. 4.5 with fit results in Table 4.3. The errors from averaging over the aperture of the polarimeter are listed in the lower part of Table A.1. As expected, the deviation from the true values is small. For both coefficients we find an error of only a few percent: $g_{\mathrm{err}}/g \sim 5\%$ and $o_{\mathrm{err}}/o \sim 1-4\%$. Note that the uncertainty from the fit for g and o is on the same order. Therefore, the error from averaging over a finite aperture can be neglected for the gradients described by the function from Eq. 4.19.

The reason that the averaging does not considerably affect the measured shape of the gradient is the following. For $S_{I,\mathrm{true}}(x) \propto x$ we find that the averaged value exactly matches the true value:

$$S_{I,\mathrm{aver}}(x_n) = S_{I,\mathrm{true}}(x_n) \quad \text{for} \quad S_{I,\mathrm{true}}(x) \propto x. \tag{A.38}$$

---

[1] Zaber linear actuator T-NA08A25-S with translation stage TSB28E

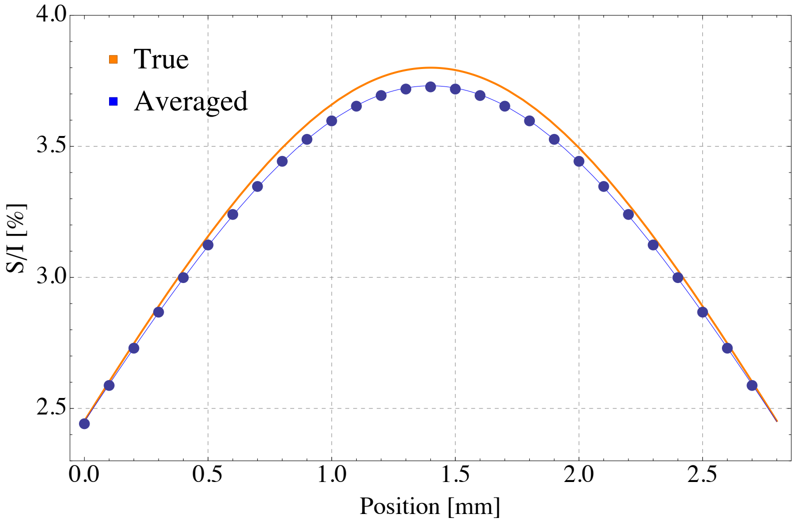

FIGURE A.1: Calculated difference between the true function $S_{I,\text{true}}$ (orange curve) from Eq. 4.19 and the averaged blue points $S_{I,\text{aver}}(x_n)$ according to Eq. A.37. The parameters are set to experimental values: $w_x = 1.4$ mm, $g = 0.63\,\%/\text{mm}$, $o = 3.80\%$, $x \to x - x_0$ with $x_0 = 1.4\,\text{mm}$, $d = 1$ mm, $\Delta x = 100\,\mu\text{m}$, $x_s = 0\,\text{mm}$ and $n = 28$. The blue points are fitted with the same function from Eq. 4.19 leaving the parameters g and o free. The fitted values are $g = 0.60\,\%/\text{mm}$ and $o = 3.73\%$. Therefore, the difference between the averaged and the true gradient or offset coefficients is negligible.

Coefficient	$P_{\text{tot}} = 2$ W			$P_{\text{tot}} = 4$ W			$P_{\text{tot}} = 6$ W		
	Lenses	FP I	FP II	Lenses	FP I	FP II	Lenses	FP I	FP II
g [%/mm]	0.25(3)	0.63(3)	0.02(2)	0.65(5)	1.78(10)	0.03(5)	0.63(10)	3.45(20)	0.43(8)
o [%]	0.76(1)	3.80(1)	0.12(1)	1.68(2)	7.36(6)	0.53(2)	2.55(5)	12.10(9)	0.72(3)
Errors from averaging over an aperture with diameter $d = 1\,\text{mm}$:									
g_{err} [%/mm]	0.012	0.031	0.001	0.032	0.087	0.001	0.031	0.169	0.021
o_{err} [%]	0.027	0.069	0.002	0.071	0.195	0.003	0.069	0.378	0.047

TABLE A.1: The upper part is identical to Table 4.3 which lists the thermally-induced gradient and offset coefficients in S/I from the fits to the data in Fig. 4.5 with the function from Eq. 4.19. The lower part shows the calculated errors due to averaging over the aperture in front of the polarimeter. The errors are found to be on the order of the uncertainties from the fits.

Indeed, for the function given in Eq. 4.19 we find that this is true for $x \gtrsim w_x$:

$$S_I(x) \simeq g(w_x - \sqrt{2\pi}x) + o \quad \text{for} \quad x \gtrsim w_x. \tag{A.39}$$

We conclude that the averaging error due to the aperture in front of the polarimeter is negligible for thermally-induced gradients described by Eq. 4.19. The observed gradient and offset coefficients are reduced by $\lesssim 5\%$ compared to the true values.

Bibliography

[1] S. Alali and A. Vitkin. Polarized light imaging in biomedicine: emerging mueller matrix methodologies for bulk tissue assessment. *Journal of Biomedical Optics*, 20(6):061104, 2015.

[2] B.-G. Andersson, A. Lazarian, and J. E. Vaillancourt. Interstellar Dust Grain Alignment. *Annual Review of Astronomy and Astrophysics*, 53:501–539, Aug. 2015.

[3] V. Andreev, D. Ang, J. Baron, D. DeMille, J. M. Doyle, G. Gabrielse, N. R. Hutzler, B. R. O'Leary, C. D. Panda, C. Weber, A. D. West, E. P. West, and G. Wilburn. Electron EDM measurements in a beam of ThO: Demostrated and planned upgrades. Poster for the 47th Annual Meeting of the APS Division of Atomic, Molecular and Optical Physics, May 2016.

[4] T. Ashida, A. Miyamura, N. Oka, Y. Sato, T. Yagi, N. Taketoshi, T. Baba, and Y. Shigesato. Thermal transport properties of polycrystalline tin-doped indium oxide films. *Journal of Applied Physics*, 105(7), 2009.

[5] R. M. A. Azzam. Arrangement of four photodetectors for measuring the state of polarization of light. *Opt. Lett.*, 10(7):309–311, Jul 1985.

[6] R. M. A. Azzam. Division-of-amplitude photopolarimeter based on conical diffraction from a metallic grating. *Appl. Opt.*, 31(19):3574–3576, Jul 1992.

[7] J. Barber. *Elasticity.* Boston: Kluwer Academic Publishers, 1992.

[8] J. Baron, W. C. Campbell, D. DeMille, J. M. Doyle, G. Gabrielse, Y. V. Gurevich, P. W. Hess, N. R. Hutzler, E. Kirilov, I. Kozyryev, B. R. O'Leary, C. D. Panda, M. F. Parsons, E. S. Petrik, B. Spaun, A. C. Vutha, and A. D. West. Order of magnitude smaller limit on the electric dipole moment of the electron. *Science*, 343(6168):269–272, 2014.

[9] J. Baron, W. C. Campbell, D. DeMille, J. M. Doyle, G. Gabrielse, Y. V. Gurevich, P. W. Hess, N. R. Hutzler, E. Kirilov, I. Kozyryev, B. R. O'Leary, C. D. Panda, M. F. Parsons, B. Spaun, A. C. Vutha, A. D. West, and E. P. West. Methods, analysis, and the treatment of systematic errors for the electron electric dipole moment search in thorium monoxide. *New Journal of Physics (submitted)*, 2016.

[10] M. Bass, E. W. Van Stryland, D. R. Williams, and W. L. Wolfe. *Handbook of Optics, Vol II. Devices, Measurements, and Properties.* McGraw-Hill, 1995.

[11] Bernhard Halle Nachfl. GmbH. Product catalog. `http://www.b-halle.de/EN/Downloads/BHalleCatalogEN.pdf`. Accessed Nov 2016.

[12] H. G. Berry, G. Gabrielse, and A. E. Livingston. Measurement of the stokes parameters of light. *Appl. Opt.*, 16(12):3200–3205, Dec 1977.

[13] G. Börner. *The Early Universe.* Springer, 2003.

[14] J. Brown and A. Carrington. *Rotational Spectroscopy of Diatomic Molecules.* Cambridge Molecular Science. Cambridge University Press, 2003.

[15] L. Canetti, M. Drewes, and M. Shaposhnikov. Matter and antimatter in the universe. *New Journal of Physics*, 14(9):095012, 2012.

[16] M. Chaichian, A. D. Dolgov, V. A. Novikov, and A. Tureanu. CPT Violation Does Not Lead to Violation of Lorentz Invariance and Vice Versa. *Phys. Lett.*, B699:177–180, 2011.

[17] J. Chang, N. Zeng, H. He, Y. He, and H. Ma. Single-shot spatially modulated stokes polarimeter based on a grin lens. *Opt. Lett.*, 39(9):2656–2659, May 2014.

[18] J. H. Christenson, J. W. Cronin, V. L. Fitch, and R. Turlay. Evidence for the 2π Decay of the K_2^0 Meson. *Phys. Rev. Lett.*, 13:138–140, Jul 1964.

[19] D. Clarke. Effects in polarimetry of interference within wave plates. *Astronomy and Astrophysics*, 434:377–384, 04/2005.

[20] D. Clarke. *Polarized light and optical measurement.* Oxford, New York, Pergamon Press, 1971.

[21] D. Clarke. Interference effects in pancharatnam wave plates. *Journal of Optics A: Pure and Applied Optics*, 6(11):1047, 2004.

[22] D. Colladay and V. A. Kostelecký. CPT violation and the Standard Model. *Phys. Rev. D*, 55:6760–6774, Jun 1997.

[23] P. Coppi. How Do We know Antimater is Absent? *eConf*, C040802:L017, 2004.

[24] Corning Inc. Corning$^{\mathrm{TM}}$ 7980 Fused Silica Datasheet. `https://www.corning.com/media/worldwide/csm/documents/5bf092438c5546dfa9b08e423348317b.pdf`. Accessed: 2016-11-06.

[25] Crystran Inc. N-BK7 Technical Datasheet. `http://www.crystran.co.uk/optical-materials/optical-glass-n-bk7-and-others`. Accessed: 2016-11-06.

[26] J. W. Dally and W. F. Riley. *Experimental stress analysis.* New York: McGraw-Hill, 1978.

[27] J. DiSciacca, M. Marshall, K. Marable, G. Gabrielse, S. Ettenauer, E. Tardiff, R. Kalra, D. W. Fitzakerley, M. C. George, E. A. Hessels, C. H. Storry, M. Weel, D. Grzonka, W. Oelert, and T. Sefzick. One-particle measurement of the antiproton magnetic moment. *Phys. Rev. Lett.*, 110:130801, Mar 2013.

[28] J.-F. Donati, C. Catala, G. A. Wade, G. Gallou, G. Delaigue, and P. Rabou. Dedicated polarimeter for the musicos chelle spectrograph. *Astronomy and Astrophysics Supplement*, 134:149–159, 01/1999.

[29] S. Eisenbach, H. Lotem, Z. Horvitz, G. Miron, M. Lando, and S. Gabay. Thermally induced window birefringence in high-power copper vapor laser. *Proc. SPIE*, 1972:13–26, 1993.

[30] J. Engel, M. J. Ramsey-Musolf, and U. van Kolck. Electric dipole moments of nucleons, nuclei, and atoms: The standard model and beyond. *Progress in Particle and Nuclear Physics*, 71:21 – 74, 2013. Fundamental Symmetries in the Era of the LHC.

[31] M. S. Farhan, E. Zalnezhad, A. R. Bushroa, and A. A. D. Sarhan. Electrical and optical properties of indium-tin oxide (ITO) films by ion-assisted deposition (IAD) at room temperature. *International Journal of Precision Engineering and Manufacturing*, 14(8):1465–1469, 2013.

[32] L. Filipovic and S. Selberherr. Performance and stress analysis of metal oxide films for cmos-integrated gas sensors. *Sensors (Basel)*, 15(4):72067227, 2015.

[33] T. Fleig and M. K. Nayak. Electron electric dipole moment and hyperfine interaction constants for tho. *J. Mol. Spectr.*, 300:16 – 21, 2014.

[34] H. Fujiwara. *Principles of Spectroscopic Ellipsometry.* John Wiley and Sons, Ltd, 2007.

[35] G. Gabrielse. The standard model's greatest triumph. *Physics Today*, 66, 2013.

[36] D. Goldstein. *Polarized Light.* Marcel Dekker, 2003.

[37] J. S. Greaves, W. S. Holland, T. Jenness, and T. G. Hawarden. Magnetic field surrounding the starburst nucleus of the galaxy M82 from polarized dust emission. *Nature*, 404:732–733, 2000.

[38] O. W. Greenberg. *CPT* Violation Implies Violation of Lorentz Invariance. *Phys. Rev. Lett.*, 89:231602, Nov 2002.

[39] A. V. Gubskaya and P. G. Kusalik. The total molecular dipole moment for liquid water. *The Journal of Chemical Physics*, 117(11):5290–5302, 2002.

[40] Y. Gurevich. *Preliminary Measurements for an Electron EDM Experiment in ThO.* PhD thesis, Harvard University, 2012.

[41] T. J. Harries and I. D. Howarth. Linear spectropolarimetry of the H emission line of η Puppis. *Astronomy and Astrophysics*, 310:533–546, 06/1996.

[42] C. He, J. Chang, Y. Wang, R. Liao, H. He, N. Zeng, and H. Ma. Linear polarization optimized stokes polarimeter based on four-quadrant detector. *Appl. Opt.*, 54(14):4458–4463, May 2015.

[43] P. W. Hess. *Improving the Limit on the Electron EDM: Data Acquisition and Systematics Studies in the ACME Experiment.* PhD thesis, Harvard University, 2014.

[44] Hinds Instruments. PolSNAP$^{\mathrm{TM}}$ and other polarimeters. `http://www.hindsinstruments.com/products/polarimeters/`, accessed Nov 2016.

[45] J. Hough. Polarimetry: a powerful diagnostic tool in astronomy. *Astronomy and Geophysics*, 47(3):3.31–3.35, 2006.

[46] J. J. Hudson, D. M. Kara, I. J. Smallman, B. E. Sauer, M. R. Tarbutt, and E. A. Hinds. Improved measurement of the shape of the electron. *Nature*, 473:493–496, 2011.

[47] W. Hui, Y. Wei, and W. Shibin. Superposition of optical glass stress birefringence. *High Power Laser and Particle Beams*, 24(09):2068, 2012.

[48] N. R. Hutzler. *A New Limit on the Electron Electric Dipole Moment: Beam Production, Data Interpretation, and Systematics.* PhD thesis, Harvard University, 2014.

[49] N. R. Hutzler, M. F. Parsons, Y. V. Gurevich, P. W. Hess, E. Petrik, B. Spaun, A. C. Vutha, D. Demille, G. Gabrielse, and J. M. Doyle. A cryogenic beam of refractory, chemically reactive molecules with expansion cooling. *Physical Chemistry Chemical Physics (Incorporating Faraday Transactions)*, 13:18976, 2011.

[50] R. Imazawa, Y. Kawano, T. Ono, and K. Itami. Development of real-time rotating waveplate Stokes polarimeter using multi-order retardation for ITER poloidal polarimeter. *Review of Scientific Instruments*, 87(1), 2016.

[51] R. Kitamura, L. Pilon, and M. Jonasz. Optical constants of silica glass from extreme ultraviolet to far infrared at near room temperature. *Appl. Opt.*, 46(33):8118–8133, Nov 2007.

[52] D. S. Kliger. *Polarized light in optics and spectroscopy.* Boston: Academic Press, 1990.

[53] D. S. Kliger, J. Lewis, and C. E. Randall. *Polarized Light in Optics and Spectroscopy.* Academic Press Inc., 1990.

[54] Kliger, S. David and Lewis, W. James and Randall, E. Cora. *Polarized Light in Optics and Spectroscopy.* Academic Press, Inc., 1990.

[55] W. Koechner. Thermal lensing in a Nd:YAG laser rod. *Appl. Opt.*, 9(11):2548–2553, Nov 1970.

[56] E. W. Kolb and M. S. Turner. *The early universe.* Addison-Wesley, 1994.

[57] G. H. Lee. *An introduction to experimental stress analysis.* New York, Wiley, 1950.

[58] T. D. Lee and C. N. Yang. Parity nonconservation and a two-component theory of the neutrino. *Phys. Rev.*, 105:1671–1675, Mar 1957.

[59] T. Lepetit and B. Kante. Metasurfaces: Simultaneous Stokes parameters. *Nature Photonics*, 9:709–719, 2015.

[60] G. Luders. On the Equivalence of Invariance under Time Reversal and under Particle-Antiparticle Conjugation for Relativistic Field Theories. *Kong. Dan. Vid. Sel. Mat. Fys. Med.*, 28N5:1–17, 1954.

[61] J. W. Maseberg and T. J. Gay. Fluorescence polarization of helium negative-ion resonances excited by polarized electron impact. *Journal of Physics B: Atomic, Molecular and Optical Physics*, 39(23):4861, 2006.

[62] V. Mukhanov. *Physical Foundations Of Cosmology.* Cambridge University Press, 2005.

[63] D. Neerinck and T. Vink. Depth profiling of thin ito films by grazing incidence x-ray diffraction. *Thin Solid Films*, 278(1):12 – 17, 1996.

[64] T. R. Nissle and C. L. Babcock. Stress-optical coefficient as related to glass composition. *Journal of the American Ceramic Society*, 56(11):596–598, 1973.

[65] B. O'Leary. AC Stark Shift Phases in ACME II. ACME Collaboration meeting presentation, 04/05/2016.

[66] C. D. Panda, B. R. O'Leary, A. D. West, J. Baron, P. W. Hess, C. Hoffman, E. Kirilov, C. B. Overstreet, E. P. West, D. DeMille, J. M. Doyle, and G. Gabrielse. Stimulated raman adiabatic passage preparation of a coherent superposition of tho $H^3\Delta_1$ states for an improved electron electric-dipole-moment measurement. *Phys. Rev. A*, 93:052110, May 2016.

[67] C. Patrignani et al. Review of Particle Physics. *Chin. Phys.*, C40:100001, 2016.

[68] J. Pavlin, N. Vaupotic, and M. Cepic. Direction dependence of the extraordinary refraction index in uniaxial nematic liquid crystals. *European Journal of Physics*, 34(2):331, 2013.

[69] A. Peinado, A. Turpin, A. Lizana, E. Fernández, J. Mompart, and J. Campos. Conical refraction as a tool for polarization metrology. *Opt. Lett.*, 38(20):4100–4103, Oct 2013.

[70] M. E. Peskin and D. V. Schroeder. *An Introduction to Quantum Field Theory.* Westview Press, 1995.

[71] A. N. Petrov, L. V. Skripnikov, A. V. Titov, N. R. Hutzler, P. W. Hess, B. R. O'Leary, B. Spaun, D. DeMille, G. Gabrielse, and J. M. Doyle. Zeeman interaction in ThO $H\,^3\Delta_1$ for the electron electric-dipole-moment search. *Phys. Rev. A*, 89:062505, Jun 2014.

[72] M. Pospelov and A. Ritz. Electric dipole moments as probes of new physics. *Annals of Physics*, 318(1):119 – 169, 2005. Special Issue.

[73] N. F. Ramsey. Electric-dipole moments of elementary particles. *Reports on Progress in Physics*, 45(1):95, 1982.

[74] K. N. Rao. Optical and electrical properties of indium-tin oxide. *Indian Journal of Pure and Applied Physics*, 42:201–204, 2004.

[75] B. C. Regan, E. D. Commins, C. J. Schmidt, and D. DeMille. New limit on the electron electric dipole moment. *Phys. Rev. Lett.*, 88:071805, Feb 2002.

[76] M. J. Romerein, J. N. Philippson, R. L. Brooks, and R. C. Shiell. Calibration method using a single retarder to simultaneously measure polarization and fully characterize a polarimeter over a broad range of wavelengths. *Appl. Opt.*, 50(28):5382–5389, Oct 2011.

[77] A. D. Sakharov. Violation of CP Invariance, C Asymmetry, and Baryon Asymmetry of the Universe. *Pisma Zh. Eksp. Teor. Fiz.*, 5:32–35, 1967.

[78] J. J. Sakurai. *Modern Quantum Mechanics.* Addison Wesley, 1994.

[79] P. Sandars. The electric dipole moment of an atom. *Physics Letters*, 14(3):194 – 196, 1965.

[80] Schafter + Kirchhoff: Optics, Metrology, and Photonics. Polarization Analyzer SK010PA. `http://www.sukhamburg.com/download/polAnalyzer_e.pdf`. Accessed Nov 2016.

[81] L. I. Schiff. Measurability of nuclear electric dipole moments. *Phys. Rev.*, 132:2194–2200, Dec 1963.

[82] Schott AG. Borofloat Glass, data sheet. `http://www.us.schott.com/borofloat/english/download/borofloat33_therm_usa_web.pdf`. Accessed Nov 2016.

[83] W. Shurcliff. *Polarized Light: Production and Use.* Harvard University Press, 1966.

[84] L. V. Skripnikov and A. V. Titov. Theoretical study of thorium monoxide for the electron electric dipole moment search, II: Electronic properties of $H^3\Delta_1$ in ThO. *J. Chem. Phys.*, 142:024301, 2015.

[85] F. Snik, J. Craven-Jones, M. Escuti, S. Fineschi, D. Harrington, A. De Martino, D. Mawet, J. Riedi, and J. S. Tyo. An overview of polarimetric sensing techniques and technology with applications to different research fields. *Proc. SPIE*, 9099:90990B–90990B–20, 2014.

[86] F. Snik, J. H. H. Rietjens, A. Apituley, H. Volten, B. Mijling, A. Di Noia, S. Heikamp, R. C. Heinsbroek, O. P. Hasekamp, J. M. Smit, J. Vonk, D. M. Stam, G. van Harten, J. de Boer, C. U. Keller, and 3187 iSPEX citizen scientists. Mapping atmospheric aerosols with a citizen science network of smartphone spectropolarimeters. *Geophysical Research Letters*, 41(20):7351–7358, 2014. 2014GL061462.

[87] N. Solmeyer, K. Zhu, and D. S. Weiss. Note: Mounting ultra-high vacuum windows with low stress-induced birefringence. *Review of Scientific Instruments*, 82(6), 2011.

[88] B. Spaun. *A Ten-Fold Improvement to the Limit of the Electron Electric Dipole Moment.* PhD thesis, Harvard University, 2014.

[89] G. Stokes. *On the Composition and Resolution of Streams of Polarized Light from Different Sources.* Proceedings of the Cambridge Philosophical Society: Mathematical and physical sciences. Cambridge Philosophical Society, 1852.

[90] G. G. Stokes. *Mathematical and Physical Papers, Vol. 3.* Cambridge University, 1901.

[91] G. 't Hooft. Symmetry Breaking through Bell-Jackiw Anomalies. *Phys. Rev. Lett.*, 37:8–11, Jul 1976.

[92] Thorlabs Inc. Free-space and fiber-coupled polarimeter systems: PAX5710 and PAX5720 series. `https://www.thorlabs.com/newgrouppage9.cfm?objectgroup_id=1564`. Accessed Nov 2016.

[93] Thorlabs Inc. Overview and specs of Glan-Laser Calcite Polarizers. `https://www.thorlabs.de/newgrouppage9.cfm?objectgroup_id=815`. Accessed Nov 2016.

[94] A. Vutha. *A search for the electric dipole moment of the electron using thorium monoxide.* PhD thesis, Yale University, 2011.

[95] A. C. Vutha, W. C. Campbell, Y. V. Gurevich, N. R. Hutzler, M. Parsons, D. Patterson, E. Petrik, B. Spaun, J. M. Doyle, G. Gabrielse, and D. DeMille. Search for the electric dipole moment of the electron with thorium monoxide. *Journal of Physics B: Atomic, Molecular and Optical Physics*, 43(7):074007, 2010.

[96] A. C. Vutha, B. Spaun, Y. V. Gurevich, N. R. Hutzler, E. Kirilov, J. M. Doyle, G. Gabrielse, and D. DeMille. Magnetic and electric dipole moments of the $H\ ^3\Delta_1$ state in ThO. *Phys. Rev. A*, 84:034502, Sep 2011.

[97] R. Waxler and A. Napolitano. Relative stress-optical coefficients of some National Bureau of Standards optical glasses. *Journal of Research of the National Bureau of Standards*, 59(2):121, 1957.

[98] S. Weinberg. *Cosmology.* Oxford, 2008.

[99] C. S. Wu, E. Ambler, R. W. Hayward, D. D. Hoppes, and R. P. Hudson. Experimental test of parity conservation in beta decay. *Phys. Rev.*, 105:1413–1415, Feb 1957.

[100] T. Yagi, K. Tamano, Y. Sato, N. Taketoshi, T. Baba, and Y. Shigesato. Analysis on thermal properties of tin doped indium oxide films by picosecond thermoreflectance measurement. *Journal of Vacuum Science and Technology A*, 23(4):1180–1186, 2005.

[101] A. Yariv. *Photonics: optical electronics in modern communications.* New York: Oxford University Press, 2007.

[102] P. Yeh and C. Gu. *Optics of Liquid Crystal Displays.* Wiley, 2010.

[103] P. R. Yoder. *Opto-Mechanical Systems Design, Third Edition.* Taylor and Francis, 2005.

[104] X. Zhao, X. Pan, X. Fan, P. Xu, A. Bermak, and V. G. Chigrinov. Patterned dual-layer achromatic micro-quarter-wave-retarder array for active polarization imaging. *Opt. Express*, 22(7):8024–8034, Apr 2014.